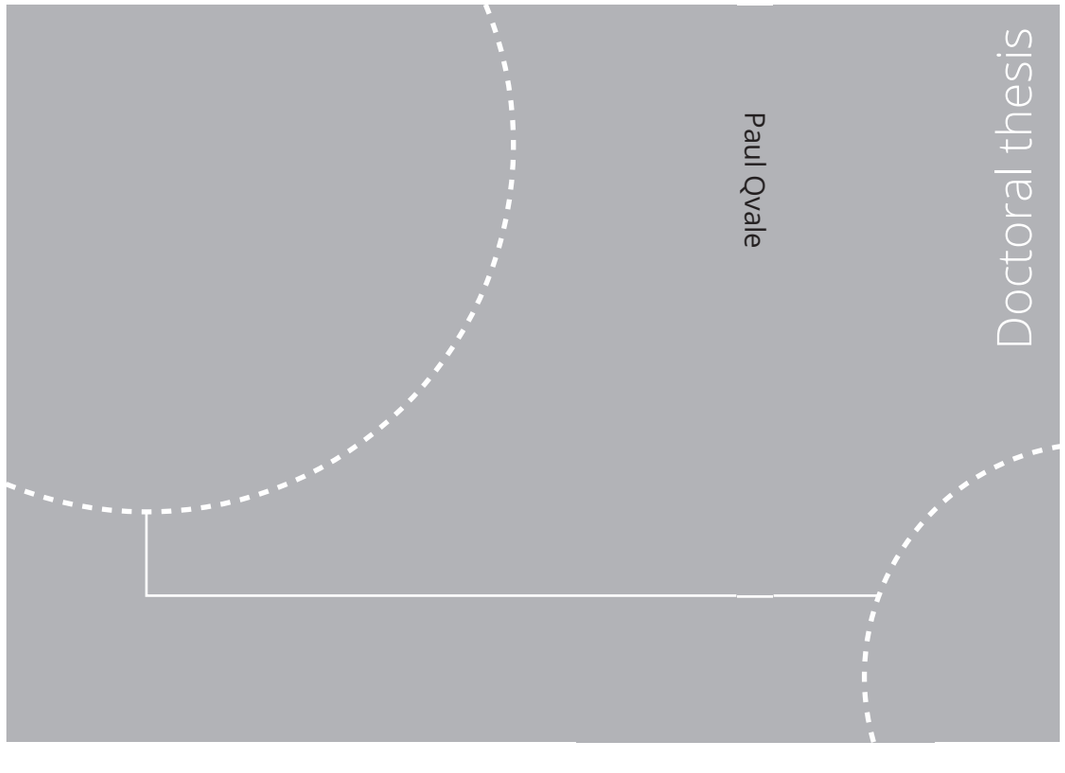

Doctoral theses at NTNU, 2022:296

Paul Qvale

Fatigue crack initiation in corroded offshore mooring chains

ISBN 978-82-326-5720-9 (printed ver.)
ISBN 978-82-326-5943-2 (electronic ver.)
ISSN 1503-8181 (printed ver.)
ISSN 2703-8084 (electronic ver.)

NTNU
Norwegian University of
Science and Technology

Doctoral theses at NTNU, 2022:296

NTNU

NTNU
Norwegian University of
Science and Technology
Thesis for the degree of
Philosophiae Doctor
Faculty of Engineering
Department of Structural Engineering

NTNU
Norwegian University of
Science and Technology

Paul Qvale

Fatigue crack initiation in corroded offshore mooring chains

Thesis for the degree of Philosophiae Doctor

Trondheim, October 2022

Norwegian University of Science and Technology
Faculty of Engineering
Department of Structural Engineering

NTNU
Norwegian University of
Science and Technology

NTNU
Norwegian University of Science and Technology

Thesis for the degree of Philosophiae Doctor

Faculty of Engineering
Department of Structural Engineering

© Paul Qvale

ISBN 978-82-326-5720-9 (printed ver.)
ISBN 978-82-326-5943-2 (electronic ver.)
ISSN 1503-8181 (printed ver.)
ISSN 2703-8084 (electronic ver.)

Doctoral theses at NTNU, 2022:296

PRINTED IN NORWAY
NO - 1598

NORDIC SWAN ECOLABEL
Printed matter
2041 0731

Printed by Skipnes Kommunikasjon AS

Preface

This thesis is submitted in partial fulfilment of the requirements for the degree of Doctor of Philosophy (Ph.D.) at the Faculty of Engineering of the Norwegian University of Science and Technology (NTNU). The work was conducted at the Department of Structural Engineering in the years 2018-2022. The work was supervised by professor Bjørn Helge Skallerud and associate professor Sigmund Kyrre Ås, both NTNU. Funding was received from the Norwegian Research Council (NRC) through the project KPN LifeMoor (RCN contract No. 280705). This thesis is written as a collection of articles that have been published in peer-reviewed journals. The aim of the thesis is to bring the articles into context of the KPN LifeMoor project and current research on degradation of offshore mooring chains.

Abstract

Mooring chains on floating offshore structures suffer from combined degradation from corrosion and fatigue. Corrosion reduces cross-sectional areas of the chains and creates surface pits. During cyclic loading of the chains, these pits can raise stress amplitudes locally and act as initiation points for fatigue cracks. The current work is focused on fatigue initiation in R4-grade mooring chain steel from both naturally corroded surfaces, idealized geometries of corrosion pits and fatigue cracks blunted by corrosion.

The full-field digital image correlation (DIC) technique was used to measure crack initiation on irregular, corroded surfaces from offshore mooring chain during fatigue testing in air. Finite element analysis (FEA) was paired with the DIC measurements to establish an initiation S-N curve for the surface. The first cracks initiated at 13-24% of the lifetimes of the specimens. Initiation lives were much shorter than in specimens with machined hemispherical notches, indicating that fatigue tests of machined specimens yield non-conservative initiation life estimates for mooring chains. Crack initiation was measured close to the mouths of the hemispherical notches. In a strain-controlled fatigue test, mean stress relaxation (MSR) was observed even at a stress amplitude below the cyclic yield stress. When taking cyclic softening and MSR into account in fatigue initiation predictions for the hemispherical notches, accuracy was significantly improved compared to calculations based on a monotonic material model. Other specimens were subjected to alternating phases of corrosion and fatigue to replicate in-service seasonal load variations. No significant difference in fatigue lifetimes was registered between specimens subjected to continuous fatigue and those periodically interrupted by phases of accelerated corrosion. Moreover, eight months of natural corrosion of specimens with fatigue cracks did not have a large effect on their remaining fatigue lifetimes. Thus, crack tip blunting from dissolution by corrosion during calm summer seasons is not expected to have a lifetime-extending effect on fatigue-cracked mooring chains.

FEA stress calculations based on a dynamic load analysis of an offshore mooring system were performed. Results showed that the stress amplitudes in the fatigue tests performed in the current work represents well the highest stress amplitudes in the mooring chain links in service. It is suggested how the method for generating fatigue initiation S-N curves in the current work can be modified for fatigue tests in saltwater environments.

Acknowledgements

I will begin by thanking Bjørn Skallerud, for his supervision, heavy involvement in review of the articles and facilitation of the experimental programs; and Sigmund Ås, for his supervision, review and assistance and discussions on measurement and monitoring techniques. I want to thank fellow Ph.D. candidate Ershad Zarandi, for discussions and collaboration on experimental programs, and for patiently taking his time to help finalizing two of the articles, even after completion of his own degree. I want to thank Christian Frugone, who made an invaluable contribution to the work by setting up the fatigue rig and its communications for some of the experimental programs. I want to thank Erling Lone for kindly sharing his results and thoughts on loading of mooring chains; and Gunnstein Frøseth, for his contribution to the discussion. Acknowledgements also goes to Andreas Erbe, Ole Øystein Knudsen and Christian Torres, for very helpful discussions on corrosion mechanisms and testing; staff and management of SINTEF and NTNU labs, for supporting and prioritizing my work, even at times of restricted access during the COVID-19 pandemic; SINTEF workshop staff, for fast execution of every machining task; Håkon Nordhagen and Alberto Arredondo, for their contributions to the articles; Trond Auestad and Egil Fagerholt, for assistance and discussions on the digital image correlation technique; and Mads Aursand, for discussions on fatigue crack growth. Finally, I am grateful for the funding received through the KPN LifeMoor project and to everyone who contributed to initiating the project.

Paul Qvale,

Trondheim, June 23, 2022

Contents

Appended articles

1. Qvale P, Zarandi EP, Ås SK, Skallerud BH. Digital image correlation for continuous mapping of fatigue crack initiation sites on corroded surface from offshore mooring chain. Int J Fatigue, 2021;151:106350. DOI: 10.1016/j.ijfatigue.2021.106350.
2. Qvale P, Zarandi EP, Arredondo A, Ås SK, Skallerud BH. Effect of cyclic softening and mean stress relaxation on fatigue crack initiation in a hemispherical notch. Fatigue Fract Eng Mater Struct 2022;1-17. DOI: 10.1111/ffe.13834.
3. Qvale P, Nordhagen HO, Ås SK, Skallerud BH. Effect of long periods of corrosion on the fatigue lifetime of offshore mooring chain steel. Mar Struct, 2022;85:103236. DOI: 10.1016/j.marstruc.2022.103236.

1 Introduction

1.1 Motivation

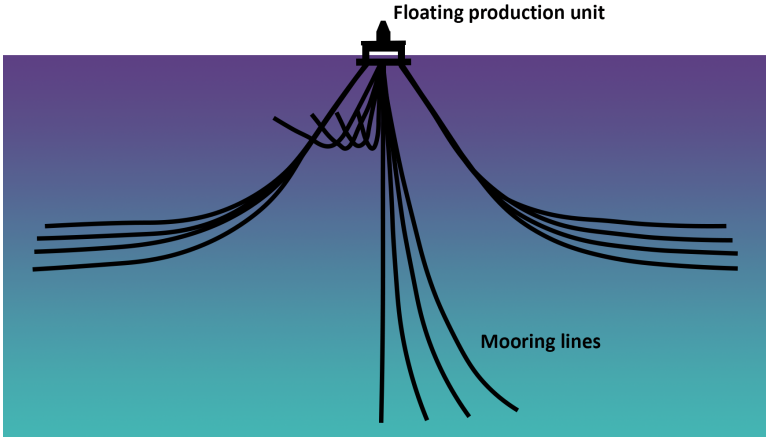

Figure 1: Typical mooring system layout on a hydrocarbon production unit.

Mooring systems are integral structural elements of floating offshore structures used for hydrocarbon and wind energy production and aquaculture. Fig. 1 shows a typical design, where sets of mooring lines are connected to a series of anchors at the seabed, to keep a floating hydrocarbon production unit in position. Failure in multiple mooring lines can cause the unit to move out of position, which may lead to uncontrolled release of hydrocarbons or collisions with nearby units[1]. Thus, safe operation is of paramount importance. Between 2010 and 2013, five cases of mooring single-line fatigue failure were registered on the Norwegian continental shelf[2]. This corresponds to around $3 \cdot 10^{-3}$ failures per line year[2] – considerably higher than the target fatigue failure frequency *for a complete mooring system* of 10^{-3} per year[3]. Some failures were attributed to inadequate design or maintenance for the relevant loading and environmental conditions[2], signaling a need for better understanding of degradation mechanisms. However, there were also cases of incorrect heat treatment during production and operational errors[2].

Determining the appropriate design and replacement interval for a mooring line ultimately involve finding the solution with the lowest cost that maintains a sufficient safety level. Increasing the accuracy of fatigue life es-

timates for a mooring line can promote large material savings, which reduce the financial and environmental costs of operation of a hydrocarbon production unit. Moreover, findings from fundamental research can easily be adapted to other offshore structures and can thus promote material savings in a variety of industries. On the other hand, lowering the maintenance costs of hydrocarbon production systems can lower prices and increase competitiveness of their deliverables towards other alternatives that are produced in less CO_2 intensive manners. This may have a negative impact on the climate.

1.2 Fatigue mechanisms and engineering approaches

Components can fail due to fatigue from cyclic loading at stress amplitudes far below the monotonic strength. The fatigue life is usually considered to consist of two stages: crack *initiation* and *growth*. In smooth steel components, cracks initiate at defects, inclusions or grain boundaries, or due to accumulation of plastic slip in grains that are favorably oriented relative to the applied stresses[4]. Initially, the very small crack is affected by grain orientations and boundaries, but it may eventually grow large enough to assume continuous growth independently of grains, in a direction perpendicular to the local stresses[5]. At this moment, the crack can be considered having completed the initiation process. In smooth specimens, the initiation process may be slow and account for most of a small component's lifetime.

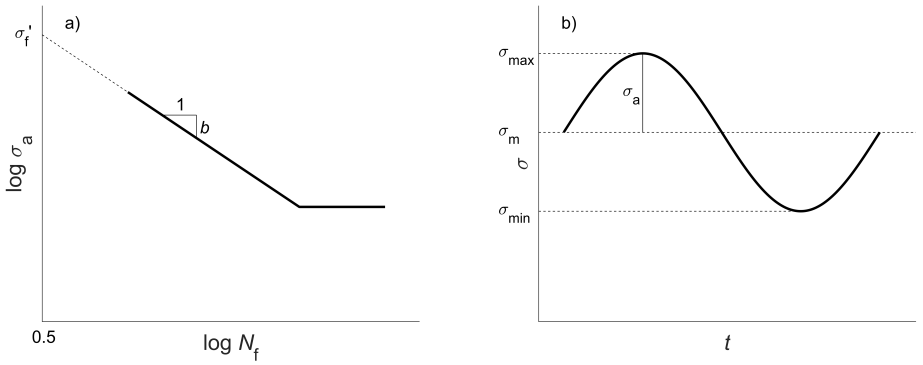

Figure 2: a) An S-N curve based on Basquin's relation and b) definitions for a stress cycle.

The fatigue strength of a material is usually mapped by cyclically loading a number of specimens to failure at different stress levels. Results are presented in logarithmic plots of the total failure lifetime, N_f, as function of the stress amplitude, σ_a. Since the initiation life, N_i, accounts for most of the total lifetime of a small, smooth specimen, one often does not differentiate between them when processing the results. The linear Basquin relation[6] can be fitted to the results, namely

$$\sigma_\mathrm{a} = \sigma'_\mathrm{f}(2N_\mathrm{f})^b. \tag{1}$$

σ'_f and b signify the $N_\mathrm{f} = 0.5$ intercept and the (negative) slope of the line. Such lines are commonly referred to as S-N curves. An example is shown in Fig. 2a. For a very low stress amplitude, measured lifetimes will deviate from the Basquin relation and assume a zero or near-zero slope[4]. This stress amplitude is referred to as the fatigue limit, below which, the material is assumed to have infinite fatigue life.

Some useful definitions for working with fatigue are those of the stress amplitude, mean stress, stress range and stress ratio, respectively

$$\sigma_\mathrm{a} = \frac{\sigma_\mathrm{max} - \sigma_\mathrm{min}}{2}, \quad \sigma_\mathrm{m} = \frac{\sigma_\mathrm{max} + \sigma_\mathrm{min}}{2}, \quad \Delta\sigma = 2\sigma_\mathrm{a}, \quad R = \frac{\sigma_\mathrm{min}}{\sigma_\mathrm{max}}. \tag{2}$$

σ_max and σ_min are the maximum and minimum stress. Fig. 2b illustrate the definitions for a stress cycle.

Due to the heterogeneity of the microstructure and defects in a material, fatigue initiation is not a deterministic phenomenon, and fatigue lives will be somewhat scattered. For engineering purposes, design S-N curves are shifted to represent low failure probabilities. However, for large components or systems thereof, shifting the S-N curve alone does not account for the *size effect*, which denote the increase in probability of failure for the system due to the higher likeliness that it contains a critical weakness. In *weakest link* theory, the size effect is considered by calculating an effective stress amplitude[7],

$$\bar{\sigma}_\mathrm{a} = \left(\frac{1}{V_0} \int_V \sigma_\mathrm{a}^\beta \mathrm{d}V \right)^{1/\beta}. \tag{3}$$

V denotes the volume, V_0 a reference volume and β the Weibull shape parameter, a measure of the scatter.

Another issue that arises from the random nature of fatigue, is the challenge of fitting an S-N curve if some fatigue tests "run out". That is, if failure is not observed in time before the test must be discontinued for practical reasons. By *maximum likelihood estimation* (MLE) both completed and run-out tests can be accounted for by maximizing the *log-likelihood* function[8],

$$\mathcal{L} = \sum_{i=1}^{k} \left[\delta_i \log p_{\mathrm{f}} + (1 - \delta_i) \log P_{\mathrm{s}} \right], \tag{4}$$

for all k tests. Here, δ is an indicator function, which takes the value 1 if there is crack initiation in an element, and 0 if there is not. p_{f} is the probability density function for failure, and P_{s} is the cumulative distribution function for survival.

If a static stress is superposed on the dynamic stress, this is referred to as the mean stress (see Fig. 2). The static stress can originate from applied loads or residual stresses in a component. A positive mean stress can shorten the fatigue life by increasing the maximum stress in cycle and thus create a higher driving force for opening and growing a crack[5]. Mean stresses are typically accommodated in fatigue predictions by use of some empirical relations to estimate an equivalently damaging stress cycle with zero mean stress. Such relations include those of Goodman[9], Morrow [10], Gerber [11], Walker[12] and Smith, Watson and Topper [13].

If the stress state is multiaxial, fatigue behavior might be affected, and predictions further complicated[4, 14]. However, since the current work considers stress states that are largely uniaxial, the topic will not be discussed further.

Notches in a component can act as macroscopic stress raisers that affect the initiation mechanisms that happen on the grain scale. Due to the stress gradient in the material under a notch, the fatigue process zone is subjected to a decreasing level of stress, and fatigue initiation is not controlled solely by the surface stress amplitude[4, 15]. To accommodate this, Taylor alternatively considered the stress state at some "critical distance" below the surface for fatigue predictions[16]. This approach is easily applicable

to finite element analysis (FEA) results. Other approaches include those of Peterson and Neuber, who based empirical relations on the notch radius[4], and Siebel and Stieler, who considered the relative stress gradient[15].

σ'_{f} is typically significantly higher than the ultimate tensile strength of the material[4]. Thus, it can be seen from Fig. 2a that Basquin's relation cannot hold for low N_{f}, where the ultimate tensile strength is exceeded. The strain-based modification of Basquin's relation by Coffin[17] and Manson[18] includes a significant plastic strain component for the *low-cycle* fatigue region:

$$\varepsilon_{\mathrm{a}} = \varepsilon_{\mathrm{ae}} + \varepsilon_{\mathrm{ap}} = \frac{\sigma'_{\mathrm{f}}}{E}(2N_{\mathrm{f}})^b + \varepsilon'_{\mathrm{f}}(2N_{\mathrm{f}})^c. \tag{5}$$

Here, $\varepsilon_{\mathrm{ae}}$ and $\varepsilon_{\mathrm{ap}}$ denote the elastic and plastic strain amplitude, respectively. $\varepsilon'_{\mathrm{f}}$ and c are equivalent to the Basquin parameters, but for a strain-life plot. E is the elastic modulus of the material.

During cyclic loading above the yield stress, materials can experience cyclic hardening or softening, raising or lowering the stress-strain curve. Moreover, if a material is loaded past its yield stress, σ_{max} will be limited by the plastic stress-strain curve, which can lead to instant shifting of σ_{m} for the stress cycle. Mean stresses can also transiently relax and redistribute during cyclic straining[19].

For components subjected to variable-amplitude loading, the fatigue damage caused by a stress cycle will vary based on the magnitude of the stress amplitude. This is traditionally accommodated by summing up the relative damage contributions from the number of cycles, n, from k stress levels using Miner's law of cumulative damage[20]:

$$\sum_{i=1}^{k} \frac{n_i}{N_{\mathrm{f}i}} = 1. \tag{6}$$

The resistance for propagating a crack is lower than for initiating one. Stress cycles below the fatigue limit can contribute to fatigue damage that has been initiated at a higher stress level and must thus be included in the damage sum. A *cut-off limit* signify a stress level, below which, stress amplitudes

are too low to even propagate a crack and can thus be disregarded in fatigue analyses.

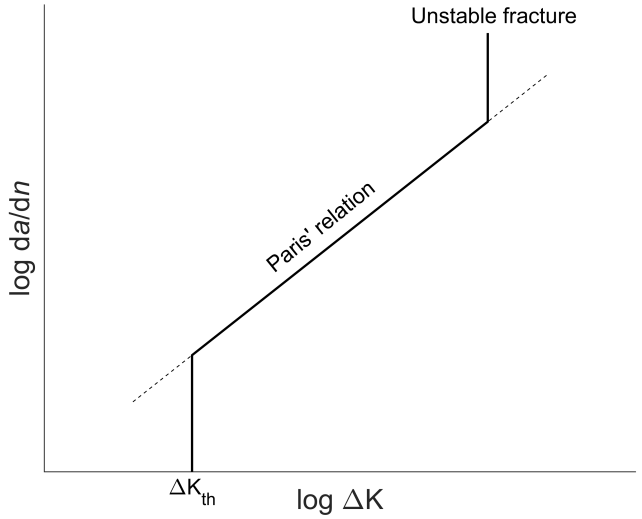

Figure 3: Idealized model of fatigue crack growth rate.

For calculating the growth rate of an initiated fatigue crack, the stress intensity factor range is the primary variable to consider[4],

$$\Delta K = F\Delta\sigma\sqrt{\pi a}. \tag{7}$$

Evidently, a higher crack depth, a, leads to a higher ΔK. F is a geometry factor. Paris[21] found that the crack increment per cycle could be approximated by a linear dependency on ΔK in a logarithmic plot, namely

$$\frac{\mathrm{d}a}{\mathrm{d}n} = C(\Delta K)^m, \tag{8}$$

where C and m are material parameters. The relation is illustrated in Fig 3 and shows that growth of a fatigue crack is initially slow, but accelerates as the crack grows. Below a threshold stress intensity factor range, ΔK_{th}, there is no crack growth. Fatigue crack growth is relatively deterministic

in nature, and less scatter is observed in crack growth lives than in crack initiation lives for smooth components.

Mean stresses affect crack growth by controlling the maximum stress intensity factor, $K_{\max}$, and the portion of stress cycle for which the crack is closed. Cracks in brittle materials may close at zero load and experience no growth for the compressive part of a stress cycle[4]. However, for ductile materials, this behavior may vary due to plastic effects at the crack tip[4]. Similar to the effect that was described earlier for fatigue initiation, overloading of an initiated fatigue crack can lead to shifting of R, closure of the crack and retardation of the crack growth rate[4].

When a steel component is submerged in a corrosive medium, like seawater, and subjected to cyclic loading, fatigue process mechanisms and rates can change compared to in air. Over time, corrosion can roughen the component surface and create locally stress-raising pits, which reduce the fatigue initiation life in a similar way as notches do. Once a fatigue crack has initiated in a chain link, further fatigue crack growth can be enhanced by hydrogen embrittlement, anodic or film-rupture facilitated dissolution at the crack tip or cohesive strength weakening from Cl^- ions[5, 22, 23]. Since corrosion is a time-dependent mechanism, load frequency becomes an important parameter to consider[5]. Mean stresses control the duration of the periods when a corrosion fatigue crack is open and the magnitude of maximum tensile strains, which can affect corrosion mechanisms. Dissolution by corrosion can expose virgin layers of material that have not been affected by previous plastic overloads and thus may have higher mean stresses. Fatigue and cut-off limits may be reduced or erased due to the assisting effects from corrosion.

Design lives for submerged offshore structures can range up to several decades. For such timescales, test programs on corrosion fatigue are impractical to conduct at natural speeds. Consequently, most tests are accelerated. This leaves researchers challenged by the task of interpreting results of time dependent degradation mechanisms in light of in-service conditions, while accounting for interactions between the different mechanisms[5, 24, 25]. Corrosion fatigue process modeling tasks are further complicated by the difficulty of obtaining meaningful measurements of mechanical states and electrolyte chemistry in corrosion pits and fatigue cracks[5].

The current work is not focused on corrosion fatigue, but rather on geometric effects from corrosion of the substrates which fatigue cracks can initiate from.

1.3 Fatigue of offshore mooring chains

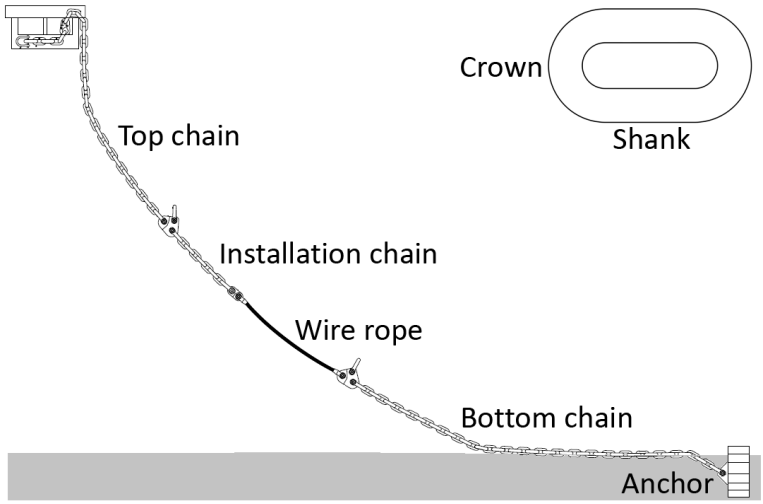

Figure 4: Typical layout of a mooring line. Reprinted from [26] with permission from Equinor.

As shown in Fig. 4, a mooring line can consist of different segments made up of either chain, steel wire or synthetic fiber rope. The current work is focused on fatigue of chains. A single chain link is made up of two curved and straight parts, referred to as "crowns" and "shanks", respectively. The current work deals only with so-called "studless" or "open" chain links[27], which do not have studs placed between the shanks of the links. From commonly used chain alloys, the low-alloy R4-grade steel[27] is considered. This has a minimum yield stress and tensile strength of 580 and 860 MPa, respectively[27]. The chain links do not receive any corrosion-protective coating before being installed for service.

Offshore mooring chain links are produced by bending hot-rolled bars to form the specified loop geometry, and then flash welding the ends of the bars together. A minimum breaking load (MBL) is specified based on the steel

grade and chain diameter[27]. All chains undergo proof load testing to 70% of the MBL before installation to service[27]. This process deforms the chain links plastically and induces compressive residual stresses in the crowns upon unloading[28, 29] that are superposed on stresses from operational loads. During operation, chain links are exposed to dynamic loads from wave loads on the floating unit[30]. In addition, the chains are subjected to mean loads from mooring line pretensioning, wind loads and the dead weight of the mooring line[30]. The loads exerted on a chain link in service can vary both on an hourly[30] and a seasonal[30–32] scale.

Figure 5: Photograph of corrosion pits on an offshore chain link. Reprinted from [26] with permission from Equinor.

Offshore mooring chains can fail due to long-term degradation from the combined action of corrosion and fatigue[2]. General corrosion and interlink wear can reduce cross-sectional area of a chain link, effectively increasing nominal stresses. Inhomogeneities in surface chemistry, as well as microbiological activity, can lead to localized corrosion attacks that produce macroscopic pits[26, 33], as seen in the photograph in Fig. 5. The corrosion pits facilitate faster fatigue crack initiation and reduced fatigue life for a chain link[34, 35]. The severity of corrosion attacks on chain links can vary considerably along a mooring line, possibly due to differences in oxygen concentration, levels of nutrients for microorganisms and electrode potential from cathodic protection systems on the connected floating structure[36, 37].

The corrosion mechanisms are not yet sufficiently understood to accurately predict rates and extent of the localized corrosion attacks.

Several test programs on fatigue behavior of R4-grade steel have been conducted in the recent years. S-N data for smooth specimens in air and salt water environments have been collected[38–41]. A number of extensive test campaigns on full-scale segments of corroded offshore mooring chain have been carried out[34] at relatively high cyclic loads and load frequencies. The most pronounced hotspot for fatigue initiation in a chain link has been found to be on the outside of the crown[34]. This indicates that stresses from the applied loads in the tests have exceeded the magnitude of the compressive residual stresses, at least partly. However, representative stress analyses of chain links in service, to verify that testing loads and observed hotspots are relevant, are lacking. Such analyses require complex dynamic load simulations of a complete mooring system to be performed.

Researchers have reached contradictory conclusions on the importance of mean loads for the fatigue lives in full-scale tests of chain segments[30, 34, 42, 43]. The observation of cyclic softening and mean stress relaxation (MSR) for R4-grade steel at plastic strain amplitudes[38] can further complicate the discussion.

Accelerating the full-scale tests by increasing the applied load and load frequency compared to in-service conditions reduces the relative impact of corrosion on the fatigue crack initiation and growth processes. Moreover, all tests have been run at constant load, and has thus not been capturing any effects of load variations or periods of very low cyclic loads.

The current DNV design standard for offshore mooring chains[3] contain S-N design curves that have been deducted from results of full-scale tests[1, 44], some lasting up to around $2 \cdot 10^6$ cycles. Design curves are extrapolated to lower loads and longer lives by assuming a constant slope of $b = -3.0$. Thus, for these low loads, which may be highly relevant for degradation of chains in service, the design curves are not directly related to any fatigue test data. Moreover, the effect of elevated load frequencies in the tests has not been considered. The DNV standard does not consider the mean service loads when design lives are to be calculated.

The current review indicates that prioritized research areas should include:

- Prediction and monitoring of general and microbial corrosion rates.
- Fatigue crack initiation on *corroded*, R4-grade steel.
- Analysis of stress states in chain links under actual service loads.
- Corrosion fatigue behavior for such stresses in a variable-amplitude-loading regime and for realistic load frequencies.
- Evolution of residual and mean stresses and their effect on fatigue of corroded chain links.

1.4 The KPN LifeMoor project

The current work was performed in the project KPN LifeMoor. The project has been a collaboration between the research organization SINTEF and the Norwegian University of Science and Technology (NTNU) funded by the Norwegian Research Council (NRC) and industry partners, primarily the energy company Equinor. The goals of the project have been to improve lifetime estimates of offshore mooring chains in service in the North and Norwegian Sea through better understanding of degradation mechanisms, as well as to allow for continuous updating of lifetime estimates through monitoring and probabilistic methods. The lifetime assessments have been mostly focused on corrosion fatigue.

Compilation of the full-scale test results has been performed in the project[34], and NTNU has also contributed to the testing. In addition to registering the fatigue life, non-destructive testing (NDT) by magnetic particle inspection (MPI) has also been used on some chain segments after testing to document any secondary cracks that did not result in fracture of a chain link. For some tests, detailed 3D scans of the chain link surfaces have been generated.

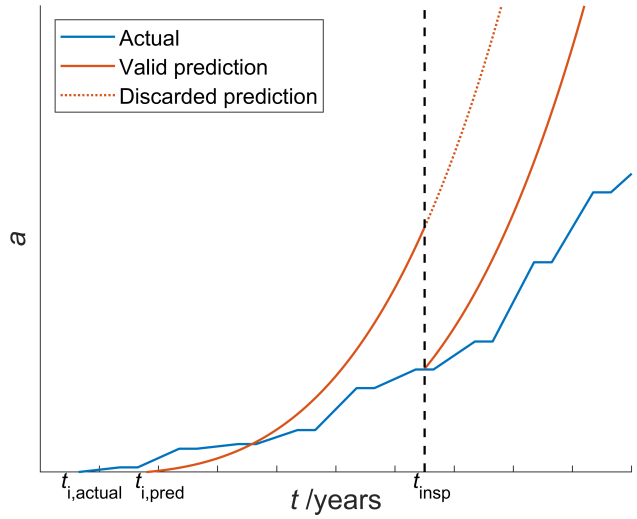

Figure 6: Hypothetical fatigue crack growth for a crack in an offshore mooring chain link. Prediction curve is updated after the inspection at t_{insp}.

The goal of the LifeMoor project has ultimately been to develop a better understanding of the actual condition of the chain at a given time. The fatigue life of a chain link in service can be illustrated by initiation and growth of the most critical fatigue crack, as shown in Fig 6. Over time, t, the actual crack depth may deviate from the predicted one, due to differences between the predicted and actual fatigue crack initiation lives, $t_{\mathrm{i,pred}}$ and $t_{\mathrm{i,actual}}$, and crack growth rates. Regular monitoring of the chains could give valuable status updates and allow for recalibration of fatigue predictions, as the inspection event at t_{insp} shows. However, in-situ crack detection in offshore mooring chains is difficult. Monitoring the states of the corroded surfaces seems more feasible. Thus, understanding fatigue crack initiation behavior from surfaces damaged by corrosion is of great importance and has been the primary focus of the current work.

1.5 Research objectives

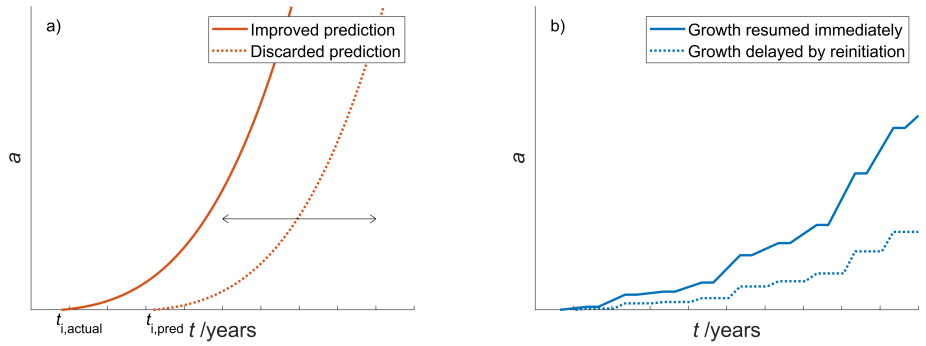

Figure 7: Variations in fatigue lives in an offshore mooring chain link due to a) variations in initiation life and b) delayed crack growth after long periods of very low loads.

Based on the review in section 1.3, the motivation and goals for the current work are listed below.

Part 1

The severity of localized corrosion attacks has a significant impact the fatigue life of a chain link[34]. Since the extent of increased stresses due to a corrosion pit is limited, the crack growth rate should remain largely unaffected, as illustrated in Fig. 7a). The fatigue initiation life in corroded chain links has not yet been quantified, even though it may be important for understanding the corrosion fatigue process and deciding how full-scale test results should be extrapolated to in-service conditions. The goals of Part 1 of the current work are therefore to

1. develop an appropriate method for measuring the fatigue initiation life from corroded surfaces.
2. determine the ratio of crack initiation to growth life for specimens extracted from corroded surfaces of R4-grade-steel offshore mooring chain links.
3. establish a method for predicting initiation lives of mooring chain links based on S-N data obtained from corroded surfaces of small specimens.

Part 2
The evolution of stress-strain behavior for R4-grade steel under cyclic loading has only been studied for plastic strain amplitudes. If MSR occurs at lower strain amplitudes, for example at those produced in a corrosion pit in a chain link at service loads, it has the potential to reduce the compressive residual stresses from proof loading. This too can reduce the fatigue initiation life, like Fig. 7a) shows. In Part 2 of the current work, the focus is to

1. quantify the degree of MSR in R4-grade steel at an elastic stress amplitude.
2. determine the influence cyclic softening and MSR on fatigue initiation in pit-like notches.

Part 3
All full-scale tests have been run at constant load amplitudes, and the effect of periods of low loads on the corrosion fatigue process has not been studied. During calm summer periods, one could imagine that any erasure of fatigue damaged material, or blunting of a fatigue crack tip, from corrosion could potentially extend the fatigue life of a chain link, since the crack must reinitiate when the high loading resumes. This scenario is illustrated in Fig. 7b). In part 3 of the current work, effects of long periods of corrosion and no fatigue load on remaining lives of fatigue cracks in R4-grade steel are studied. The main goal is to

1. determine if calm summer periods give potential for lifetime extension for mooring chains in service compared to fatigue results obtained from full-scale tests.

The research topics in the current work were studied by combining experimental fatigue testing programs with FEA. Other tools, like 3D surface scanning, full-field fatigue crack detection by digital image correlation (DIC)[45] and statistical results processing by means of MLE were used to complement the study. Emphasis was put on combining simple techniques to create powerful prediction methods that could increase the value of already available full-scale test data.

2 Summary

Part 1
Qvale P, Zarandi EP, Ås SK, Skallerud BH. Digital image correlation for continuous mapping of fatigue crack initiation sites on corroded surface from offshore mooring chain. Int J Fatigue, 2021;151:106350. DOI: 10.1016/j.ijfatigue.2021.106350.

In part 1, specimens were extracted from the surface of corroded chain links and fatigue tested in air in three-point bending. DIC was used for the first time to monitor fatigue crack initiation on such corroded surfaces. Several initiation sites were identified in each specimen. The surfaces were 3D scanned, and FEA was used to calculate the local stress at each initiation site. MLE was used for an S-N curve regression, which also statistically included stress results from the regions of the surfaces where no cracks initiated. From testing of only four specimens, it was possible to identify fourteen initiation sites, as well as large areas with no initiation. From this it was possible to construct an S-N curve with low uncertainty and scatter. The method and S-N curve is deemed appropriate for fatigue initiation predictions for chain links in air environment. The first cracks initiated at 13-24% of the total lifetimes of the specimens. This indicates that crack growth is an important phase to focus on when extrapolating full-scale test results.

Part 2
Qvale P, Zarandi EP, Arredondo A, Ås SK, Skallerud BH. Effect of cyclic softening and mean stress relaxation on fatigue crack initiation in a hemispherical notch. Fatigue Fract Eng Mater Struct 2022;1-17. DOI: 10.1111/ffe.13834.

In part 2, the same fatigue test and DIC setup as in part 1 was used to study fatigue crack initiation in machined, hemispherical notches, representing idealized geometries of corrosion pits. The entire notch profile was monitored. Initiation was predicted and measured near the mouths of the notches, where the stress and strain amplitudes were the highest. A complementary, strain-controlled fatigue test revealed significant MSR in R4-grade steel even at a stress amplitude below the cyclic yield. For the hemispherically notched specimens, accuracy of initiation life predictions improved when cyclic softening and MSR were accounted for, compared to using only

the monotonic stress-strain curve. This observation is considered important in the current discussion of the mean stress effect on fatigue lives of mooring chains. For initiation lives above 100,000 cycles, scatter in the S-N data and residual stresses from machining of the notch made predictions for the notched specimens less accurate.

Part 3

Qvale P, Nordhagen HO, Ås SK, Skallerud BH. Effect of long periods of corrosion on the fatigue lifetime of offshore mooring chain steel. Mar Struct, 2022;85:103236. DOI: 10.1016/j.marstruc.2022.103236.

In part 3, two test programs of alternating corrosion and fatigue phases were conducted to replicate seasonal load variations on mooring chains in service. In the first test program, periodic corrosion phases were accelerated by anodic polarization. It was observed that cracks quickly initiated from the precorroded surfaces and grew too deep for the crack tip to be severely affected by the polarization. Thus, this way of accelerating corrosion is deemed inappropriate for studies of corrosion effects on fatigue cracks. The growth of shallow cracks that experienced extensive crack tip blunting by corrosion was, however, not significantly retarded by the periods of corrosion. In the second test program, fatigue-cracked specimens were exposed to eight months of natural corrosion to study the effect on the remaining lives. No marked effect was observed. Based on previous studies in the literature, it can be assumed that cracks with tips blunted by corrosion are as critical for the fatigue life as sharp, uncorroded cracks. Thus, no beneficial effect on fatigue lives of mooring chains can be expected from calm summer periods, and no positive correction factor can be applied to full-scale test results when employing them to in-service conditions.

3 Complementary stress analysis of chain link

The small-scale test programs in the current work have been performed at sufficiently high loads to be completed within practical time frames. The same applies to the full-scale tests. To interpret and evaluate the relevance of results from the current work, a comparison of stress states in chain links in service and those of the tested specimens and chain links would be very valuable. A comprehensive case study of dynamic loads on mooring lines of a semi-submersible platform has recently been completed[31]. The current section presents stress analyses based on the load output from the case study. The surface stress levels are then compared to those of the tests, while disregarding stress concentrating effects from any notches or corrosion pits.

In [31], historic hindcast data of Norwegian Sea sea states from year 1958 through 2018 were used to calculate the dynamic loads for a semi-submersible hydrocarbon production unit moored with 16 lines. In the current work, the top chain of line number 13 is considered, which was calculated to have the most fatigue-critical load history[31]. The fatigue damage was evaluated using an S-N approach based on the nominal tension stresses in the shanks of the chains. The chain diameter used in the dynamic load analysis was 142 mm. The authors of [31] have commented that the unit in the case study did not obtain a high level of fatigue damage during a typical design life. For this reason, the following load states have been considered *for a particularly fatigue-damaging year* (1993): The load cycle that resulted in the highest accumulated fatigue damage during the year, as well as the single load cycle with the highest load amplitude. All load data were extracted from the dynamic load analysis by the authors of [31]. In order to investigate a scenario with a higher level of fatigue damage, stresses were also calculated for a smaller, Ø114 mm chain link. In this additional stress analysis, load ranges from the dynamic load analysis were used directly, but the mean loads were scaled down proportionally to the MBL of the chain, to approximate identical levels of pretensioning as in the Ø142 mm case.

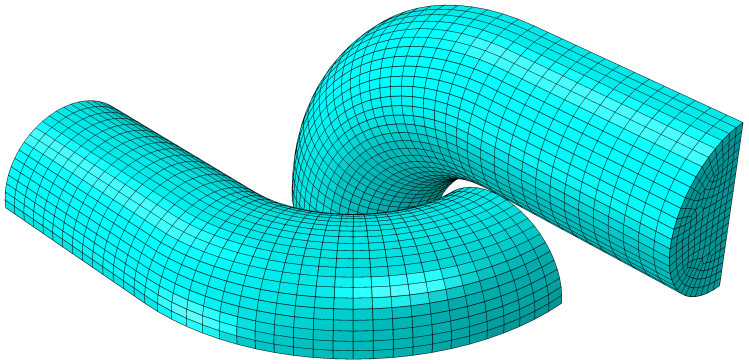

Figure 8: Meshed finite element model of contact between two chain links.

Contact between halves of two chain links was modeled using two planes of symmetry in ABAQUS 2017. Fig. 8 shows the first-order hexahedron element mesh. For the contact condition, the normal behavior was modeled as hard, and the tangential behavior was modeled with a friction coefficient of 0.3[46]. A monotonic material model for R4-grade steel from [38] was used. Proof loading at 70% of the MBL was modeled before the test loading. Since the proof loading process has been found to dominate the values of residual stress in axial direction of the chain link profile[29], preceding heat treatments were not included in the stress analyses.

The stresses for the specimens in Part 1-3 of the current work were calculated using the FEA models described in the respective articles.

Fig. 9 shows the stress amplitudes and mean stresses for the specimens from Part 1-3 and outside of the crown of the chain links from the full-scale tests and chain links in service. Two markers are displayed for each diameter of chain in service: The marker at the lowest stress amplitude shows the most fatigue-damaging stress state, and the other marker shows the highest stress state. Each load level in the test programs from Part 1-3 is displayed with a separate marker.

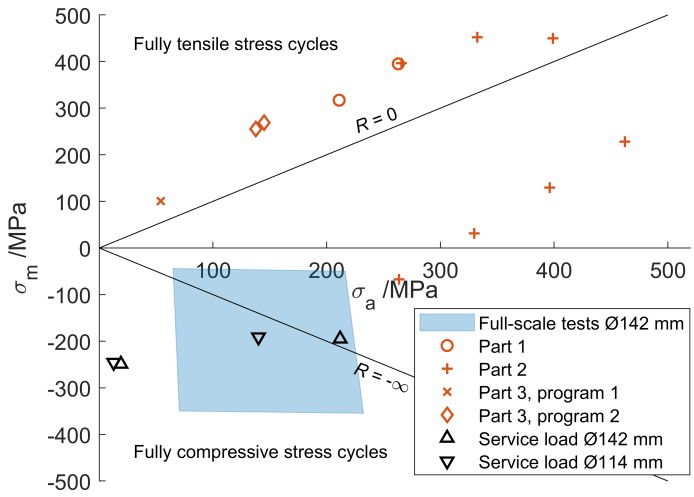

Figure 9: Surface stresses (from FEA models without pits or notches) in specimens from part 1-3 compared to surface stresses outside of the crown of pit-free chain links from full-scale tests and in service.

The full-scale tests have been performed with different chain diameters, with load ranges from 6 to 20% of MBL and mean load from 6.4 to 20% of MBL[34]. The region in Fig. 9 that approximately encompasses the pool of full-scale test stress conditions was identified by performing FEAs of Ø142 mm chain loaded to these limits of load amplitude and mean load.

Since the FEAs do not take into account the non-Masing or any transient stress-strain behavior of R4-grade steel that was discussed in [38] and Part 2 of the current work, especially the calculated mean stresses might be inaccurate. Nevertheless, Fig. 9 provides a basis for a crude comparison of the different stress states.

From Fig. 9, it is apparent that the full-scale tests represent well the mean stresses and the highest stress amplitudes found for the current chain links in service. The accumulated most fatigue-damaging stress amplitude that was identified in [31] is not well represented. However, in [31], an S-N curve without any fatigue or cut-off limit was employed to determine fatigue damage. Corrosion fatigue behavior of chain links subjected to very low

stress amplitudes needs to be studied before the most fatigue-damaging load can be correctly identified.

The specimens from the test programs in Part 1-3 generally have higher mean stresses than the chains in service. Stress amplitudes in Part 2 seem to be higher than in chains in service, while Part 1 and 3 have stress amplitudes that are more similar to highly loaded chains in service. However, the low stress calculated for the first test program in Part 3 might be somewhat misleading, since the circumferential notch in these specimens lead to a significant increase in effective cross-sectional stresses that is not visible in the nominal stresses in Fig. 9.

Implications of the results are further discussed in the following section.

4 Discussion

4.1 Fatigue crack initiation in offshore mooring chains

Conducting small-scale fatigue tests is a relatively inexpensive method for isolating and studying effects on degradation in ways that would be impractical to achieve through full-scale tests. However, creating conditions that are similar as for chains in service can be a challenge. In the current section, relevance of the test programs in Parts 1-3 to fatigue initiation of mooring chains is discussed in light of the presented stress comparison.

It has already been pointed out that mean stresses in the small-scale test programs were higher than in chains in service, when disregarding notches and corrosion pits. The reasons for the high mean stresses were mostly practical: three-point bending fatigue setups were selected for their similar stress amplitude distribution to mooring chain crowns and sensitivity of their stiffness to cracks. Such setups cannot accommodate negative R values. However, as discussed in Part 2, mean stresses in a stress raiser, like a notch and corrosion pit, can redistribute on the first loading or relax transiently during the cyclic loading. Thus, effective mean stresses might be more similar than Fig. 9 indicates. Consequently, it can be argued that the stress amplitude is the most relevant quantity to compare.

It has been shown that for chains in service, the small-scale tests represented well the highest stress amplitudes, which occur relatively infrequently. The representation was poorer for the most damaging, very low stress amplitudes. However, as mooring chains are also subjected to stress amplitudes that lie between these two extremes, and such stress amplitudes have potential to cause significant damage due to their magnitude or quantity, the relevance of the small-scale tests to damaging stress cycles should not be dismissed until a cut-off limit has been established for corroded R4-grade steel in a service environment.

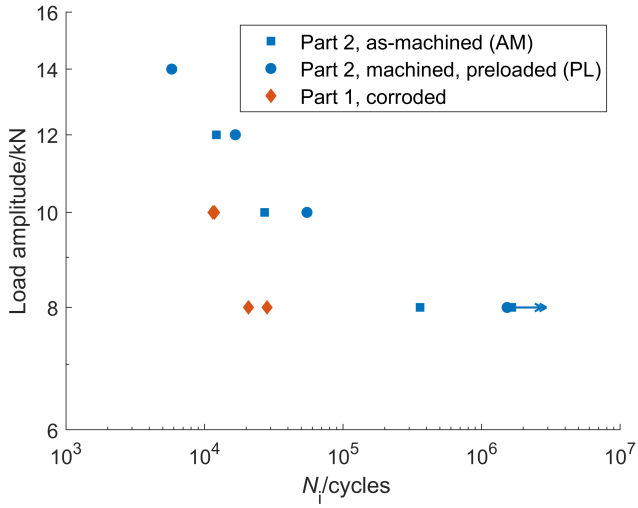

Figure 10: Fatigue initiation lives for the naturally corroded and machined specimens from test programs in Part 1 and 2.

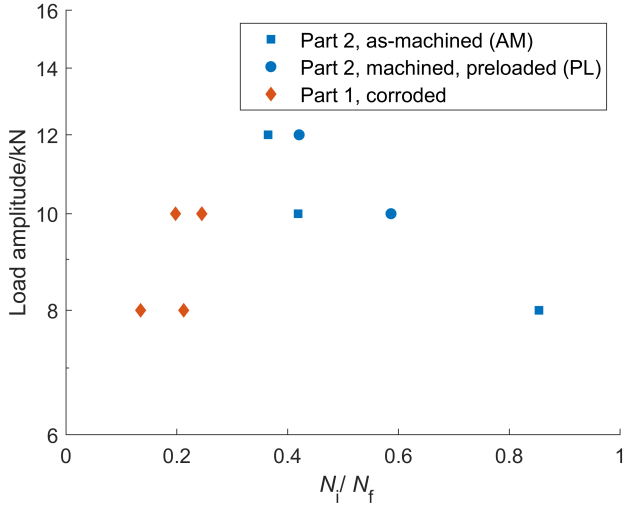

Figure 11: Ratio of initiation lives to total lives for the naturally corroded and machined specimens from test programs in Part 1 and 2.

In Part 1, fatigue crack initiation lives were measured for surfaces retrieved from offshore mooring chains. Crack *initiation* was defined by the lowest inter-node displacement, or strain increase (1%), across a crack plane that could be detected through the noise in the DIC signal. Possible sources of errors and noise include obstructed views of the metal surface by DIC paint and remaining corrosion products, as well as suboptimal image filtering. A paint-free DIC setup has been demonstrated to yield higher strain sensitivity[47] and could possibly have detected cracks at an even earlier stage.

In Fig. 10, the initiation lives from the corroded specimens are compared to those measured from specimens with hemispherical, machined notches at similar load levels in Part 2. Arrows mark run-out tests. For the corroded specimens, the initiation lives are significantly lower than for the machined ones – almost two orders of magnitude for the lowest load level. The reduction in initiation life for the corroded specimens is presumably caused by roughness or micro-scale surface features in the corrosion pits. The stress concentration factors might also have been higher for some corrosion pits than for the machined, hemispherical notches. The comparison of initiation lives show that S-N data collected from fatigue tests of smooth specimens cannot be used directly for corroded surfaces.

Since a fatigue crack becomes increasingly independent of the surface state as it grows, crack growth lives are more similar between the corroded and machined specimens. Consequently, the ratio of initiation life to total life is lowest for the corroded specimens, at 13-24%, as shown in Fig. 11. In a chain in service, the crack growth life would be extended by the larger cross section that a fatigue crack has to traverse. Moreover, both crack initiation and growth lives have been found to be shorter in salt water for R4-grade[39, 40, 48] and other steels[5, 22]. Moreover, the discussion of the $N_\mathrm{i}/N_\mathrm{f}$ ratio for a crack in a mooring chain crown is also complicated by the crack growing in stress field that is initially at least partly compressive (see Fig. 9) and then turns more tensile at the crack tip as the crack grows[49]. However, by using the S-N curve from Part 1, it should be possible to estimate the initiation life and $N_\mathrm{i}/N_\mathrm{f}$ ratio for a chain link fatigue tested in air. Improvement of estimates for fatigue tests in salt water is discussed in the subsequent section.

Even though Fig. 10 shows that machined specimens are not suitable for measuring initiation lives that are directly applicable to corroded surfaces, the work performed in Part 2 is still relevant for mooring chain fatigue. Part 2 showed that there is a significant MSR effect in R4-grade steel loaded at elastic stress amplitudes, and that accuracy of fatigue predictions can be increased when taking this into account. Data on MSR can aid future investigations on effects from mean stresses on the fatigue initiation life of corroded surfaces. If MSR also occurs below corroded mooring chain link surfaces, it could reduce the effect of the initial compressive mean stresses on fatigue initiation. This could lead to nonconservative initiation life predictions if not considered. Even if Fig. 9 shows that nominal stress amplitudes are higher in the specimens from Part 2 than in chains in service, it is apparent from Fig. 10 that corroded surface of a chain has more critical stress raisers than the machined notches in Part 2. Thus, local stress amplitudes in corrosion pits in chains in service might still be similar to those in the notches in Part 2.

The discussion in Part 2 is based on a very limited amount of test data. Higher confidence in the conclusions could be obtained if more relevant tests could be performed and a more physically based material model could be employed for the instant and transient stress-strain behavior. Future testing should involve better control or elimination of machining stresses, for example by stress-relieving heat treatments.

In Part 3, no indication was found of that calm summer periods greatly influence the remaining lifetime of specimens with fatigue cracks. The suggested explanation was that a corroded crack is as critical as a noncorroded one with respect to the stress state at the crack tip. Fig. 9 shows that nominal stress amplitudes in the specimens in Part 3 are similar to the highest ones in chains in service. But even at lower stresses, the logic of the explanation holds, and no great effect of calm periods should be expected.

One could imagine that a crack that have initiated from a corrosion pit can close and arrest if it grows into a compressive stress field in the crown of a chain link. Crack dissolution by a long period of corrosion could then possibly reopen the crack, allow for local relaxation of the compressive stresses and promote a further increment of crack growth. Thus, in this scenario, a corrosion pit or a blunted crack is more critical for fatigue initiation than a sharp crack.

Another proposed, hypothetical case could be if the initial yearly growth increment for an initiated crack is smaller than the yearly corrosion rate[50]. If a surface is so severely corroded that the stress state is not worsened locally by a year of corrosion – that is, if the stress concentration on the pitted surface has converged – lifetime extension from erasure of the fatigue crack could be expected. However, rather than studying this particular, hypothetical case, efforts might be better spent on studying the effects of corrosion under high service loads and realistic load frequencies.

4.2 Extension of techniques to full-scale tests

Monitoring of fatigue initiation during testing of corroded offshore mooring chain segments can be a challenge, due to the many possible initiation sites. However, as shown in Part 1, this property also allows for increased learning from each test. The high cost of full-scale tests of mooring chains should motivate researchers to maximize the results output. In the current section, extension of techniques used for the small-scale tests in Part 1 to full-scale tests is discussed.

Part 1 combined different simple tools in a powerful manner to construct an initiation life S-N curve: stress analysis using FEA on 3D surface scans, crack initiation using DIC and probabilistic post processing using MLE. The result was an S-N curve that was accurately defined from only four specimens, because it was based on measurements from the entire corroded surfaces. Moreover, due to the continuous monitoring with DIC until failure of the specimens, the S-N curve extended to initiation lives far longer than the first initiations.

The generated S-N curve applies to corroded surface elements – not components. Thus, it can be used to predict surface element survival probabilities for elements in a chain link. Probabilities for all elements in a chain link can then be multiplied to find the survival probability of the whole chain link.

In Part 1, specimens were fatigued in air. Thus, the S-N curve is only applicable to corroded chain links in air environment. Extending the technique for use on full-scale tests would facilitate generation of an S-N curve that is one step closer to chains in service. However, as dispersion of iron oxides from the corroding chain links could limit visibility in the water and thus the usability of DIC, some other full-field technique to detect fatigue initiation

would have to be employed. An alternative could be to calculate fatigue crack growth "in reverse" from the final fatigue fracture, as well as from secondary cracks detected with MPI. Studies on crack growth predictions for mooring chains is currently ongoing[51, 52]. The estimated initiation lives could be combined with stress analyses on 3D scans of the chain links to create an initiation S-N curve. Taylor's critical distance method could be employed for increasing the accuracy. Application of the S-N curve to stress analyses of surface scans from chains in service would be technically possible. Nevertheless, the results would be non-conservative, because of the lower load frequency of chains in service compared to the full-scale tests, and thus higher impact of corrosion.

Even if accurate estimates of initiation lives in the full-scale tests would be difficult to achieve – due to a lack of appropriate models for crack growth in compressive stress fields from irregular surface geometries – simply building more systematic databases of secondary cracks and local stress states could be helpful for quantifying initiation lives. A high density of initiated cracks in highly stressed areas could statistically indicate that a large portion of the fatigue life is spent on crack growth, since the first initiated crack would otherwise grow to fracture before others could initiate.

5 Conclusions

The current work involved different aspects of fatigue initiation from corroded surfaces of offshore mooring chains made from R4-grade steel. Some key findings are listed below.

- Small-scale specimens with corroded surfaces have been fatigue tested in air. Fatigue initiation was measured from strain fields measured by DIC. Fatigue cracks initiated after 13-24% of the total fatigue lives of the specimens. A method for generating a S-N initiation curve for corroded surfaces has been established and executed. Being surface-element based, the resulting S-N curve can be applied to a mooring chain link to predict its probability of failure.
- From the first load cycle to the half-life of a specimen, the mean stress have been found to relax by 49% during loading at a stress amplitude just below the plastic yield stress. Taking this observation and cyclic softening into account increased the accuracy of fatigue initiation life predictions for specimens with hemispherical notches. The cracks initiated near the mouths of the notches.
- By exposing specimens with fatigue cracks to long periods in corrosive environments, it was found that crack tip blunting from corrosion did not extend the remaining lives significantly when fatigue loading was resumed. Thus, any blunting of fatigue cracks in offshore mooring chains during calm summer months cannot be expected to have a life-time extending effect. Acceleration of corrosion by anodic polarization of the specimens was found not to result in realistic appearances of the crack surfaces.
- FEA stress calculations based on a dynamic load analysis of an offshore mooring system showed that the stress amplitudes in the small-scale tests in the current work represented well the highest stress amplitudes in the mooring chain links. However, if the most damaging load level in service could be identified with higher confidence, the comparison could be improved.

6 Suggestions for further work

In the current section, some concrete ideas and comments for further studies are presented. The studies could not be completed in the current work due to time constraints.

6.1 Corrosion fatigue at mooring chain service loads

As pointed out, it is important to investigate which loads are more damaging for chains in service in order to determine relevant loads to use in future fatigue testing. In the load analysis for a semi-submersible platform in [31], the potentially most damaging loads were determined, assuming that even the lowest loads that a chain experiences in service can propagate fatigue cracks. However, if a cut-off limit exists, the most damaging load may be higher, since the lowest loads can be ignored. Identification of the cut-off limit thus remains one of the most important topics for accurate prediction of mooring chain lives.

The fatigue and cut-off limit could be investigated in small-scale fatigue test programs. Since offshore mooring chains are subjected to variable amplitude loading in service, it is useful to determine the cut-off limit. This can be calculated for a crack of a certain size from ΔK_{th} under realistic load frequencies in sea water. A potential test program could involve exposing specimens with fatigue cracks initiated at a higher load to realistic load conditions and environment for a long period of time. If a load level does not give any measurable crack growth increment, it can be considered to control ΔK_{th}.

For determining the fatigue limit, corroded surfaces from offshore mooring chains could be exposed to in-service load conditions and environment for several months. Testing at different, low load levels could reveal at which local stress amplitudes no initiation occurred.

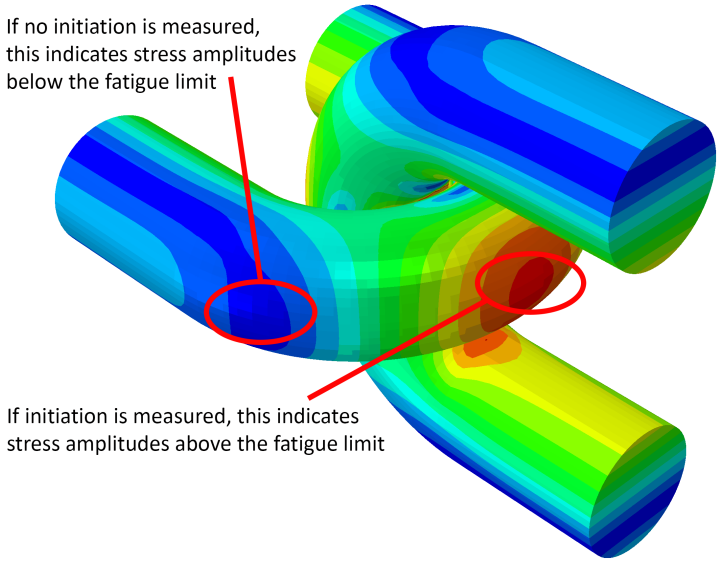

Figure 12: A hypothetical stress amplitude field in a chain link. Red areas show the highest stresses, and blue the lowest stresses. Some regions of high and low stresses are highlighted.

Alternatively, detailed FEA of selected, long-duration, full-scale tests could be performed. The heterogeneous surface stress distribution in a chain link under load could then be taken advantage of. A fatigue limit could possibly be deducted from careful non-destructive or destructive testing combined with stress analysis of regions of the chain links with different levels of stress. If no initiations are measured in a region, this could indicate that stresses are locally below the fatigue limit. Such a concept is illustrated in Fig. 12 for a hypothetical stress state in a chain link.

6.2 Mean stress effect on fatigue initiation from corroded surfaces

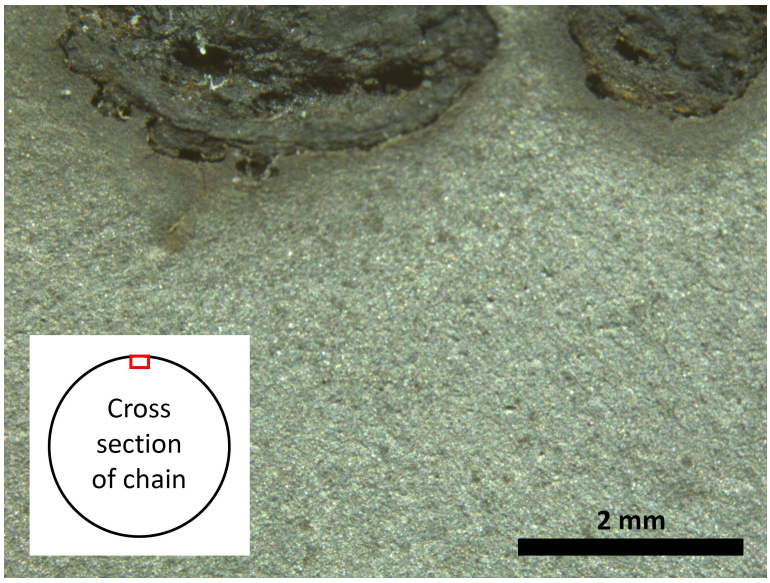

Figure 13: Section of fatigue fracture surface from another test program that shows an example of a corrosion pit on a mooring chain surface.

Some authors have identified a mean stress dependency on fatigue life in the full-scale tests[30, 42, 43]. It would be useful for understanding the fatigue behavior of chains in service if any mean stress dependency could be attributed to effects primarily on the crack initiation or on the crack growth stage. The current section outlines a study of mean stress effect on corroded surfaces.

Fig. 13 shows a small section of the fracture surface from a fatigue test in air performed outside of the current work on corroded R4-grade steel from a mooring chain link. Two corrosion pits with a highly irregular surface can be seen. In the left pit, tendencies to smaller pits within it can be seen, a constellation which has been demonstrated to increase the stress concentration factor[53].

One hypothesis could be that corrosion pits-in-pits or other critical corrosion geometries might yield sufficiently high local stress amplitudes to cause

transient mean stress relaxation, or even instant mean stress reduction from plastic overloads. If so, the effect of mean stresses on the fatigue initiation stage would be reduced.

To investigate the micro-scale mean stress evolution in corrosion pits, FEAs using the material models from Part 2 could be performed. Pit geometries could be obtained from micro-scale 3D scans, or 2D profiles extracted from micrographs could be used. Another alternative could be to model some idealized, worst-case pit geometries.

When local mean stresses had been calculated, fatigue initiation lives could be predicted. Eventually, fatigue tests with different mean stresses and the DIC crack detection procedure developed in Part 1 could be used to verify the predictions.

6.3 In-situ fatigue crack monitoring in offshore mooring chains

In-situ surface scanning of offshore mooring chains is time consuming and can only give information about the corrosion condition. When combined with FEA, it can provide the probability of crack fatigue initiation, but it cannot identify an existing crack. In-situ fatigue crack monitoring, on the other hand, would give valuable warnings about already cracked chain links that are nearing the end of their fatigue life. However, in-situ crack monitoring represents a practical challenge, and no applicable methods have been demonstrated. The current section presents an idea for a monitoring method.

Impulse excitation technique has been used to determine dynamic elastic material properties for specimens with specified geometries[54]. The method works by tapping on a specimen and measure the resonant frequencies. Perhaps a similar approach could be used for detecting cracks in a chain link with known elastic material properties, but an unknown state of cracking.

Crack growth in the outside of the crown of a chain link in tension is likely to cause a measurable stiffness change, because of the bending moment load in this location. FEA could be used for a sensitivity study of effect of crack sizes on resonant frequencies. However, alterations of the chain link geometry from corrosion and wear would also have to be accounted for.

6.4 Other thoughts

Corrosion fatigue of mooring chains involves mechanisms that are not well-understood and where fundamental research is still needed. Much of the current research is based on empirical observations. Empirical models are great for capturing trends in test data, but without a proper model of degradation mechanisms on the micro scale, it is difficult to predict what will happen outside of the ranges of a test program. Future research should be focused on multiphysics modeling, especially on interaction between mechanical and electrochemical phenomena during fatigue crack initiation and growth.

In the LifeMoor project, a large database of full-scale tests has been compiled. Even though some work on statistical processing of the test results has been carried out[34], there is still potential for more. Especially if combining with detailed stress analysis and material modeling, one could learn more about what affects fatigue of the chain segments.

Bibliography

[1] Mathisen J, Hørte T, Moe V, Lian W. DEEPMOOR – Design methods for deep water mooring systems – calibration of a fatigue limit state. DNV; 1999. DNV Technical Report No. 98-3110 R, rev. 3.

[2] Kvitrud A. Lessons learned from Norwegian mooring line failures 2010–2013. In: Proceedings of the ASME 2014 33rd International Conference on Ocean, Offshore and Arctic Engineering. ASME; 2014. https://doi.org/10.1115/OMAE2014-23095.

[3] Offshore standards, DNV-OS-E301, Position mooring. DNV AS; 2021.

[4] Dowling NE. Mechanical Behavior of Materials: Engineering Methods for Deformation, Fracture, and Fatigue. 3rd ed. Upper Saddle River, NJ, USA: Pearson Prentice Hall; 2007.

[5] Schijve J. Fatigue of Structures and Materials. 2nd ed. Springer Netherlands; 2009. https://doi.org/10.1007/978-1-4020-6808-9.

[6] Basquin OH. The exponential law of endurance tests. American Society for Testing and Materials Proceedings. 1910;10:625–630.

[7] Wormsen A, Sjödin B, Härkegård G, Fjeldstad A. Non-local stress approach for fatigue assessment based on weakest-link theory and statistics of extremes. Fatigue Fract Eng Mater Struct. 2007;30(12):1214 1227. https://doi.org/10.1111/j.1460-2695.2007.01190.x.

[8] Pollak RD, Palazotto AN. A comparison of maximum likelihood models for fatigue strength characterization in materials exhibiting a fatigue limit. Probabilistic Eng Mech. 2009;24(2):236 241. https://doi.org/10.1016/j.probengmech.2008.06.006.

[9] Smith JO. The effect of range of stress on the fatigue strength of metals. University of Illinois Engineering Experiment Station Bulletin Series No 334. 1942;39(25).

[10] Graham JA, Millan JF, Appl FJ, editors. Fatigue Design Handbook. Society of Automotive Engineers; 1968.

[11] Gerber H. Bestimmung der zulässigen Spannungen in Eisen-Constructionen. Z Bayer Arch Ing Ver. 1874;6:101-10.

[12] Walker K. The effect of stress ratio during crack propagation and fatigue for 2024-T3 and 7075-T6 aluminum; 1970. ASTM STP32032S, https://doi.org/10.1520/STP32032S.

[13] Smith KN, Topper T, Watson P. A stress–strain function for the fatigue of metals. J Mater. 1970;5:767-78.

[14] Bruun ØA, Härkegård G. A comparative study of design code criteria for prediction of the fatigue limit under in-phase and out-of-phase tension–torsion cycles. Int J Fatigue. 2015;73:1-16. https://doi.org/10.1016/j.ijfatigue.2014.10.015.

[15] Härkegård G, Halleraker G. Assessment of methods for prediction of notch and size effects at the fatigue limit based on test data by Böhm and Magin.

Int J Fatigue. 2010;32(10):1701-9. https://doi.org/10.1016/j.ijfatigue.2010.03.011.
[16] Taylor D, Bologna P, Bel Knani K. Prediction of fatigue failure location on a component using a critical distance method. Int J Fatigue. 2000;22(9):735-42. https://doi.org/10.1016/S0142-1123(00)00062-1.
[17] Coffin LF Jr. A study of the effects of cyclic thermal stresses on a ductile metal. Trans ASME. 1954;76:931-50.
[18] Manson SS. Behavior of Materials under Conditions of Thermal Stress. National Advisory Committee of Aeronautics; 1953. NACA-TN-2933.
[19] James MR. Relaxation of residual atresses – an overview. In: Niku-Lari A, editor. Residual Stresses. Pergamon; 1987. p. 349-65. https://doi.org/10.1016/B978-0-08-034062-3.50026-4.
[20] Miner MA. Cumulative damage in fatigue. J Appl Mech. 2021 03;12(3):A159-64. https://doi.org/10.1115/1.4009458.
[21] Paris P, Erdogan F. A critical analysis of crack propagation laws. J Basic Eng. 1963 12;85(4):528-33. https://doi.org/10.1115/1.3656900. Available from: https://doi.org/10.1115/1.3656900.
[22] Gangloff RP. Corrosion fatigue crack propagation in metals. In: 1st International Conference on Environment Induced Cracking of Metals. NASA; 1990. https://ntrs.nasa.gov/citations/19900015089.
[23] Shipilov SA. Mechanisms for corrosion fatigue crack propagation. Fatigue Fract Eng Mater Struct. 2002;25(3):243-59. https://doi.org/10.1046/j.1460-2695.2002.00447.x.
[24] Montgomery EL, Calle LM, Curran JC, Kolody MR. Timescale correlation between marine atmospheric exposure and accelerated corrosion testing – part 2. In: Corrosion 2012. NACE; 2012. NACE-2012-1730, https://onepetro.org/NACECORR/proceedings/CORR12/All-CORR12/NACE-2012-1730/120250.
[25] Baldwin KR, Smith CJE. Accelerated corrosion tests for aerospace materials: current limitations and future trend. Aircr Eng Aerosp Technol. 1999;71(3):239 244. https://doi.org/10.1108/00022669910270718.
[26] Gabrielsen Ø, Liengen T, Molid S. Microbiologically influenced corrosion on seabed chain in the North Sea. In: Proceedings of the ASME 2018 37th International Conference on Ocean, Offshore and Arctic Engineering. ASME; 2018. https://doi.org/10.1115/OMAE2018-77460.
[27] Offshore standards, DNV-OS-E302, Offshore mooring chain. DNV AS; 2021.
[28] Zarandi EP, Skallerud BH. Experimental and numerical study of mooring chain residual stresses and implications for fatigue life. Int J Fatigue. 2020;135:105530. https://doi.org/10.1016/j.ijfatigue.2020.105530.
[29] Martinez Perez I, Constantinescu A, Bastid P, Zhang YH, Venugopal V. Computational fatigue assessment of mooring chains under tension loading. Eng Fail Anal. 2019;106:104043. https://doi.org/10.1016/j.engfailanal.2019.06.073.

[30] Lone EN, Leira BJ, Sauder T, Aksnes V, Gabrielsen Ø, Larsen K. Influence of mean tension on mooring line fatigue life. vol. Volume 2A: Structures, Safety, and Reliability of International Conference on Offshore Mechanics and Arctic Engineering. ASME; 2020. https://doi.org/10.1115/OMAE2020-18628.

[31] Lone EN, Sauder T, Larsen K, Leira BJ. Probabilistic fatigue model for design and life extension of mooring chains, including mean load and corrosion effects. Ocean Eng. 2022;245:110396. https://doi.org/10.1016/j.oceaneng.2021.110396.

[32] Bauer E. Interannual changes of the ocean wave variability in the North Atlantic and in the North Sea. Clim Res. 2001;18(1-2):63-9. https://doi.org/10.3354/cr018063.

[33] Ma K, Gabrielsen Ø, Li Z, Baker D, Yao A, Vargas P, et al. Fatigue tests on corroded mooring chains retrieved from various fields in offshore West Africa and the North Sea. In: Proceedings of the ASME 2019 38th International Conference on Ocean, Offshore and Arctic Engineering. vol. 3. ASME; 2019. https://doi.org/10.1115/OMAE2019-95618.

[34] Mendoza J, Haagensen PJ, Köhler J. Analysis of fatigue test data of retrieved mooring chain links subject to pitting corrosion. Mar Struct. 2022;81:103119. https://doi.org/10.1016/j.marstruc.2021.103119.

[35] Lone EN, Sauder T, Larsen K, Leira BJ. Fatigue assessment of mooring chain considering the effects of mean load and corrosion. vol. Volume 2: Structures, Safety, and Reliability of International Conference on Offshore Mechanics and Arctic Engineering; 2021. https://doi.org/10.1115/OMAE2021-62775.

[36] Fredheim S, Reinholdtsen SA, Håskoll L, Lie HB. Corrosion fatigue testing of used, studless, offshore mooring chain. In: Proceedings of the ASME 2013 32nd International Conference on Ocean, Offshore and Arctic Engineering. ASME; 2013. OMAE2013-10609.

[37] Gabrielsen Ø, Liengen T, Rørvik G, Molid S, Stavang T. Corrosion experience with low carbon steel R4 grade mooring chain. vol. Day 3 Wed, August 18, 2021 of OTC Offshore Technology Conference; 2021. https://doi.org/10.4043/31233-MS.

[38] Zarandi EP, Skallerud BH. Cyclic behavior and strain energy-based fatigue damage analysis of mooring chains high strength steel. Mar Struct. 2020;70:102703. https://doi.org/10.1016/j.marstruc.2019.102703.

[39] Arredondo A, Fernández J, Silveira E, Arana JL. Corrosion fatigue behavior of mooring chain Steel in seawater. vol. Volume 1: Offshore Technology; Offshore Geotechnics of International Conference on Offshore Mechanics and Arctic Engineering; 2016. https://doi.org/10.1115/OMAE2016-54426.

[40] Lassen T, Storvoll E, Bech A. Fatigue life prediction of mooring chains subjected to tension and out of plane bending. vol. Volume 1: Offshore Technology of International Conference on Offshore Mechanics and Arctic Engineering. ASME; 2009. p. 229-39. https://doi.org/10.1115/OMAE2009-79253.

[41] Canut FA, Simões AMP, Reis L, Freitas M, Bastos IN, Castro FC, et al. Monitoring of corrosion-fatigue degradation of grade R4 steel using an electrochemical-mechanical combined approach. Fatigue Fract Eng Mater Struct. 2019;42(11):2509-19. https://doi.org/10.1111/ffe.13079.

[42] Gabrielsen Ø, Larsen K, Dalane O, Lie HB, Reinholdtsen S. Mean load impact on mooring chain fatigue capacity: Lessons learned from full scale fatigue testing of used chains. In: Proceedings of the ASME 2019 38th International Conference on Ocean, Offshore and Arctic Engineering. vol. 3. ASME; 2019. https://doi.org/10.1115/OMAE2019-95083.

[43] Influence of the mean load on the fatigue performance of mooring chains. vol. Day 1 Mon, May 06, 2019 of OTC Offshore Technology Conference; 2019. D011S014R002, https://doi.org/10.4043/29621-MS.

[44] Fernández J, Storesund W, Navas J. Fatigue performance of grade R4 and R5 mooring chains in seawater. In: Proceedings of the ASME 2014 33rd International Conference on Ocean, Offshore and Arctic Engineering. ASME; 2014. https://doi.org/10.1115/OMAE2014-23491.

[45] Jones EMC, Iadicola MAE. A Good Practices Guide for Digital Image Correlation; 2018. https://doi.org/10.32720/idics/gpg.ed1.

[46] Rampi L, Dewi F, Francois M, Gerthoffert A, Vargas P. Chain out of plane bending (OPB) fatigue joint industry project (JIP) static test program and OPB interlink stiffness. vol. Volume 1: Offshore Technology; Offshore Geotechnics of International Conference on Offshore Mechanics and Arctic Engineering; 2016. V001T01A052, https://doi.org/10.1115/OMAE2016-54195.

[47] Evans C, Leiva-Garcia R, Akid R. Strain evolution around corrosion pits under fatigue loading. Theor Appl Fract Mech. 2018;95:253-60. https://doi.org/10.1016/j.tafmec.2018.02.015.

[48] Lassen T, Arana JL, Canada L, Henriksen J, Holthe NK. Crack growth in high strength chain steel subjected to fatigue loading in a corrosive environment. vol. 3 of International Conference on Offshore Mechanics and Arctic Engineering; 2005. p. 93-101. https://doi.org/10.1115/OMAE2005-67242.

[49] Zarandi EP, Skallerud BH. Experimental and numerical study of mooring chain residual stresses and implications for fatigue life. Int J Fatigue. 2020;135:105530. https://doi.org/10.1016/j.ijfatigue.2020.105530.

[50] Yamamoto N, Sugimoto T, Ishibashi K. Fatigue strength assessment of a structure considering corrosion wastage and corrosion fatigue. In: Proceedings of the ASME 2018 37th International Conference on Ocean, Offshore and Arctic Engineering. vol. 3. ASME; 2018. https://doi.org/10.1115/OMAE2018-78188.

[51] Aursand M, Skallerud BH. Numerical simulation of fatigue crack growth in offshore mooring chains. MekIT'19: 10th National Conference on Computational Mechanics. NTNU; 2019. p. 61-80.

[52] Aursand M, Skallerud BH. Mode I stress intensity factors for semi-elliptical fatigue cracks in curved round bars. Theor Appl Fract Mech. 2021;112:102904. https://doi.org/10.1016/j.tafmec.2021.102904.
[53] Cerit M, Genel K, Eksi S. Numerical investigation on stress concentration of corrosion pit. Eng Fail Anal. 2009;16(7):2467-72. https://doi.org/10.1016/j.engfailanal.2009.04.004.
[54] ASTM E1876-21. Standard test method for dynamic Young's modulus, shear modulus, and Poisson's ratio by impulse excitation of vibration. ASTM; 2021. https://doi.org/10.1520/E1876-21.

Appended articles

International Journal of Fatigue 151 (2021) 106350

Contents lists available at ScienceDirect

International Journal of Fatigue

journal homepage: www.elsevier.com/locate/ijfatigue

Digital image correlation for continuous mapping of fatigue crack initiation sites on corroded surface from offshore mooring chain

Paul Qvale [a,*], Ershad P. Zarandi [a], Sigmund K. Ås [b], Bjørn H. Skallerud [a]

[a] Department of Structural Engineering, Norwegian University of Science and Technology (NTNU), NO-7491 Trondheim, Norway
[b] Department of Marine Technology, NTNU, NO-7491 Trondheim, Norway

ARTICLE INFO

Keywords:
Fatigue initiation
Digital image correlation
Finite elements
Corrosion fatigue
Offshore engineering

ABSTRACT

The full-field digital image correlation (DIC) technique was used to identify crack initiation and early crack growth on irregular, corroded surfaces from offshore mooring chain. Finite element analysis was paired with the DIC measurements, which made it possible to correlate initiation events with local stress concentrations due to corrosion pits. An initiation S-N curve was established based on this correlation. It included 14 crack initiation events from 4 specimens, in addition to statistical treatment of regions where no initiation occurred. The first cracks initiated at 13–24% of the total lifetimes of the specimens.

1. Introduction

Mooring chains are an integral part of floating structures for offshore energy production. In service, they have a limited lifetime, and corrosion fatigue is an important degradation mechanism. General corrosion reduces the cross section areas, and pitting corrosion raises the cyclic stress ranges locally[1,2]. Replacing the mooring chains on a production unit represents a significant cost for the operator. Thus, the industry needs more accurate lifetime estimates, allowing for more timely replacement of the chains. This could improve safety and reduce costs and environmental impact.

A number of chain segments have been fatigue tested in artificial sea water during the past decades[3,4]. Although full-scale corrosion fatigue tests give valuable benchmark data, it is still a challenge to use these results for in-service lifetime prediction. In order for the tests to finish within a reasonable time, the applied cyclic loads and load frequencies have been higher than those experienced by the chains in service. Since corrosion is a time dependent process, effects of the corrosive environment on fatigue is decreased when tests are accelerated. Considering this effect alone, full-scale laboratory data would give non-conservative predictions when applied to in-service chains. Test temperature also affects free corrosion crack growth, and in this case the laboratory tests conducted at room temperature would be detrimental to fatigue life, i.e. conservative compared to the in-service temperatures experienced during the winter months in the North and Norwegian Sea [5]. There are several other uncertainties that exacerbate this fundamental problem of using corrosion fatigue lab data in the real world, such as the use of constant amplitude data for in-service spectrum loading, choice of damage accumulation methods, mean stress corrections, and others[6–8]. The various approaches to account for these effects in lifetime prediction typically distinguish between initiation mechanisms and crack growth mechanisms. Detailed studies have been made on the initiation of cracks from pits[9–15] that have provided valuable insights into growth of small cracks from corrosion pits. Whereas these efforts were aimed at single artificially created pits, the current study is aimed at detecting initiation events within a larger area of corroded surfaces, either on full-scale chain links or on small-scale specimens.

Digital image correlation (DIC) is a full-field, optical monitoring technique that can be used to track displacements on a surface from a series of sequentially captured images[16]. The method has been used to gain valuable insight into fatigue crack behavior on a macro (continuum) scale [17,18] and micro scale [19]. Crack initiation from the mouth of an artificial corrosion pit in a smooth specimen has been monitored[10], and in a fatigue test a specimen with an electropolished surface, multiple microcrack initiation sites were revealed using DIC [20]. To the authors' knowledge, there has been no attempt to monitor fatigue crack initiation on a surface with general corrosion from service, like that of an offshore mooring chain.

The motivation for the current work is to promote detection of crack initiation in both small-scale and full-scale testing. Initiation life in this paper is defined, using the recorded surface displacements, as the

* Corresponding author.
E-mail address: paul.qvale@ntnu.no (P. Qvale).

https://doi.org/10.1016/j.ijfatigue.2021.106350
Received 29 March 2021; Received in revised form 12 May 2021; Accepted 24 May 2021
Available online 28 May 2021
0142-1123/© 2021 The Author(s). Published by Elsevier Ltd. This is an open access article under the CC BY license (http://creativecommons.org/licenses/by/4.0/).

number of cycles until a crack of a certain size can be detected. An initiation event is thus not related to the micromechanical process of forming a crack from persistent slip bands[6]. Rectangular bar specimens were extracted from mooring chain links retrieved from service, while keeping one face as-corroded. The specimens were subjected to cyclic loading in a three-point bending test setup in an air environment. DIC was used to measure displacement histories for a grid of points on the corroded surface. Early signs of crack initiation across the corroded specimen surface were captured by applying an initiation criterion to the displacement histories of the points in the grid, to determine the fatigue lifetime spent on initiation and growth, respectively. Finite element analysis (FEA) was performed on scanned specimen geometries to calculate the stresses at initiation sites. The database of initiation events was used to establish an initiation *S-N* curve for a surface element of a corroded mooring chain link.

2. Methodology

2.1. Experimental details

2.1.1. Specimen preparation

Four fatigue test specimens were cut from the non-welded straight section of two connected Ø114 mm mooring chain links, see Fig. 1. The links were made from R4 grade high-strength steel. Monotonic and cyclic yield strengths of 843 MPa and 630 MPa, respectively, have been measured on similar links[21]. The links had been retrieved from chains that had been in service on a floating production storage and offloading (FPSO) unit in the Norwegian Sea for 15 years. The two links had been exposed to identical service loads and environment. The specimens were cut from the chain links using electrical discharge machining (EDM), and then milled to their final dimensions, as shown in Fig. 2. The coordinate system in the figure will be used as a reference throughout this work. It can be assumed that residual stresses from production of the chains[22,23] were relieved from the specimen material when the specimens were extracted.

To remove corrosion products and expose the bare metal surface for optical fatigue monitoring, the corroded specimens were degreased and cleaned in a hydrochloric acid solution according to ASTM G1 - 03 (2017) e1, procedure C.3.5[24]. Degreasing and cleaning was done in an ultrasonic acetone bath. Thereafter, the specimens were lightly brushed to remove remaining corrosion products. After the treatment, some

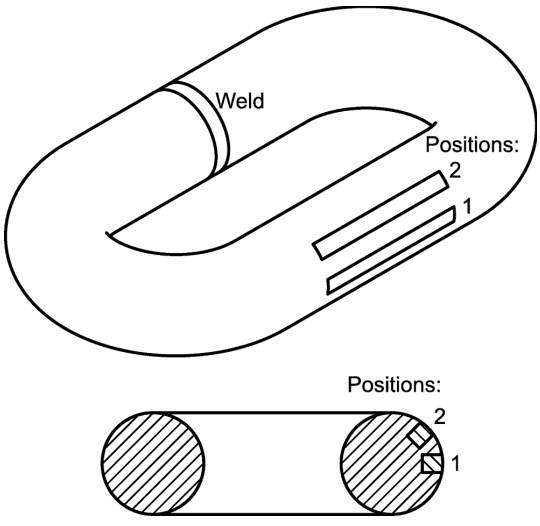

Fig. 1. Extraction locations of specimens in a chain link.

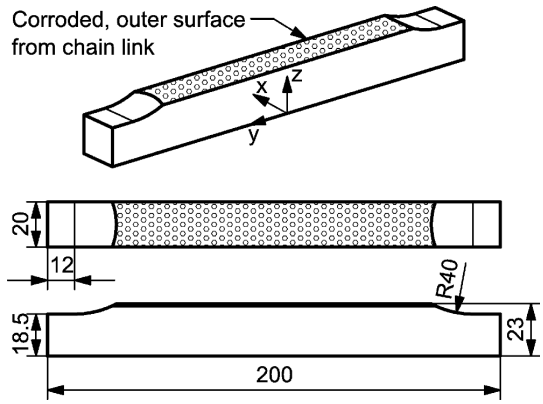

Fig. 2. Dimensions of specimens in millimeters. Reference coordinate system is shown.

corrosion products still remained in the deepest pits. However, since the metal surface everywhere else on the corroded surfaces had been successfully exposed, the result was considered satisfactory. Ideally, no corrosion product should have been left on the specimens. Nevertheless, more aggressive cleaning procedures were not attempted, to avoid risk of damaging the surfaces. Fig. 3 shows the corroded surfaces of the specimens after cleaning.

2.1.2. Fatigue test setup

The specimens were loaded cyclically in a three-point bending setup as shown in Fig. 4. The specimens had been extracted from the straight part of chain links, to provide a corroded surface with a convenient shape for fatigue testing. However, the moment load induced by a three-point bending setup resembles more closely that found in the crown of a loaded chain link, where the majority of failures in recent full-scale tests have been found to occur[25]. The load levels that were used are shown in Table 1. The loads correspond to a nominal stress ratio (of minimum to maximum stress) of $R = 0.2$. The loads were applied using a triangular wave shape and a frequency of 3 Hz. Loading was applied using an Instron 8800 250 kN test system and an A10025E cylinder with a stroke of 250 mm. An Instron 250 kN load cell was used. Load cell calibration performed 2 years before testing was executed showed 0.2% deviation at 25 kN tension load.

2.1.3. Monitoring by DIC

A random, monochrome surface pattern was needed to provide surface references for the DIC monitoring. The corroded surfaces of the specimens were sprayed with a thin coat of white paint. Thereafter, a light dust of black paint was applied, leaving the specimens with a fine speckle pattern.

For acquiring images, one 12.3-megapixel Basler acA4112-30um camera with a Sony IMX304 CMOS sensor and a Samyang 100 mm f/2.8 ED UMC Macro lens was mounted on each side of the testing rig in a manner shown for one side in Fig. 5. A two-camera setup was used, to be able to capture displacements on different sides of surface features, and to allow for 3D post-processing of DIC images. Nevertheless, the algorithms developed in this work only made use of 2D displacements. Since a beam in the testing rig prevented the placement of a camera directly below the surface, the cameras had to be placed at a 48°angle to the surface normal. This setup allowed for sufficient depth of field to obtain images that covered the width of a specimen. The photographed mid-sections had lengths of 40–42 mm. The image resolution was 3000 pixels (px) in the *y* direction. A Metz Mecalight LED-480 LED panel was placed 85 mm below the specimen surface to keep the shutter times low. The cameras were triggered at the peak load of every 100th load cycle.

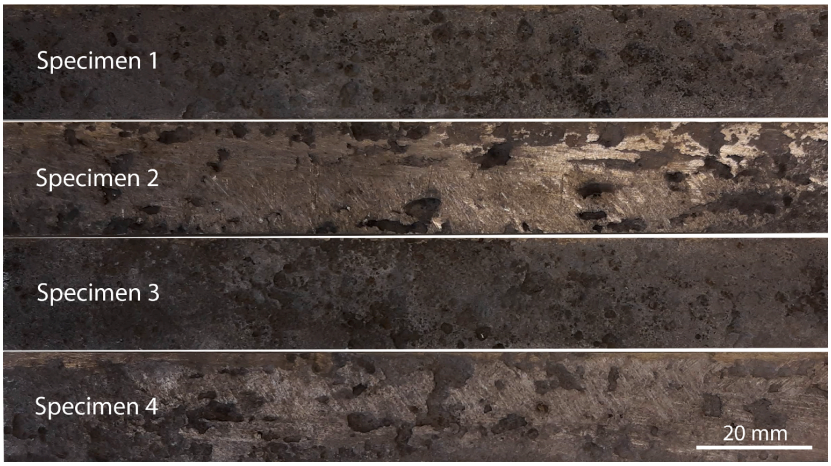

Fig. 3. Cleaned corroded surfaces of the specimens.

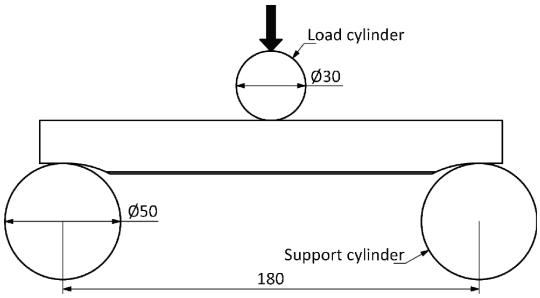

Fig. 4. Three-point bending setup used for fatigue testing.

Camera shutter times were 15–20 ms.

Post-processing of images was carried out in the in-house, finite-element based DIC code eCorr v4.0[26]. A mesh consisting of 15-by-15 px, isoparametric Q4 bilinear quadrilateral elements was created to track the coordinate evolutions on the relevant surface. This corresponds to an element length of 0.2 mm in the y direction and 0.3 mm in x direction of the specimen. Each element had four corner nodes, and consequently, each node was shared between four elements.

In the current work, crack initiation on the surfaces of the fatigue test specimens was detected by imposing a criterion on sub-pixel, inter-node displacement of the DIC mesh as load cycling progressed. The nodal coordinate histories were imported to the numeric computing environment MATLAB, and the following criterion was implemented on the nodal displacements in the y direction of the specimens:

The distance between a node and its neighbor is thought of as a material ligament. A ligament is considered broken, and thus, a crack is defined as initiated, when the ligament length has increased by 0.15 px (2 μm) above its all-time minimum.

Fig. 6 illustrates the criterion. Fig. 7 provides an example of an inter-node displacement history and application of the criterion. To avoid false indications of initiation caused by noise in the DIC measurements, a ten-point moving average of the displacement histories were used. As an additional measure against temporary fluctuations in ligament length, only ligaments eventually reaching 0.90 px (13 μm) of extension were considered real initiation points. The last intersection of the displacement curve with the 0.15 px limit was defined as the initiation time. As will be shown, the criterion produced realistic initiation events and subsequent crack growth with few erroneous indications.

Tilting of the cameras relative to the specimens introduced a small error in the DIC measurements. Since the camera sensor was parallel with the specimen y axis, the error along this axis due to perspective distortion could be readily estimated. With the current camera setup, the distance from the center of the lenses to the specimen surfaces was around 520 mm. Geometric calculations showed that measurements of a displacement in the y direction on the edges of the specimen could differ by $\pm$1.3% compared to measurements made in the x-z midplane. This error was considered negligible for the purpose of using the crack initiation detection criterion.

It should be noted that a more pronounced error can occur regardless of camera angle when cracks start to grow large in a specimen in a bending fatigue setup. As the bending stiffness is reduced, the deflection at maximum load along the loading axis increases cycle by cycle. In relation to the camera sensor, this results in an out-of-plane displacement, which eventually causes a significant error in the inter-node displacement measurements. For reasons described later, the DIC processing in the current work was limited to detection of cracks as long as they remained relatively small. In this domain, the recorded deflection at maximum load at the position of the load roller did not increase more than 0.14 mm for any specimen. Calculations for the current camera angle showed that this resulted in a maximum error of only 2.0% on displacements measured with DIC, which was deemed negligible.

Table 1
Load levels for each specimen and original positions on the chain links. The highest nominal stresses in y direction at the surface of a specimen are also given.

Specimen ID	Link ID	Position on link	Load amplitude/kN	Mean load/kN	Nominal stress amplitude/MPa	Nominal mean stress/MPa
1	1	1	8	12	211	317
2	1	2	10	15	263	395
3	2	1	8	12	211	317
4	2	2	10	15	263	395

Fig. 5. One side of test rig with camera.

2.2. Surface scanning and FEA

For the purpose of stress calculations by FEA, all specimens were surface scanned using a GOM ATOS 5 8MP scanner with a MV170 lens pair, with a measurement volume of 170x130x130 mm. The system is based on fringe projection [27] and optical triangulation for relative positioning of multiple scans. The specimens were placed on a software controlled rotary table, thus multiple scans from different angles could be collected automatically to cover all sides of the surface pits. The size probing error and sphere spacing error have been found to be 6 μm and -4 μm, respectively, according to VDI/VDE 2634–3:2008 test procedures. GOM Inspect 2019 software was used for processing the scans, using the "high detail" setting to retain as much detail from the point cloud as possible. Autofill was applied in GOM Inspect to close holes that appeared in a few deeply recessed or dark areas. Finally, the mesh was smoothed with a surface tolerance of 0.01 mm in order to remove smaller asperities. The resulting surface meshes were regularized in the modelling software ANSYS SpaceClaim by applying its "shrinkwrap" feature. A 0.15 mm element size was used on the surface of the midsection of the specimens. In the FEA software ANSYS Mechanical, solid, quadratic-order tetrahedron meshes were generated, applying a slow transition from the midsection element size to a global element size of 1.5 mm. An example of a meshed specimen is shown in Fig. 8.

A mesh sensitivity analysis was carried out for the midsection element size. For a semi-spherical Ø2 mm pit in the middle of an otherwise smooth specimen surface, 0.15 mm and 0.22 mm size elements provided nearly identical results for stresses in the *y* direction. A mesh consisting of 0.35 mm elements gave slightly deviating results. Thus, it can be concluded that both a 0.15 mm and 0.22 mm element mesh are of adequate resolution for accurate stress calculation for a pitted surface.

For FEA of the specimens, loading was applied as concentrated line loads and displacements at the position of the rollers in the testing rig. As will be seen, stress amplitudes remained below the cyclic yield strength across all specimen surfaces. Thus, a monotonic material model for R4

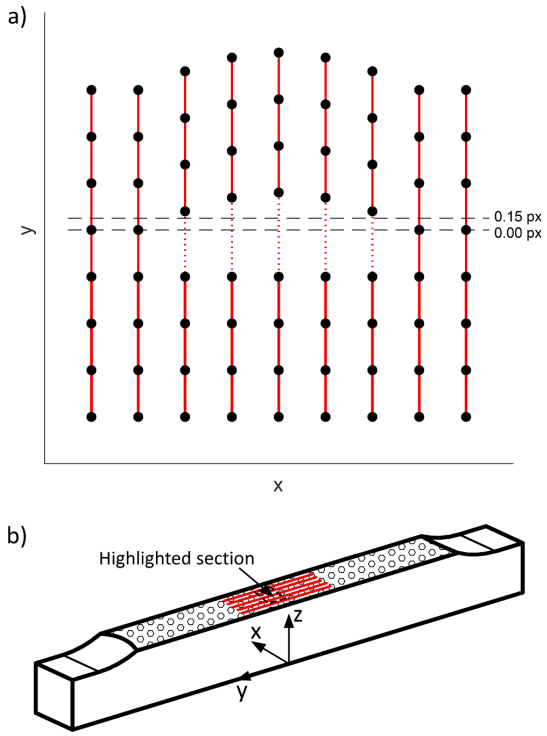

Fig. 6. Schematic illustration of a) crack initiation criterion on DIC results on b) the midsection of a specimen. The black dots in a) represent DIC mesh nodes. Surface material ligament (red) was considered broken if inter-node displacement exceeded 0.15 px, corresponding to a displacement of 2 μm.

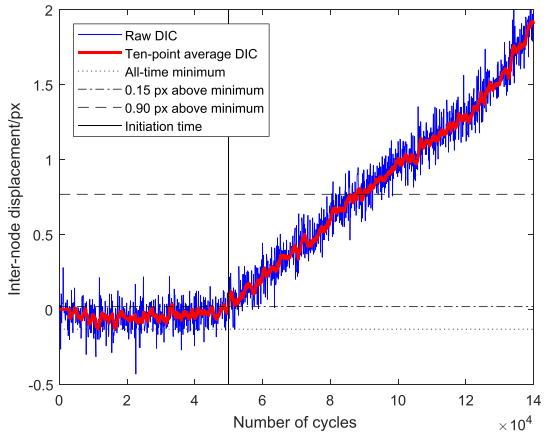

Fig. 7. Crack initiation detection criterion applied on a node pair in *y* direction. Initiation was said to happen at the last time the displacement curve crossed the line for 0.15 px above the all-time minimum, corresponding to a displacement of 2 μm.

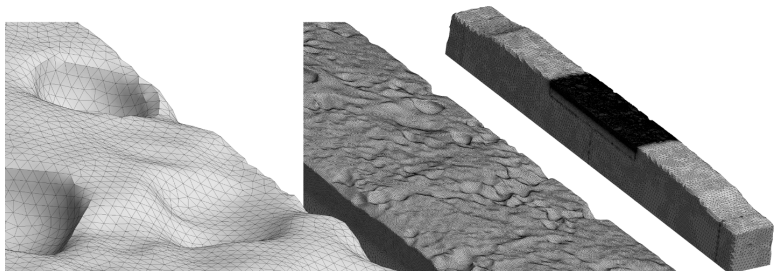

Fig. 8. Different zooms on the finite element surface mesh used for the midsection of specimen 3.

grade steel from [21] was used. Stress amplitudes in the y direction of the specimens, S_{ya}, were exported and used for the fatigue analysis.

2.3. Censoring data for multiple initiation events

On a corroded surface, corrosion pits and other stress irregularities act as stress raisers that are often highly local. Since a crack growing from a pit into a sharply decreasing stress field may need time to develop, time is left for secondary cracks to initiate from other areas with less severe stress states. Since the DIC technique can detect initiation and growth of secondary cracks, this can provide statistical insights when coupled with the stress results from FEA. Since the surface stresses will be altered in a region surrounding the growing cracks, the initiation events should be censored if they are significantly influenced by neighboring cracks.

A "stress sensitivity analysis" from a growing crack was performed, to see how the stress field compared to that of a crack-free specimen. As a worst-case example, a quarter-circular corner crack was placed in the x-z plane of a specimen with smooth surfaces loaded in three-point bending, see Fig. 9. Fig. 10 shows how S_y change at distances from the center of the crack. As an example, the presence of a 1-mm crack is marked by dotted lines. They show that at distances greater than 1.9 and 3.6 mm from the crack center, S_y on path x and y, respectively, was less than 5% affected by the crack.

Based on the results in Fig. 10, an algorithm for classifying crack initiation events as "independent" was implemented in MATLAB: The crack development log from DIC was replayed cycle by cycle. The first

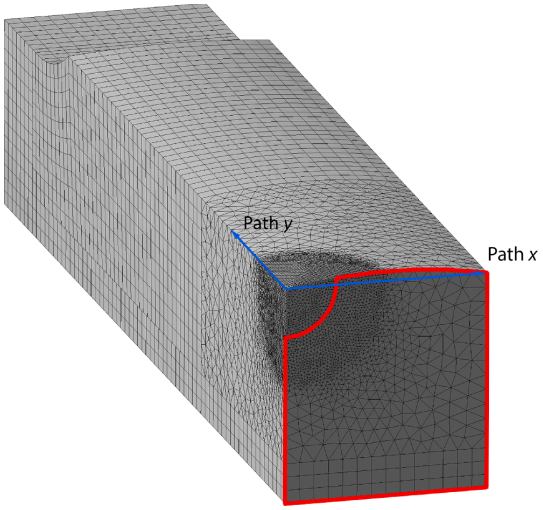

Fig. 9. FEA model for stress field sensitivity analysis for cracks of different sizes. The region enclosed in red is fixed in y direction at the x-z plane. Paths x and y are marked for outputting stresses.

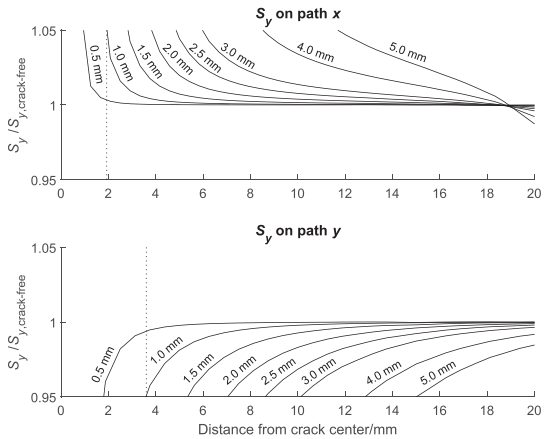

Fig. 10. S_y in a corner-cracked specimen with crack lengths 0.5 to 5 mm compared to a crack-free specimen. Stresses on paths x and y from Fig. 9 are shown. The dotted lines mark the distance from the crack center where a 1 mm crack causes 5% change in the stress field.

initiation was identified as stated earlier. As load cycling progressed, and further growth of the crack was registered by DIC, a 5% change in stress around the crack was said to invalidate the original FEA stress result. Only subsequent initiations *outside* of the region affected by the crack stresses were registered as new, independent initiations. As more cracks initiated, more regions of FEA stress were invalidated.

These conditions were enforced by virtually lining up rectangular areas around initiation sites, as cracks grew from them, and censoring any initiations happening within the rectangles. The rectangle sides had half lengths corresponding to crossings of the 5% lines in Fig. 10. Since Fig. 10 is based on a worst-case crack, this was thought to be a conservative approach. When the surface length of any crack in a specimen exceeded 3 mm, the effect on the original FEA stress field of a specimen was considered so extensive that the remaining stress field was invalidated.

2.4. Statistical treatment of results

The described algorithm returns data on initiation events on a specimen; however, it could also map regions that had survived without crack initiation at a given time. These data can be taken into account in the statistical treatment of the results. In the current work, the FEA stress amplitude fields for the midsection of each specimen were discretized into 0.1-by-0.1 mm, homogeneously stressed surface elements. Since it was known which elements experienced crack initiation and which did not, the best S-N curve fit to the data could be found using maximum likelihood regression. That is, an S-N curve was fitted to a few initiation events per specimen, as well as to the survival of every other 0.1-by-0.1

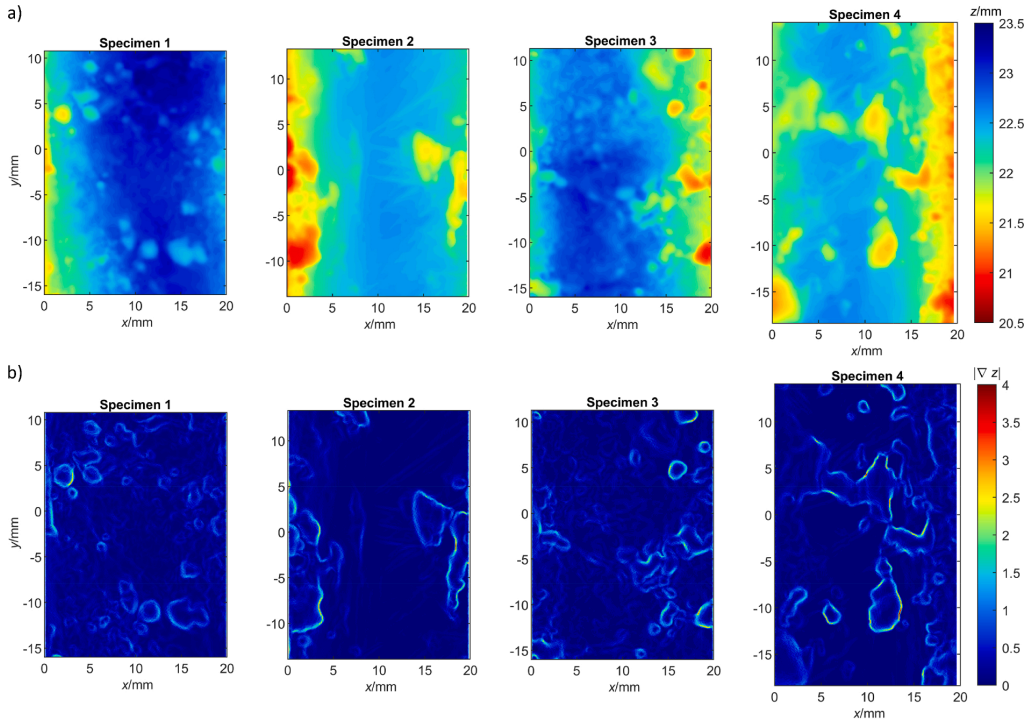

Fig. 11. a) Height profile and b) gradient plots of the midsection from every specimen.

mm surface element.

The curve fit was done by maximizing the *log-likelihood* function[28],

$$\mathscr{L} = \sum_{i=1}^{k} [\delta_i \log p_i + (1 - \delta_i) \log P_s] \tag{1}$$

for all k surface elements. Here, δ is an indicator function, which takes the value 1 if there is crack initiation in an element, and 0 if there is not. If the initiation lifetime is assumed to be Weibull distributed, then the probability density function for initiation, p_i, and the cumulative distribution function for survival, P_s, of a surface element, is given by[29]

$$\begin{aligned} p_i &= \frac{\ln 2 \cdot \beta_N \left(\frac{n}{N}\right)^{\beta_N}}{n \cdot 2^{\left(\frac{n}{N}\right)^{\beta_N}}} \text{ and} \\ P_s &= 2^{-\left(\frac{n}{N}\right)^{\beta_N}}, \end{aligned} \tag{2}$$

where β_N is the Weibull shape parameter, a measure of initiation lifetime scatter. n is the number of cycles recorded for the surface element, and N is the median initiation lifetime, given by the *S-N* curve[6],

$$N = A S_{ya}^{b}, \tag{3}$$

where S_{ya} is the stress amplitude in the y direction. A and b are fitting constants, and $1/b$ states the slope of the *S-N* curve in a diagram with logarithmic axes.

3. Results

Height profile and gradient plots calculated from surface scans of the specimen midsections are shown in Fig. 11. Because of a limit in the maximum allowable number of nodes in the DIC software, only 27–32 mm length segments containing the biggest pits around the middle of the specimens were analyzed. The plots in Fig. 11 have been cropped to show only these areas. It can be seen from the height profiles that, because of the irregular nature of the corroded chain surface, the actual

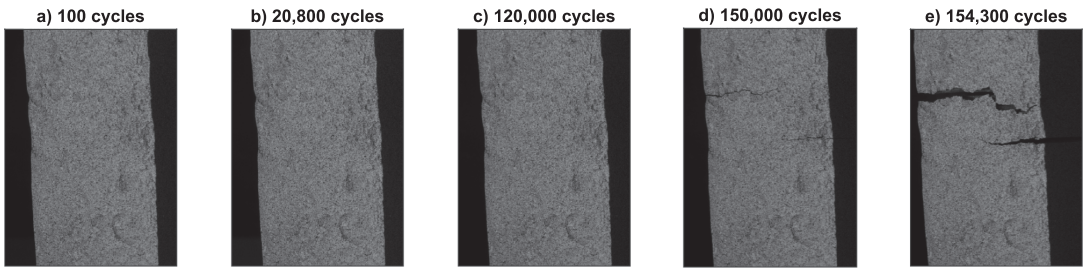

Fig. 12. Photographs of specimen 1 taken by the right camera a) at first frame, b) at 13%, c) 78% and d) 97% of the specimen lifetime and e) at the last frame before final fracture.

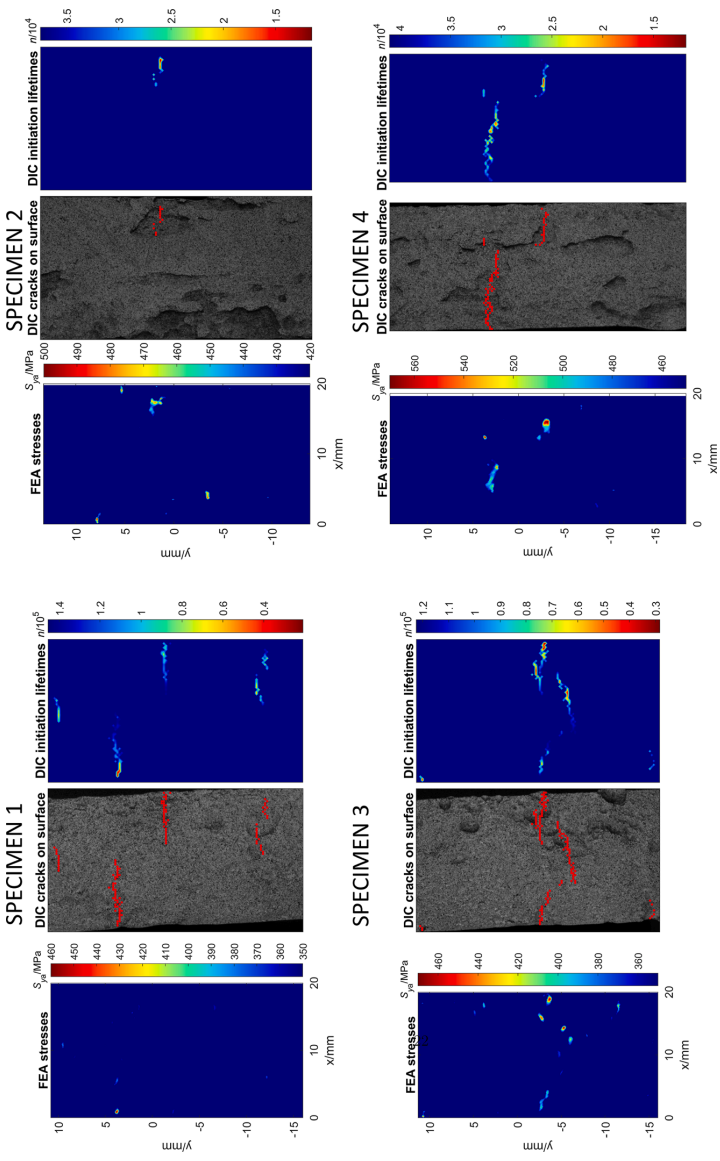

Fig. 13. Maps of stress amplitudes calculated with FEA (left) and crack initiation lifetimes measured with the crack initiation criterion on DIC results (right) for every specimen. The middle maps show crack development from DIC plotted on raw photographs of the specimen surfaces.

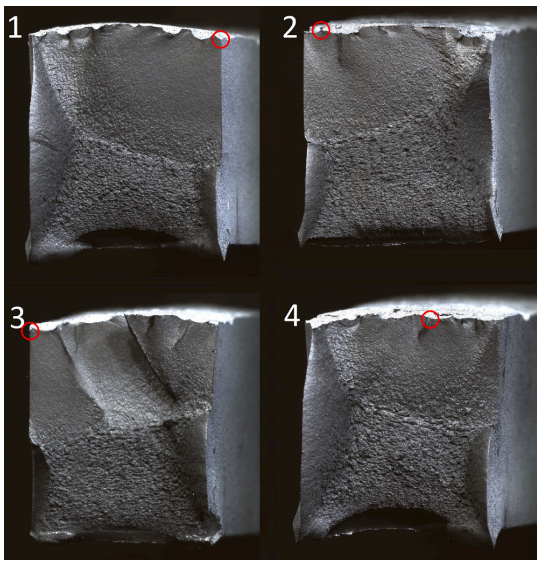

Fig. 14. Fracture surfaces of all specimens, viewed from positive *y* side. Red circles mark the earliest initiation sites for each surface.

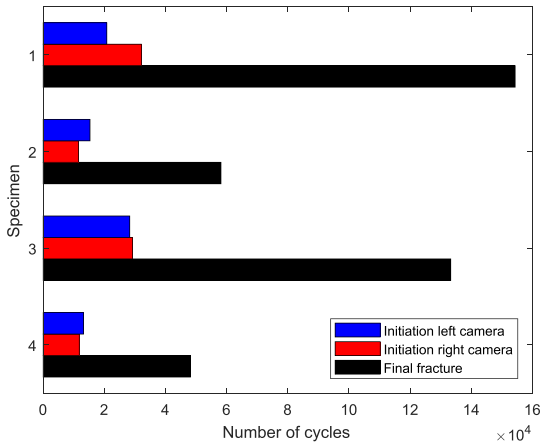

Fig. 15. Initiation and total lifetimes for all specimens.

maximum heights of the specimens varied between 22.6 and 23.5 mm. Specimen 2 and 4 seem to have a lower number of individual pits, but the pits have somewhat steeper walls than those in specimen 1 and 3, indicated by larger height gradients at the edges.

Fig. 12 shows examples of the raw photographs taken of the midsection of specimen 1 at different times for the purpose of DIC post-processing. To the naked eye, changes in the surface are barely visible even at frame c, at 78% of the specimen lifetime. In frame d, at 97% of the specimen lifetime, the crack that soon thereafter lead to final fracture, can be easily seen, along with one other crack.

The left sides of Fig. 13 show plane maps of stress amplitudes from FEA for all specimens. The color scales have been capped at the lower end to highlight the regions of relevant, high stresses. The right sides of Fig. 13 shows maps of initiating and growing cracks that were identified from DIC. The photographs of crack-free specimen surfaces are displayed in the middle figures, with red dots marking the locations where

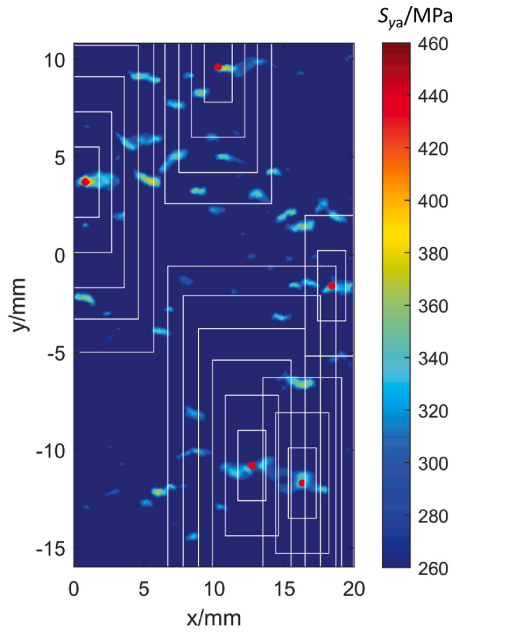

Fig. 16. Illustration of search algorithm for crack initiation applied to specimen 1. Red dots show crack initiation locations found by DIC, and the rectangles successively invalidates the FEA stress results in enclosing areas as cracks grow.

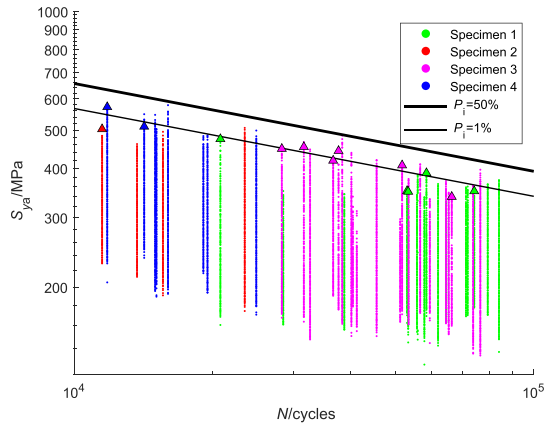

Fig. 17. An *S-N* curve for initiation in 0.1-by-0.1 mm element fitted to initiation and survival events from every specimen. The curve has a slope of $b = -4.49$ when taking the logarithms of the axes.

crack development occurred. Note that in the DIC maps, the cracks are plotted according to their location on the photographs, which might deviate slightly from locations of the corresponding stress concentrations in the plane coordinate systems of the FEA maps.

Fig. 13 shows that there is good correspondence between the calculated stresses and the initiation location of each crack. Several cracks were detected in all but specimen 2. When looking at Fig. 13, more cracks can be seen in the DIC plot for specimen 1 compared to Fig. 12. Moreover, the DIC criterion was shown to detect cracks at an early stage. As early as in frame b of Fig. 12, crack initiation was

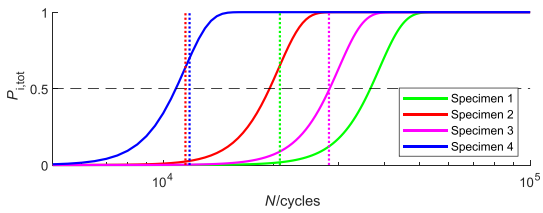

Fig. 18. Calculated probabilities of crack initiation for all specimens (solid lines), as well as recorded initiation lifetimes (dotted lines).

registered by DIC. No changes in the specimen surface were visible to the naked eye until much later.

As a crack grows and opens, a dark line becomes apparent on the photographs, as seen in Fig. 12. Eventually, the part of the DIC mesh interfering with the crack starts to break down and produce invalid displacement results. Therefore, this work was limited to detection of crack initiation and growth of small cracks. DIC measurements past the point of mesh breakdown were discarded. This is one reason why complete crack paths at final fracture are not shown on the crack development maps in Fig. 13. The time of mesh breakdown is stated by the maximum value on the color scale.

Another reason that full crack paths are not visible in Fig. 13, is that the initiation criterion works in retrospect. For crack initiation to be registered at a node pair, the inter-node displacement has to reach 0.90 px, even though the actual initiation time is registered earlier, at a time of only 0.15 px displacement. The result is that any node pair with a displacement between 0.15 and 0.90 px at the time of mesh breakdown does not show up on the crack development maps as initiated.

Macrographs of the final fractures of all specimens are shown in Fig. 14. Red circles mark the sites of the first initiations on the final crack surfaces. For the case of specimen 3 and 4, this was not the first initiation site for the specimen as a whole. In these specimens, secondary cracks outgrew the first crack that initiated. Since the crack development maps

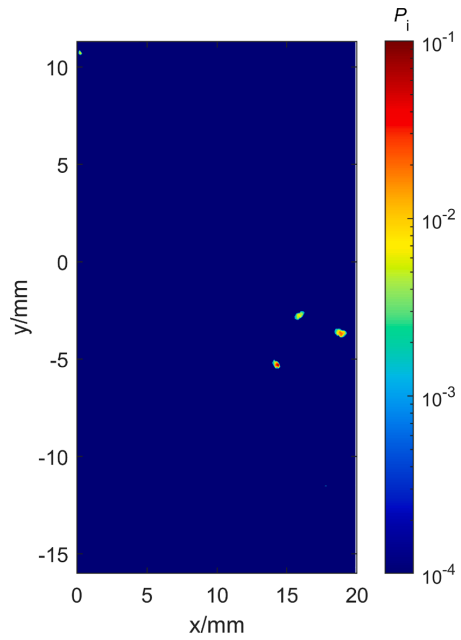

Fig. 20. Map of element crack initiation probability for the midsection of specimen 3 at the moment of measured initiation.

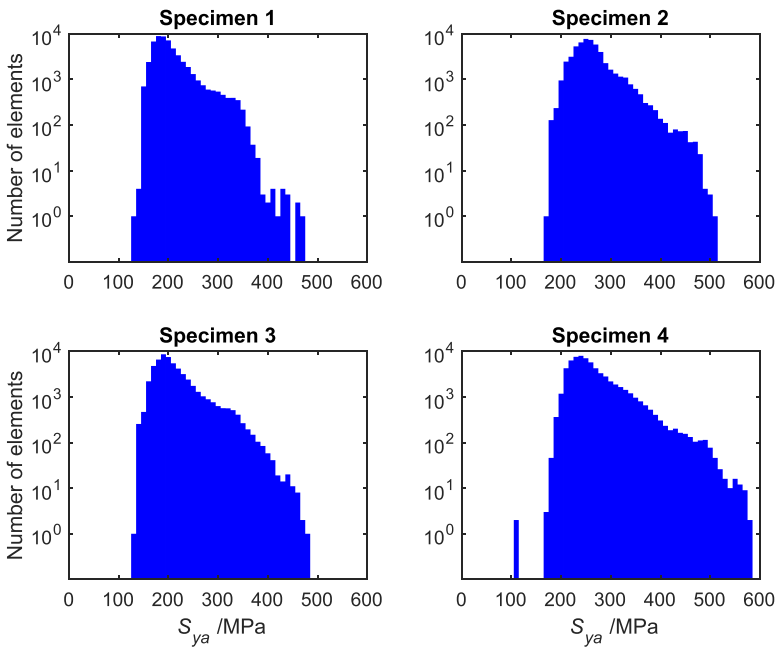

Fig. 19. S_{ya} distributions for all specimens, discretized into 10-MPa levels.

in Fig. 13 show cracks at a much earlier stage, it is difficult to correlate them completely to the appearance of the final fracture surfaces. However, Fig. 14 still provides some validation of the initiation location and early crack development measured by DIC.

Fig. 15 shows the total lifetimes for all specimens, registered at the final, unstable fracture. The earliest initiation lifetimes recorded by each camera is also shown. The deviations in the initiation lifetime could be due to differences in depth of field and field of view for the two cameras, or due to noise in the DIC results. Fig. 13 displays results from the camera showing the earliest initiation for each specimen. In order to produce conservative initiation lifetime results, that same camera was used for further results processing for the specimen.

It can be seen from Fig. 15 that crack growth dominates the fatigue lives at the current load levels, accounting for 76–87% of the lifetime of the specimens.

The algorithm for logging initiation events is illustrated in Fig. 16. The contour plot shows FEA stresses, and the red dots mark all initiation sites. As cycling progresses, the rectangles lined up in white encloses progressively larger regions of the specimen surface.

Data about initiation and survival of surface elements for all specimens has been plotted in an *S-N* diagram in Fig. 17. Dots mark survived elements, and triangles mark initiations. It should be noted that a total of fourteen independent initiation events could be plotted from the four specimens, i.e. ten more than from an ordinary fatigue test. Every region on a specimen being enclosed by a rectangle is shown by a vertical line of data points. For each specimen, the data points are spread out over a large portion of total lifetime. Thus, for components where the first crack initiation occurs early, the method provides a good basis for *S-N* curve fitting even for single-load-level test programs. An *S-N* curve, marked by black lines, was fitted to the results using maximum likelihood regression. The curve represents the probability of a crack initiating in a 0.1-by-0.1 mm element at a given time.

Solid lines in Fig. 18 shows the total cumulative distribution function of first initiation for every specimen, found by multiplication of element survival probabilities. The dotted lines represent the earliest recorded initiations. While cracks initiate in all specimens within the limits of the scatter, it happens at very low probabilities for specimen 1 and 2. The explanation lies in Fig. 17: Even though the *S-N* curve is based on data points from all specimens, specimen 1 and 2 have few surface elements that are stressed to levels of high initiation probability *at the moment of first initiation*. This just shows that there are variations in fatigue properties between the specimens, or between locations on them, that cannot be identified by stress calculations of the current scale.

Fig. 19 shows the number of surface elements exposed to each stress amplitude level for all specimens. As expected, it can be seen in Fig. 18 that it is the highest stress amplitudes, and the size of the area they cover, that controls the lifetime ranking of the specimens. Specimens 3 and 4 have more severe stress states than the correspondingly loaded specimens 1 and 2.

Finally, element crack initiation probabilities can be plotted as in Fig. 20. Although the appearance might not be much different from that of a stress amplitude map, it provides a properly scaled, graphical representation in the initiation probability across a specimen surface. It can be developed into a tool for quantitatively comparing the severity of corrosion pits of different shapes.

4. Discussion

Stresses in corrosion pits were calculated with FEA. Even though the mesh was not fine enough to capture stresses induced by microscopic surface features and roughness from corrosion, the calculated surface stresses showed a good correlation with initiation lifetimes, and an *S-N* curve with low scatter was produced. This may indicate that the detrimental effect on initiation life of any smaller-scale features is largely even across the surface. Thus, even though the macroscopic appearance of corrosion has been shown to vary significantly between mooring chain links[2], the constructed *S-N* curve might still be valid if stresses are calculated from FEA with the current mesh resolution. However, this follows an assumption that microscopic surface damage from general corrosion is equal for all levels of macroscopic damage, which is debatable. To further reduce scatter in lifetime predictions, microscopic surface profiles could be included in the FEA[30]. Taking into account sub-surface stress distributions could also reduce scatter[31].

A geometric feature that is present in the specimens, but not in a chain link, is the sidewalls. The lack of surrounding material near the edges of the corroded surface lowers constraint, facilitating crack initiation. This effect on the stress fields is well represented by the FEA and does not lead to any discrepancies between recorded lifetimes and calculated initiations stresses. However, cutting by EDM has been shown to introduce detrimental residual stresses, defects and metallurgical transformations[32], and milling is known to introduce shallow residual stresses that can affect fatigue lifetime both positively and negatively [33]. Since these effects are not accounted for in the FEA, they can be a source of scatter in the *S-N* curve. From Fig. 13 it can be seen that some cracks initiated from the edges of specimen 1 and 3. Even though most of these initiated from areas with high calculated stresses, the influence from machining stresses cannot be ruled out completely.

In the current tests, large fractions of the specimen lifetimes were found to be spent on crack growth. This indicates that the crack growth phase should be the main one to focus on for the purpose of lifetime prediction at the current stress levels. In full-size chain links, there might be larger surface regions of high stress than in the specimens. This would increase the probability of early crack initiation. Moreover, the cross sections are larger, so cracks have to grow longer before final fracture. Thus, the lifetime fraction of crack growth for a chain link might be even larger than what was registered for the specimens. However, if the chains are loaded to lower stresses, the situation may be another. Future small-scale tests should be run at load levels that give surface stresses corresponding to relevant full-scale tests of mooring chain segments.

Moreover, the current specimens were not tested in seawater. Even though the effects of the corrosive medium on crack initiation and growth lifetimes are less in laboratory fatigue tests of chain segments than in service, it should not be overlooked.

The effect of mean stresses was not considered here. Mean stresses are likely to affect the processes of crack initiation and growth from a corroded surface differently. Changing the mean stress might thus alter the time fractions of initiation and growth. In the current work, mean stress relaxation occurred in highly stressed areas because of yielding during the initial upload. In the most highly stressed point on specimen 4, R was reduced from 0.2 to −0.2. However, stress-raising, microscopic surface features might have caused the actual mean stress relaxation to be even more pronounced than calculated by FEA. In mooring chains, residual stresses from production have been identified as compressive in some critical crack initiation locations[22]. When superposing these to fatigue loading of the chains, R values may effectively be lowered. By designing a fatigue test program with more varying mean loads, the techniques described in the current work can be applied to investigate the effects on fatigue initiation life of corroded specimens.

DIC showed to be sensitive enough for crack detection, even when based on photographs of a highly irregular surface captured from an angle. High node coordinate resolution and accuracy is achievable and can likely be increased by rerunning the analyses using meshes where elements do not span the currently identified crack paths[26]. However, the crack initiation criterion could be made more robust, and alternative criteria could be evaluated. Moreover, better routines for transforming coordinates between DIC and FEA results should be developed, since manual linking is time consuming and vulnerable to human error. Any routine would benefit from more ideal camera placement.

Locations of the initiation sites were manually measured from the DIC maps in Fig. 13. This procedure may be prone to manual measuring errors and inaccuracies caused by the limited resolution of the DIC mesh. Therefore, based on an estimate of manual measuring accuracy, a

tolerance was included on initiation site location: When counting an initiation event, the highest stress within a 0.6 mm distance from the located initiation site was considered to be the initiation stress. However, this definition leads to a bias in the results, when concluding that the highest FEA stress is controlling crack initiation. The problem would be lessened if tolerances in initiation site localization could be lowered. This would be possible if using a more accurate coordinate linking technique and a finer DIC mesh.

Crack initiation in smooth specimens begins with cyclic slip within a single grain[6]. Since the element size in the DIC meshes in the current work is considerably larger than the grain size of the steel, it is unlikely that any intra-grain displacements would be picked up by the measurements. Additionally, the paint on the specimen surfaces likely acts to soften the most local discontinuities in the displacement field that is visible to the cameras. This means that the displacement that is measured as initiation at a node pair in the current work presumably comes from the strain field in front of, or opening of, a crack that is already spanning multiple grains. Considering that a DIC element measures 0.3 mm in the x direction, a crack with a strain field of that same width could go unnoticed. Since the initiation criterion works in retrospect, it would be difficult to stop a fatigue test at the time of initiation in order to examine the crack appearance.

The idea of taking the stress distribution across the whole specimen surface into account when calculating the probability of failure is not new. Discretization of the surface into homogeneously stressed elements represents a primitive application of the weakest link method[34]. A more advanced stress integration scheme could improve accuracy.

For future work, it is planned to apply the constructed crack initiation *S-N* curve to results from full-scale fatigue tests of chain links. If the total life of chain links could be predicted by combining results from the constructed *S-N* curve and those of an appropriate crack growth model, this would provide validation of the results obtained in the current work.

5. Conclusions

Specimens cut from corroded mooring chain links were fatigued in three-point bending, and the DIC technique was used to detect crack initiation locations. The initiation stresses were calculated by FEA. An algorithm for defining independent crack initiation events was implemented, and the results were used to construct a crack initiation *S-N* curve for corroded surfaces of mooring chains.

It was shown that DIC provides suitable coordinate data for detecting initiation and growth of multiple cracks on a corroded surface. When more crack initiation data is available per specimen, the number of specimens needed to develop a statistically sound results database is reduced, lowering testing costs.

For the current load levels, it was found that cracks initiated from the corroded surface within 13–24% of the total specimen lifetime. The fact that the majority of the specimen lifetimes were spent in crack growth, suggests that the primary focus should be on this phase for fatigue lifetime predictions of mooring chains. However, the current test program was limited in terms of stress levels, and a single stress ratio of $R = 0.2$ was used. Other stress states in mooring chains might yield other divisions of lifetimes in full-scale tests.

Declaration of Competing Interest

The authors declare that they have no known competing financial interests or personal relationships that could have appeared to influence the work reported in this paper.

Acknowledgments

The authors would like to acknowledge Christian Frugone (NTNU), for his extensive efforts in setting up the fatigue rig systems. Acknowledgment also goes to Trond Auestad, Egil Fagerholt and Per J. Haagensen (NTNU), for discussions on the DIC monitoring and fatigue test setup. The authors are grateful for financial support for the work received through the project KPN Lifemoor (RCN contract No: 280705).

References

[1] Gabrielsen Ø, Liengen T, Molid S. Microbiologically influenced corrosion on seabed chain in the north sea, in. In: Proceedings of the ASME 2018 37th International Conference on Ocean, Offshore and Arctic Engineering. ASME; 2018. https://doi.org/10.1115/OMAE2018-77460.

[2] K. Ma, Ø. Gabrielsen, Z. Li, D. Baker, A. Yao, P. Vargas, M. Luo, A. Izadparast, A. Arredondo, L. Zhu, N. Sverdlova, I.S. Høgsæt, Fatigue tests on corroded mooring chains retrieved from various fields in offshore west africa and the north sea, in: Proceedings of the ASME 2019 38th International Conference on Ocean, Offshore and Arctic Engineering [35]. doi: 10.1115/OMAE2019-95618.

[3] Fernández J, Storesund W, Navas J. Fatigue performance of grade r4 and r5 mooring chains in seawater, in. In: Proceedings of the ASME 2014 33rd International Conference on Ocean, Offshore and Arctic Engineering. ASME; 2014. https://doi.org/10.1115/OMAE2014-23491.

[4] Ø. Gabrielsen, K. Larsen, O. Dalane, H.B. Lie, S. Reinholdtsen, Mean load impact on mooring chain fatigue capacity: Lessons learned from full scale fatigue testing of used chains, in: Proceedings of the ASME 2019 38th International Conference on Ocean, Offshore and Arctic Engineering omae19. doi: 10.1115/OMAE2019-95083.

[5] Thorpe TW, Scott PM, Rance A, Silvester D. Corrosion fatigue of BS 4360:50D structural steel in seawater. Int. J. Fatigue 1983;5(3):123–33. https://doi.org/10.1016/0142-1123(83)90025-7. https://www.sciencedirect.com/science/article/pii/0142112383900257.

[6] Schijve J. Fatigue of Structures and Materials. 2nd Edition,. Netherlands: Springer; 2009. https://doi.org/10.1007/978-1-4020-6808-9.

[7] Gkatzogiannis S, Weinert J, Engelhardt I, Knoedel P, Ummenhofer T. Correlation of laboratory and real marine corrosion for the investigation of corrosion fatigue behaviour of steel components. Int. J. Fatigue 2019;126:90–102. https://doi.org/10.1016/j.ijfatigue.2019.04.041. http://www.sciencedirect.com/science/article/pii/S014211231930163X.

[8] Igwemezie V, Mehmanparast A. Waveform and frequency effects on corrosion-fatigue crack growth behaviour in modern marine steels. Int. J. Fatigue 2020;134:105484. https://doi.org/10.1016/j.ijfatigue.2020.105484. http://www.sciencedirect.com/science/article/pii/S0142112320300153.

[9] Turnbull A. Characterising the early stages of crack development in environment-assisted cracking. Corros. Eng., Sci. Technol. 2017;52(7):533–40. https://doi.org/10.1080/1478422X.2017.1348761.

[10] Evans C, Leiva-Garcia R, Akid R. Strain evolution around corrosion pits under fatigue loading. Theoret. Appl. Fract. Mech. 2018;95:253–60. https://doi.org/10.1016/j.tafmec.2018.02.015. http://www.sciencedirect.com/science/article/pii/S0167844218300387.

[11] Nicolas A, Co NEC, Burns JT, Sangid MD. Predicting fatigue crack initiation from coupled microstructure and corrosion morphology effects. Eng. Fract. Mech. 2019;220:106661. https://doi.org/10.1016/j.engfracmech.2019.106661. http://www.sciencedirect.com/science/article/pii/S0013794419303005.

[12] Liu L, Hou N, Ding N, Guo W. Interacting Effects of Internal Defects and Corrosion Pits on the Stress Concentration of Hourglass-Shaped Specimens. J. Fail. Anal. Prev. 2019;19(4):967–75. https://doi.org/10.1007/s11668-019-00682-2.

[13] Chen J, Diao B, He J, Pang S, Guan X. Equivalent surface defect model for fatigue life prediction of steel reinforcing bars with pitting corrosion. Int. J. Fatigue 2018;110:153–61. https://doi.org/10.1016/j.ijfatigue.2018.01.019. http://www.sciencedirect.com/science/article/pii/S0142112318300239.

[14] Zhao T, Liu Z, Du C, Liu C, Xu X, Li X. Modeling for corrosion fatigue crack initiation life based on corrosion kinetics and equivalent initial flaw size theory. Corros. Sci. 2018;142:277–83. https://doi.org/10.1016/j.corsci.2018.07.031. http://www.sciencedirect.com/science/article/pii/S0010938X18305687.

[15] M.D. McMurtrey, D.E. Mills, J.T. Burns, The effect of pit size and density on the fatigue behaviour of a pre-corroded martensitic stainless steel, Fatigue & Fracture of Engineering Materials & Structures 42 (1) (2019) 3–18, _eprint: https://onlinelibrary.wiley.com/doi/pdf/10.1111/ffe.12860. doi:10.1111/ffe.12860. https://onlinelibrary.wiley.com/doi/abs/10.1111/ffe.12860.

[16] E. Jones, M.E. Iadicola, A Good Practices Guide for Digital Image Correlation, 2018. doi:10.32720/idics/gpg.ed1.

[17] Mathieu F, Hild F, Roux S. Identification of a crack propagation law by digital image correlation. Int. J. Fatigue 2012;36(1):146–54. https://doi.org/10.1016/j.ijfatigue.2011.08.004. https://www.sciencedirect.com/science/article/pii/S0142112311002027.

[18] Zhu M-L, Lu Y-W, Lupton C, Tong J. In situ near-tip normal strain evolution of a growing fatigue crack. Fatigue & Fracture of Engineering Materials & Structures 2016;39(8):950–5. https://doi.org/10.1111/ffe.12391. https://onlinelibrary.wiley.com/doi/abs/10.1111/ffe.12391.

[19] J.D. Carroll, W. Abuzaid, J. Lambros, H. Sehitoglu, High resolution digital image correlation measurements of strain accumulation in fatigue crack growth, International Journal of Fatigue 57 (2013) 140–150, fatigue and Microstructure: A special issue on recent advances. doi: 10.1016/j.ijfatigue.2012.06.010. https://www.sciencedirect.com/science/article/pii/S0142112312002113.

[20] Rupil J, Roux S, Hild F, Vincent L. Fatigue microcrack detection with digital image correlation. The Journal of Strain Analysis for Engineering Design 2011;46(6):492–509. https://doi.org/10.1177/0309324711402764.

[21] Zarandi EP, Skallerud BH. Cyclic behavior and strain energy-based fatigue damage analysis of mooring chains high strength steel. Marine Structures 2020;70:102703. https://doi.org/10.1016/j.marstruc.2019.102703. http://www.sciencedirect.com/science/article/pii/S0951833919304186.

[22] Zarandi EP, Skallerud BH. Experimental and numerical study of mooring chain residual stresses and implications for fatigue life. Int. J. Fatigue 2020;135:105530. https://doi.org/10.1016/j.ijfatigue.2020.105530. https://www.sciencedirect.com/science/article/pii/S014211232030061X.

[23] Martinez Perez I, Constantinescu A, Bastid P, Zhang Y-H, Venugopal V. Computational fatigue assessment of mooring chains under tension loading. Engineering Failure Analysis 106 2019:104043. https://doi.org/10.1016/j.engfailanal.2019.06.073. https://www.sciencedirect.com/science/article/pii/S1350630718310914.

[24] ASTM International, West Conshohocken, PA, G1–03(2017) e1 Standard Practice for Preparing, Cleaning, and Evaluating Corrosion Test Specimens (2017). doi: 10.1520/G0001-03R17E01.

[25] Gabrielsen Ø, Larsen K, Reinholdtsen S-A. Fatigue testing of used mooring chain, in. In: Proceedings of the ASME 2017 36th International Conference on Ocean, Offshore and Arctic Engineering. ASME; 2017. https://doi.org/10.1115/OMAE2017-61382.

[26] Fagerholt E, Børvik T, Hopperstad O. Measuring discontinuous displacement fields in cracked specimens using digital image correlation with mesh adaptation and crack-path optimization. Opt. Lasers Eng. 2013;51(3):299–310. https://doi.org/10.1016/j.optlaseng.2012.09.010. https://www.sciencedirect.com/science/article/pii/S0143816612002801.

[27] S.S. Gorthi, P. Rastogi, Fringe projection techniques: Whither we are?, Optics and Lasers in Engineering 48 (2) (2010) 133–140, fringe Projection Techniques. doi: 10.1016/j.optlaseng.2009.09.001. https://www.sciencedirect.com/science/article/pii/S0143816609002164.

[28] Pollak RD, Palazotto AN. A comparison of maximum likelihood models for fatigue strength characterization in materials exhibiting a fatigue limit. Probab. Eng. Mech. 2009;24(2):236–41. https://doi.org/10.1016/j.probengmech.2008.06.006. http://www.sciencedirect.com/science/article/pii/S026689200800057X.

[29] Wormsen A, Härkegård G. Weibull fatigue analysis of notched components under constant and variable amplitude loading. In: Proceedings of the 9th International Fatigue Congress 2006. Elsevier; 2006.

[30] Skallerud B, As SK, Ottosen NS. A gradient-based multiaxial criterion for fatigue crack initiation prediction in components with surface roughness. Int. J. Fatigue 2018;117:384–95. https://doi.org/10.1016/j.ijfatigue.2018.08.020. https://www.sciencedirect.com/science/article/pii/S0142112318303943.

[31] Härkegård G, Halleraker G. Assessment of methods for prediction of notch and size effects at the fatigue limit based on test data by böhm and magin. Int. J. Fatigue 2010;32(10):1701–9. https://doi.org/10.1016/j.ijfatigue.2010.03.011. https://www.sciencedirect.com/science/article/pii/S0142112310000770.

[32] Ghanem F, Sidhom H, Braham C, Fitzpatrick ME. Effect of near-surface residual stress and microstructure modification from machining on the fatigue endurance of a tool steel. J. Mater. Eng. Perform. 2002;11(6):631–9. https://doi.org/10.1361/105994902770343629. https://doi.org/10.1361/105994902770343629.

[33] H. Sasahara, The effect on fatigue life of residual stress and surface hardness resulting from different cutting conditions of 0.45%c steel, International Journal of Machine Tools and Manufacture 45 (2) (2005) 131–136. doi: 10.1016/j.ijmachtools.2004.08.002. https://www.sciencedirect.com/science/article/pii/S0890695504001853.

[34] Wormsen A, Sjödin B, Härkegård G, Fjeldstad A. Non-local stress approach for fatigue assessment based on weakest-link theory and statistics of extremes. Fatigue & Fracture of Engineering Materials & Structures 2007;30(12):1214–27. https://doi.org/10.1111/j.1460-2695.2007.01190.x.

[35] Proceedings of the ASME 2019 38th International Conference on Ocean, Offshore and Arctic Engineering, Vol. 3, ASME, 2019.

Check for updates

Received: 29 April 2022 | Revised: 18 August 2022 | Accepted: 27 August 2022

DOI: 10.1111/ffe.13834

ORIGINAL ARTICLE

FFEMS Fatigue & Fracture of Engineering Materials & Structures WILEY

Effect of cyclic softening and mean stress relaxation on fatigue crack initiation in a hemispherical notch

Paul Qvale[1] | **Ershad P. Zarandi**[1] | **Alberto Arredondo**[2] | **Sigmund K. Ås**[3] | **Bjørn H. Skallerud**[1]

[1]Department of Structural Engineering, Norwegian University of Science and Technology (NTNU), Richard Birkelandsvei 1A, NO-7491, Trondheim, Norway

[2]Vicinay Marine Innovación, Plaza Ibaiondo 1, planta 1a, Leioa, ES-48940, Spain

[3]Department of Marine Technology, NTNU, Trondheim, NO-7491, Norway

Correspondence
Paul Qvale, Department of Structural Engineering, Norwegian University of Science and Technology (NTNU), Richard Birkelandsvei 1A, NO-7491 Trondheim, Norway.
Email: paul.qvale@ntnu.no.

Funding information
Norges Forskningsråd

Abstract

Corroded surfaces of offshore mooring chains typically show a very irregular shape with different pit geometries. Fatigue tests were performed in three-point bending on specimens with hemispherical notches, representing an idealized geometry of a corrosion pit. Digital image correlation was used to detect crack initiation lives and locations. The aim of the study was to quantify mean stress relaxation (MSR) and its influence on fatigue initiation life. MSR data were obtained from strain-controlled fatigue tests on R4-grade offshore mooring chain steel. Interestingly, MSR was observed even at a stress amplitude below the cyclic yield stress. For initiation lives below 100,000 cycles, significant improvement in predictions was obtained if cyclic softening and MSR were accounted for. Using only the monotonic stress-strain curve led to less accurate predictions. For longer lives, scatter in the base material *S-N* data and residual stresses from machining of the notch made predictions less accurate.

KEYWORDS

cyclic softening, digital image correlation, fatigue crack initiation, finite element, mean stress relaxation, offshore engineering

1 | INTRODUCTION

The structural integrity of offshore mooring chains is essential for safe operation of floating structures used for oil and gas extraction, wind energy production, and aquaculture. In order to accurately predict fatigue or corrosion fatigue lives of the chains, a good understanding of the material's cyclic stress-strain response is needed. A recent study by Zarandi and Skallerud[1] documented that strain-controlled load cycling of R4-grade mooring chain steel at initial stress amplitudes above its monotonic yield stress, $R_{p0.2}$, can significantly alter its stress–strain response. The material exhibited *cyclic softening* and *mean stress relaxation* (MSR)—effects that are often neglected in fatigue calculations.

If fatigue loading is high enough to cause cyclic plasticity, most metals exhibit either cyclic hardening or softening.[2] Materials that have been work hardened tend to soften.[2,3] Some materials have been reported to soften at low strain ranges and harden at high strain ranges.[4–6]

Manuscript submitted for review to *Fatigue & Fracture of Engineering Materials & Structures* April 29, 2022.

This is an open access article under the terms of the Creative Commons Attribution License, which permits use, distribution and reproduction in any medium, provided the original work is properly cited.
© 2022 The Authors. *Fatigue & Fracture of Engineering Materials & Structures* published by John Wiley & Sons Ltd.

The material response during cyclic plastic loading is governed by dislocation movements and the interaction between dislocations and the microstructure. Residual stresses that are present prior to cyclic plastic loading will relax by converting the elastic residual strains into microstructural plastic strains.[7] This mechanism can also lead to *cycle-dependent* MSR during non-symmetric (stress ratio $R \neq -1$) strain-controlled cyclic loading and ratcheting during stress-controlled loading.[3,8] It has been assumed that cyclic plastic straining is a prerequisite for MSR to occur.[3,5,9] However, significant MSR has been reported for mild steel at stress amplitudes of around $R_{p0.2}/3$.[6]

Neglecting MSR effects in fatigue life predictions may lead to non-conservative predictions if initially compressive stresses are assumed to exist throughout the life. Current models used to calculate MSR[10,11] can be somewhat physically based, in that they consider the evolution of yield surfaces and backstresses in a material continuum[10,11] or the amount of cold work.[12] However, it has been demonstrated that the former models often overestimate the amount of ratcheting or MSR.[10] Recent models have been developed to try to remedy this.[13] However, accurate MSR models are still lacking in commercial FEA codes.[14] Other MSR models[6,15,16] are purely empirically based, simply fitting an expression to the measured shift of mean stresses as a function of the number of load cycles. It can be argued that a model with a physical basis is more likely to be adaptable to a variety of conditions. However, cycle-by-cycle FEA for calculating the evolution of relevant stress tensors for a whole component is often impractical due to the high computational cost.

Offshore mooring chains are subject to general and microbiologically influenced corrosion attacks.[17,18] During cyclic loading, corrosion pits act as stress raisers, and may become initiation sites for corrosion fatigue cracks.[18] The current work aims to improve the understanding of MSR and its influence on fatigue initiation. Since corrosion pits vary in size and shape,[19] machined, hemispherical notches are considered here in order to develop a generic approach for MSR in R4-grade steel chains. This simplification is consistent with a previous study of local strains around corrosion pits.[1] Some studies using physically based MSR and ratcheting models in stress-strain calculations for cyclically loaded notches exist.[8,20,21] However, results of such calculations are not as easily verified as for smooth specimens.

In the current work, the transient stress-strain response, specifically cyclic softening and MSR, was calculated based on low-cycle fatigue results from Zarandi and Skallerud[1] and a complementary fatigue test performed at a lower strain level. A proposed MSR model was then used to predict fatigue initiation times and locations in hemispherical notches. Half of the specimens had compressive residual surface stresses, induced by an initial overload, to replicate the stress state found in a crown of an offshore mooring chain link.[22,23] Fatigue initiation life and locations were verified from fatigue tests by continuous monitoring with digital image correlation (DIC).

2 | INVESTIGATION OF TRANSIENT STRESS-STRAIN RESPONSE IN R4-GRADE STEEL

Zarandi and Skallerud performed strain-controlled fatigue tests on R4-grade steel specimens extracted from the straight part (shank) of a mooring chain link.[1] It was found that the monotonic and cyclic stress-strain curve for the material can be described by the Ramberg-Osgood (RO) relation,

$$\varepsilon = \frac{\sigma}{E} + \left(\frac{\sigma}{K}\right)^{1/n}, \tag{1}$$

with parameters as noted in Table 1. σ denotes the stress, and ε denotes the strain. Parameters in in Table 1 for monotonic loading were derived from a single stress-strain test, while parameters for cyclic loading were based on eight tests performed at fully reversed loading (strain

TABLE 1 Ramberg-Osgood parameters identified for monotonic and cyclic loading R4-grade mooring chain steel[1]

Parameter	Symbol	Monotonic loading	Cyclic loading (stabilized)	First load reversal
Strain hardening exponent	n	0.0463	0.0688	0.1397
Strain hardening coefficient/MPa	K	1124	966	3316
Elastic modulus/GPa	E	207	207[a]	195
Yield stress/MPa	$R_{p0.2}$	843	630	N/A

Note: A provisional model for the first load reversal is included in the rightmost column.

[a]In the current work, the apparent strain range dependency on E that was measured at high strain ranges[1] was disregarded, and the value of E for monotonic loading was adopted to the cyclic material model.

ratio $R_\varepsilon = -1$). Moreover, in three non-symmetrically loaded tests performed at strain amplitude $\varepsilon_a = 0.0045$ and $R_\varepsilon = -0.33$, $R_\varepsilon = 0$ and $R_\varepsilon = 0.33$, mean stresses were found to relax by more than 90% during the fatigue half-life of the specimens.[1] The rate of MSR was shown to be highest during the first few cycles, an observation that is consistent with observations of MSR in other steels.[2,5,13]

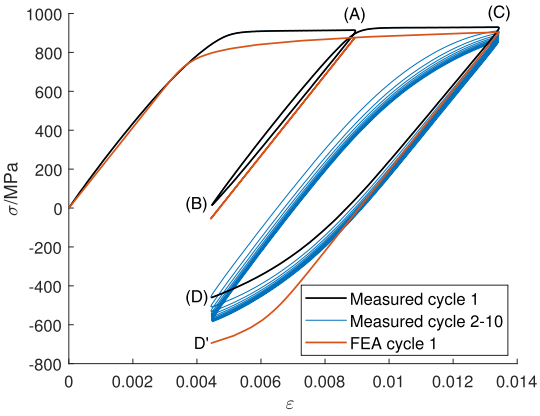

FIGURE 1 Stress-strain history for one of the non-symmetrically loaded tests ($\varepsilon_a = 0.0045$, $R_\varepsilon = 0.33$)[1] compared with FEA using the monotonic material model from Table 1. On execution of the test, the specimen was strained according to the following sequence: zero - mean (A) - minimum (B) - maximum (C) - minimum (D). Thereafter, the specimen was cycled between the strain levels of C and D until failure. The first 10 cycles are displayed [Colour figure can be viewed at wileyonlinelibrary.com]

In Figure 1, the stress–strain response for the first cycle (black line) and the nine subsequent cycles (blue line) in one test are shown in more detail. Also shown are results from elastoplastic finite element analysis (FEA) using the monotonic material model from Table 1 with kinematic hardening. While the maximum stress (point C) in the first cycle is reasonably well replicated by FEA, there is a discrepancy between the measured (D) and calculated (D′) minimum stress. This is caused by instant softening that manifests itself as non-Masing behavior.[1,24] Using the computed stress values at point C and D′ directly in fatigue calculations would yield large errors in mean stress estimates. However, it was observed that the stress-strain curves for the first load reversal (C to D) for all values of R_ε had almost identical shapes, indicating that the unloading behavior was independent of the magnitude of the maximum strain. Thus, as an alternative to the Masing model, a RO relation with parameters given in Table 1 could be fitted to the unloading curve by least-squares regression (with coefficient of determination, $R^2 = 0.9976$). This then provides a much better a much better estimate for the initial mean stress, which is the basis for the MSR calculation described in Section 3.2.2.

For the non-symmetrically loaded tests by Zarandi and Skallerud,[1] Figures 2 and 3 show the evolution in the

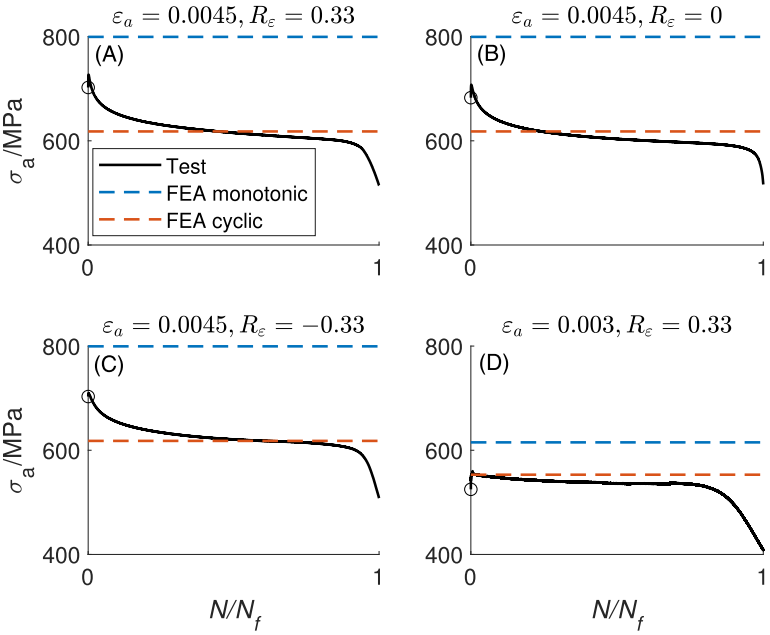

FIGURE 2 Measured stress amplitudes through the fatigue lives of specimens from Zarandi and Skallerud[1] and the current work, compared with FEAs using the monotonic and cyclic material models [Colour figure can be viewed at wileyonlinelibrary.com]

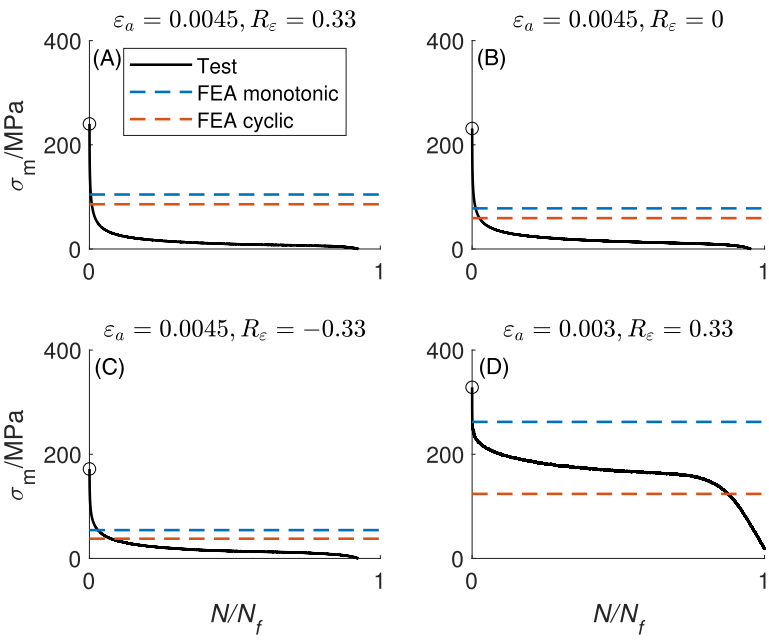

FIGURE 3 Measured mean stresses through the fatigue lives of specimens from Zarandi and Skallerud[1] and the current work, compared with FEAs using the monotonic and cyclic material models [Colour figure can be viewed at wileyonlinelibrary.com]

Element	C	Mn	Cr	Ni	Mo	Si	Fe and minor constituents
Percentage	0.24	1.3	1.3	0.7	0.3	0.3	Balance

TABLE 2 Chemical composition measured in chain links from the same production batch as the specimens were extracted from

stress amplitude, σ_a, and mean stress, σ_m, as a function of the ratio between the elapsed number of cycles, N, and the failure life, N_f. One additional test was made in the current work at a lower strain amplitude, $\varepsilon_a = 0.003$, and $R_\varepsilon = 0.33$ to complement the previous tests. The test setup was identical to that described by Zarandi and Skallerud,[1] except that the load frequency was 0.5 Hz, the wave shape was sinusoidal, and an Instron 100 kN servo-hydraulic machine was used. From Figure 3D, 49% MSR at half-life can be identified for the specimen run at $\varepsilon_a = 0.003$. The strain amplitude corresponds to an elastically calculated $\sigma_a = 621$ MPa, which means there is significant MSR at a stress amplitude well below the monotonic yield stress of the material (cf. Table 1). Moreover, the blue dashed lines in Figure 2 confirm that σ_a for the first load cycle cannot be calculated accurately for any of the tests by using the monotonic material model in an FEA. However, the red lines show that the cyclic material model can adequately represent the stabilized stress amplitude. Regarding the mean stress, neither the initial nor the stabilized value is well represented by any of the two models without correction.

3 | FATIGUE TESTING OF SPECIMENS WITH HEMISPHERICAL NOTCHES

3.1 | Experimental setup

3.1.1 | Specimen preparation

For the study on hemispherical notches, eight specimens were extracted near-surface from the non-welded shanks of two connected Ø114 mm mooring chain links made from R4-grade steel. The chain links had been processed according to standard specifications.[25] The chemical composition of chain links from the same production batch is given in Table 2. The tests by Zarandi and Skallerud were also conducted on material from a link from the same chain. The current fatigue testing was performed in conjunction with a study of fatigue initiation from natural corrosion pits[19] and thus involved a chain that had been in service and submerged in sea water. The chain links had been in service on a floating production storage and offloading (FPSO) vessel for 20 years. The specimens

were cut from the chain links using electrical discharge machining (EDM) and then milled to their final dimensions shown in Figure 4. The coordinate system shown in the figure is used as a reference throughout this article. In half of the specimens, hereby referred to as the *as-machined* (AM) specimens, Ø3 mm hemispherical notches were drilled in the centers of the surfaces that had been facing outwards on the chain link. Before the notches were drilled in the other half of the specimens, one high loading-unloading cycle was applied to them to induce compressive residual surface stresses, as detailed in Section 3.1.2. These specimens are referred to as *pre-loaded* (PL) specimens. In the AM specimens, notches were drilled using a drill bit with a Ø3 mm hemispherical tip at 12,000 rpm and 180 mm/min feed rate. In the PL specimens, vibrations occurred during drilling when penetrating material with compressive residual stresses. To remedy this, the feed rate was reduced to just 0.2 mm/min, and the potentially dulled drill bit was replaced between drilling of each notch. After drilling, any remaining lips outside of the notches were removed by gently rubbing a #2000 grit sandpaper in the z direction.

3.1.2 | Preloading and fatigue setup

The PL specimens were first preloaded in three-point bending with a plastically deforming load and then unloaded. This resulted in a compressive residual stress field in the z direction opposite of the load surface.[26] The residual stress field was meant to represent that on the outside curved part (crown) of a proofloaded offshore mooring chain, where longitudinal residual stresses of −500 to −400 MPa had been measured close to the surface.[23]

Figure 5 shows the rig used for preloading and fatigue loading. During preloading of the PL specimens, a 44 kN load was applied at the load cylinder. After unloading, an average residual stress in the z direction of −332 MPa was calculated from X-ray diffraction stress measurements directly opposite of the attack line of the load cylinder on one specimen. The stress measurements were performed using a Proto iXRD with a Cr cathode run at 20 kV and 4 mA, and a 1 mm diameter aperture. Proto

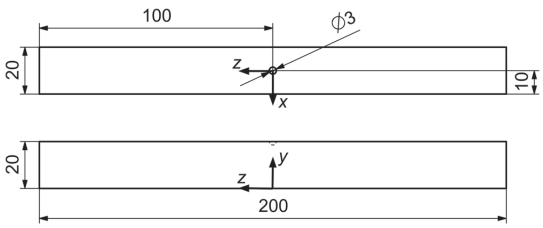

FIGURE 4 Fatigue testing specimen geometry

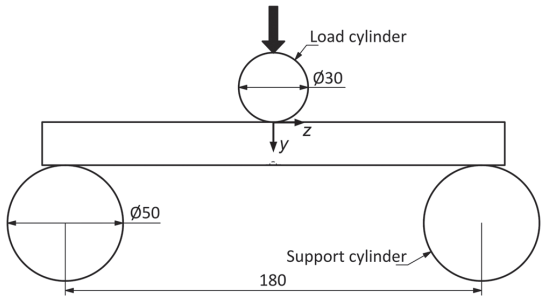

FIGURE 5 Schematic drawing of the three-point bending loading rig

XRDWIN software was used to analyze the result according to the $\sin^2\psi$ method using 11 beta angles (±20°). Elastoplastic FEA of the preloading was performed using the monotonic material model. Details about the FEA are provided in Section 3.2.1. Since the non-Masing behavior during unloading was not accounted for by the kinematic hardening model in the FEA (see Figure 1), Neuber's rule[27] was used to shift from the FEA result to the RO curve for first load reversal from Table 1. In good agreement with the measurements, a residual stress of −319 MPa was calculated.

The specimens then underwent cyclic loading according to Table 3. All load cycles had a load ratio of $R_L = 0.2$. The loads were applied using a triangular wave shape and a frequency of 3 Hz. Loading was applied using a calibrated Instron 8800 250 kN test system and an A10025E cylinder with a stroke of 250 mm.

It is apparent from Table 3 that the notch mean stress at the lowest load level was significantly lower in the PL specimen than in the AM specimen, because of the residual compressive stresses from preloading (e.g., compare results for specimens 1 and 5). For higher load levels, stress ranges were so high that maximum (and mean) stresses ended up at comparable levels. Minor differences in notch stress amplitudes between the AM and PL specimens in Table 3 at equivalent load levels were a result of plastic deformation of the contact surfaces with the load cylinder in the PL specimens during preloading. That is, the load cylinder had a larger contact surface for the PL specimens.

3.2 | Prediction of fatigue initiation life

3.2.1 | FEA model

FEA models with two symmetry planes were created in Abaqus 2017 for all specimens. Figure 6 shows the quadratic reduced integration (type C3D20R) element mesh. Doubling the element count along all axis directions for

TABLE 3 Load levels for each specimen

Specimen ID	Preloaded	Load amplitude (kN)	Mean load (kN)	Stress amplitude (MPa)	Mean stress (MPa)
1	No	8	12	479	407
2	No	8	12	479	407
3	No	10	15	569	340
4	No	12	18	638	292
5	Yes	8	12	467	135
6	Yes	10	15	558	306
7	Yes	12	18	628	349
8	Yes	14	21	678	334

Note: Surface stresses in z direction from the most highly stressed point (close to the mouth) in the notch are given. Calculations are performed by elastoplastic FEA using the monotonic material model and the RO relation for first load reversal. Stresses are valid for the first load cycle. Mean stresses include residual stresses.

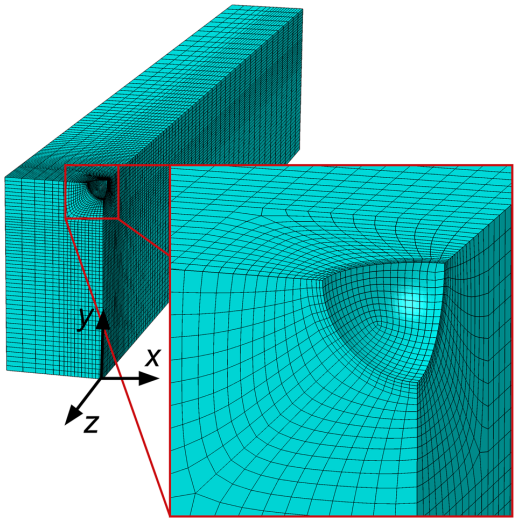

FIGURE 6 Mesh of FEA model [Colour figure can be viewed at wileyonlinelibrary.com]

one specimen resulted in less than 0.2% change in output values at the notch mouth. Thus, the original mesh was considered adequate for stress and strain representation.

It was assumed that all stresses from production of the chain links were completely relieved during specimen extraction. Thus, the specimens were modeled as initially stress-free.

"Hard," normal contact was modeled between the specimen and the load cylinder in order to accurately represent the plastic response in the specimen midsections during preloading of the PL specimens. The model was configured to take into account geometric nonlinearities. To replicate the specimen preparation process, preloading was simulated on notch-free models, and elements inside the notches were deactivated before fatigue loading was applied. Multilinear, kinematically hardening material models based on parameters from Table 1 were employed.

The post-processing of the FEA results to calculate fatigue initiation lives were performed in the numeric computing environment MATLAB. Procedures are detailed in the following section. In the calculations, both applied mean stresses and any residual stresses from preloading in the FEA results were considered as mean stresses.

3.2.2 | Fatigue initiation prediction

The highest stresses in Table 3 show that the test program extended into the low-cycle fatigue (LCF) domain. Therefore, strain-based fatigue initiation prediction, based on the Basquin[28] and Coffin-Manson[29,30] equations, was deemed most appropriate. For the specimens with the lowest loads and limited plastic strains, this approach reduces to a stress-based one. To account for mean stresses, the model of Smith, Watson and Topper (SWT)[31] was employed, resulting in the equation[2]

$$\sigma_{\max}\varepsilon_a = \frac{\sigma_f'^2}{E}(2N_i)^{2b} + \sigma_f'\varepsilon_f'(2N_i)^{b+m}. \quad (2)$$

Here, $\sigma_{\max} = \sigma_a + \sigma_m$ is the maximum stress during a load cycle. σ_f' and b are the Basquin parameters that signify the $N = 0.5$ intercept and the (negative) slope of an $S-N$ curve in a plot with logarithmic axes. ε_f' and m are equivalent Coffin-Manson parameters for an $\varepsilon_{plastic}-N$ curve. N_i is the number of cycles at fatigue crack initiation.

Stabilized stress and strain ranges to be used in the fatigue predictions were calculated at the notch surface using FEA and the cyclic material model with kinematic

hardening, since this model had shown in Figure 2 to give accurate representations. It can be argued that, as the load cycles are exerted on a specimen, the material will soften in regions where the stress amplitudes exceed the cyclic yield stress. Thus, the global cyclic response will approach that which can be represented by the cyclic material model.

In addition to the stress and strain ranges, an accurate estimate of the mean stresses is also needed to determine σ_{max} in Equation (2). An estimate was achieved by firstly calculating the mean stress in the first load cycle, by using FEA with the monotonic material model and then adjusting the minimum stress by shifting to the RO relation for first load reversal. The shift was performed while keeping the strain constant, equivalent to moving from point D′ to point D in Figure 1. Thereafter, a linear regression from Figure 7, based on the observations of MSR presented in Figure 3, was used to estimate the mean stress at half-life. Figure 7 shows the ratio of half-life mean stresses to initial mean stresses as a function of the strain range. Since mean stresses have been shown to quickly relax and approach more or less stable values, constant mean stresses equal to those at the half-lives were used in the fatigue predictions. Moreover, any resulting stress cycles with maximum or minimum values that exceeded the cyclic stress-strain curve, were adjusted accordingly.

It is widely accepted that fatigue initiation in components with steep stress gradients is not controlled solely by the highest surface stress amplitude.[32,33] Several methods have been developed to take the subsurface stress distribution into account.[32] Taylor's point-based critical distance method[34] was adopted in the current work. Instead of evaluating the surface state in the notch, this method considers the stress and strain at some distance (related to the crack process zone) below the surface. Thus, in the notch, rather the subsurface than the surface stress was considered for the fatigue calculations. For locations in the notch, the critical distance was employed along the surface plane normals. The critical distance method was chosen because of its simple application to combined distributions of stress and strain. Moreover, an exhaustive review of fatigue tests on notched 30CrNiMo8 low-alloy steel specimens, showed that the method could provide reasonably accurate results for a variety of stress distributions.[32]

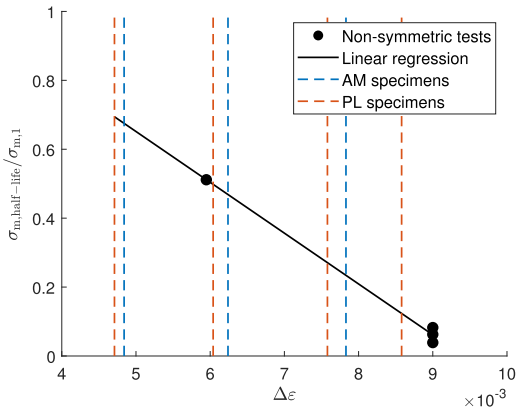

FIGURE 7 Linear regression model for the ratio of half-life mean stresses, $\sigma_{m,half-life}$, to initial mean stresses, $\sigma_{m,1}$, as a function of the strain range. Maximum strain ranges in the hemispherical notches, as well as results from the non-symmetrically loaded tests by Zarandi and Skallerud[1] and the current work have been plotted [Colour figure can be viewed at wileyonlinelibrary.com]

In lack of stress gradient sensitivity investigations for R4-grade steel, the same critical distance as for the thoroughly reviewed 30CrNiMo8 was used in the current work, that is, $d = 34$ μm.[32] Taylor has argued the critical distance of a material is related to its strength and grain size.[35] At 730–828 MPa[32] and 20–40 μm,[36,37] the yield strength and grain size of 30CrNiMo8 is comparable to 843 MPa[1] and 15–25 μm measured for R4-grade steel. This provides some support to the claim that d should also be similar for the two materials. Stresses and strains at critical distance from the surface was found by linear interpolation between FEA element nodal values at and 50 μm below the surface.

At $d = 34$ μm from the surface, calculated von Mises stress amplitudes deviated by less than 4.5% from the corresponding normal stress amplitudes within the top 30° from the notch mouth. This indicated low degree of multiaxiality in the stress states. Thus, little difference can be expected between alternative multiaxial stress criteria,[38] and the z-direction/normal stress and strain was conveniently used for the fatigue initiation analysis. In summary, Figure 8 shows the complete methodology for the fatigue prediction that was performed along the notch profile.

For the fatigue calculations, low-cycle and high-cycle S-N data for R4-grade steel were collected from Zarandi and Skallerud[1] and Arredondo et al,[39] respectively. Some additional, previously unpublished data points from Arredondo's test program were included. It was assumed that the use of smooth, small-scale specimens in the referenced test programs promoted a high ratio of initiation to total fatigue life, so that the data could be used to predict initiation lives in the current notched specimens. At least for long fatigue lives, this should be a sound assumption. In addition to the $S-N$ data, $\varepsilon'_f = 0.725$ and $c = -0.6508$ were obtained from Zarandi and Skallerud.[1]

Figure 9 shows all raw data points from the test programs in blue and grey. In the figure, and throughout the

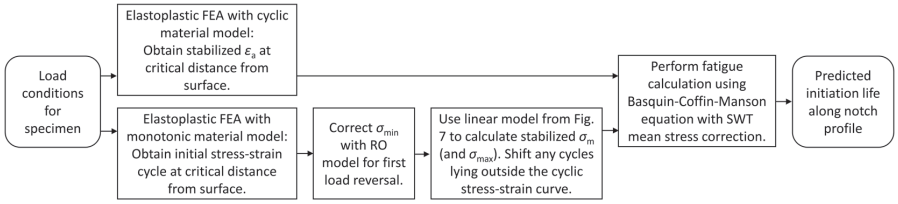

FIGURE 8 Flow chart for fatigue prediction methodology for the notched specimens

current work, arrows mark run-out tests—that is, tests where no failure occurred during the testing period. Zarandi and Skallerud's tests were run at stress ratio $R = -1$. Arredondo's tests were run at $R = 0.1$ and needed to be adjusted to $R = -1$ to produce correspondence. The inherent mean stress correction term of Equation (2), namely, $\sigma_{a,R=-1} = \sqrt{\sigma_{max}\sigma_a}$, was used to adjust the data points.[2] The adjusted points are shown by red markers in Figure 9.

Maximum-likelihood regression[19,40] was used to fit the most probable double-slope *S-N* fatigue initiation curve to the adjusted data, accounting for both failed and run-out tests.[†] That is, the best fits of both slopes, as well as the knee point, were determined simultaneously by iteration over all possible configurations for the whole data set. The *S-N* data was assumed to be Weibull distributed.[41] To accommodate the apparent large scatter in N in the lower part of the data, the regression was performed by treating N as the independent parameter. The data point from Arredondo with the lowest stress amplitude ($\sigma_a = 232$ MPa for $R = 0.1$) was considered an outlier and was thus not included in the curve fitting.

3.3 | DIC measurements of fatigue crack initiation life

Fatigue crack initiation was defined as the first sign of a crack that could be detected by DIC. DIC is a full-field monitoring technique[42] that has recently been employed to measure strain evolution around artificial corrosion pits[43] and crack initiation on naturally corroded surfaces[19] during fatigue testing but has never been used inside hemispherical notches. For acquiring photographs, one camera was placed in the *x-y* plane on each side of the specimen, at a 48° angle to the *x-z* plane. This allowed

[†]Although the horizontal position of a run-out data point in an *S–N* diagram is not defined, the run-out test suggests that the fatigue life is longer than the test duration, that is, that the *S–N* curve is located to the right of the point. This information is considered in maximum-likelihood regression.

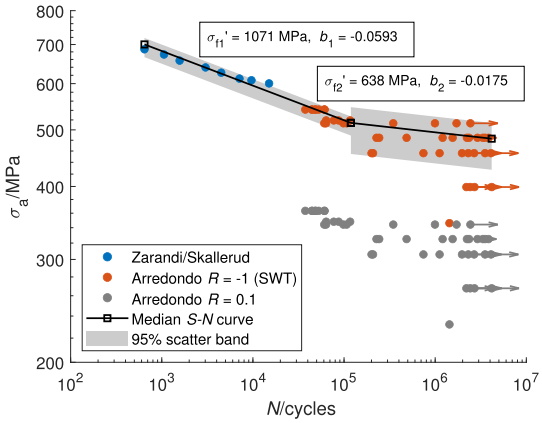

FIGURE 9 Double-slope *S–N* curve for R4-grade steel and $R = -1$, constructed by maximum likelihood regression on data from Zarandi and Skallerud[1] and Arredondo et al.[39] SWT's mean stress criterion has been used to shift the raw data from Arredondo. Arrows mark run-out tests [Colour figure can be viewed at wileyonlinelibrary.com]

the whole *x-y* plane surface profile of the notch of a specimen to be monitored. The DIC setup and crack detection criterion that were used in the current work are identical to those used by Qvale et al.[19] The reader is referred to Qvale et al[19] for a detailed description of the camera setup, DIC mesh, crack detection methodology and possible error sources.

4 | RESULTS

Figure 10 shows photographs of the notch of specimen 4 for DIC processing. The applied mesh in Figure 10B was used to track movement of surface points and detect crack initiation according to the detection criterion in Coffin.[19] Figure 10C shows a color plot of the displacement field in *z* direction for a crack that has grown past the mouth of a notch. Cracks at the initiation stage did not show up as distinct features in color plots but could be identified by tracking the inter-node displacements in MATLAB.

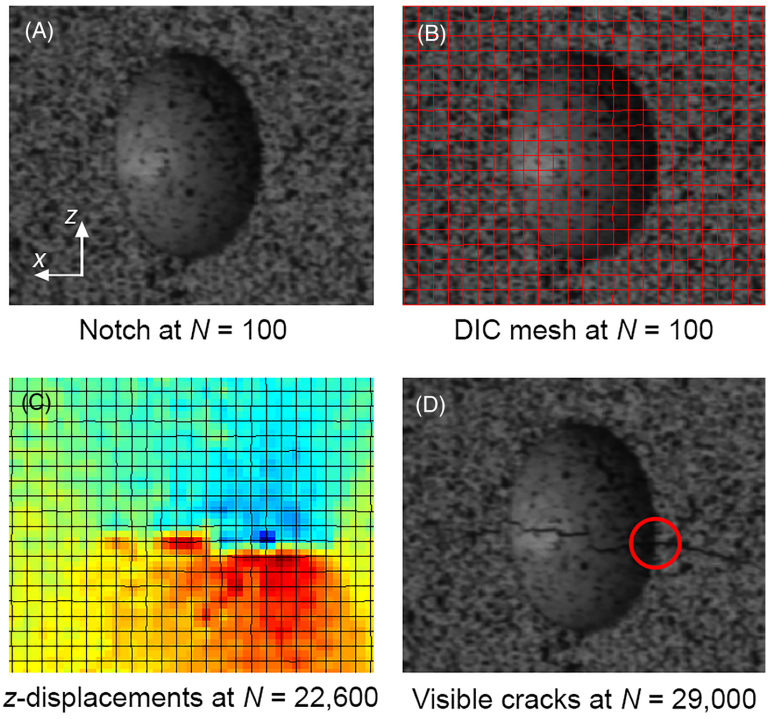

FIGURE 10 Crack development and DIC mesh for the notch in specimen 4. (A)–(D) all show the same section of the specimen. In (C), blue color shows positive displacements and red color shows negative displacements. In (D), the red circle shows the initiation location [Colour figure can be viewed at wileyonlinelibrary.com]

Crack surface lengths, $2c$, at the moment of detection could not be verified by other measurement techniques. Nevertheless, a crude estimate can be calculated based on FE solutions of Raju et al. for a semi-elliptical surface crack under bending load[44] and the current crack detection criterion, which signals a crack when the inter-node displacement across the crack plane reaches 2 μm.[19] The solution for the shallowest crack of Raju et al. (still a relatively deep crack with a depth-to-plate-thickness ratio of $a/t = 0.2$), when assuming $a/c = 0.8$ and a bending surface stress equal to the cyclic yield stress, yields a crack of $2c = 0.53$ mm for a crack mouth opening displacement of 2 μm.

Micrographs of all fracture surfaces where cracks initiated are shown in Appendix A (Figure A1). Specimen 8 was part of an individual study, and fatigue testing was stopped before final fracture.

Figure 11 shows the cycles to fatigue initiation registered by DIC, as well as the total fatigue lives, for all the tested specimens. It is apparent that at high load amplitudes the ratio of crack growth life to the total fatigue life is the highest. Two of the specimens tested at the lowest load level did not show any signs of fatigue initiation during the testing period. Moreover, the test at the highest load level was stopped after initiation, but before failure, for an independent fractographic study of the specimen. Longer initiation lives were documented for the PL specimens than for the AM specimens.

Figure 12 shows the predictions for fatigue initiation lives compared to measurements by DIC. The results are also given in table form in Appendix B (Table B1) and marked on fracture surfaces in Appendix A. Blue, unfilled markers signify predictions where the cyclic material model and MSR have been taken into account. For the red markers, MSR has been neglected. Finally, for reference, grey markers show the outcome of calculations based directly on FEA results where the monotonic material model has been used without any further post-processing. Isolines of the ratio $r = N_{\mathrm{i,predicted}}/N_{\mathrm{i,measured}}$ give indications of the accuracy of the results. It is apparent that the blue markers are closest to the $r = 1$ ideal line. Agreement is very good for $N_{\mathrm{i}} < 10^5$ cycles. For higher N_{i}, all methods yield very conservative predictions. Reasons for the deviations are discussed in the next section. "Cyclic" and "Cyclic+MSR" predictions fall together for the low load levels, meaning that it is here predicted that the cyclic softening alone is controlling the mean stress relaxation.

In Figure 13, notch profiles in the x-y plane are displayed for all specimens. For each notch, fatigue initiation lives have been plotted on logarithmic axes normal to the profile. This way of presenting the results allows

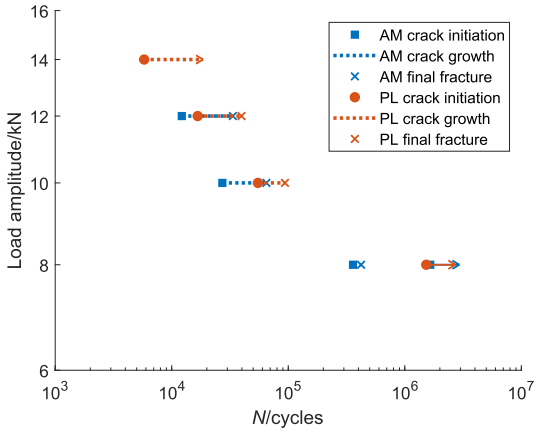

FIGURE 11 Measured numbers of cycles to fatigue initiation and failure for the notched specimens [Colour figure can be viewed at wileyonlinelibrary.com]

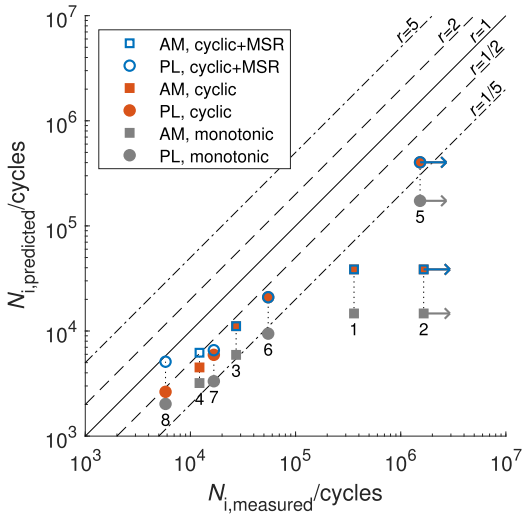

FIGURE 12 Predicted versus measured initiation lives for the notched specimens. "Cyclic" and "monotonic" refers to the respective material models used. Isolines of $r = N_{\mathrm{i,predicted}}/N_{\mathrm{i,measured}}$ are shown. The specimen numbers from Table 3 are printed below each vertical collection of points [Colour figure can be viewed at wileyonlinelibrary.com]

for easy identification of fatigue hotspots and initiation lives. The blue lines show the predicted initiation life distributions. Red dots show initiation locations and lives measured by DIC. Red error bars from a dot show the distance to neighboring DIC nodes, representing the surrounding region that is unmonitored and where the actual initiation could have occurred. Dashed red lines show the test duration of run-out tests without any registered fatigue initiation.

DIC readings on some specimens exhibited independent cracks growing from both sides of the notch. For these specimens, both initiations are marked in the diagrams. In specimen 7, identical initiation lives were registered in two nodes on the right side. This indicates that a crack initiated between the two nodes. A lot of noise was observed in the DIC measurements for specimen 8 because of low gray levels in the photographs. Thus, the results for this specimen are somewhat less accurate. Overall, it seems that the (2D) DIC routine was adequate to identify and display realistic developments of fatigue cracks on the curved notch surfaces.

Predictions indicated that the most likely location for fatigue initiation was just below the notch mouth, at 9 to 36° below the surface. Such observations are in line with previous calculations of stress and strain concentrations in hemispherically notched specimens[45,46] and mooring chain links.[1] Actual initiations were measured between 0.3 mm outside of the notch and 30° down in the notch and were in very good agreement with calculated locations. Variations in predicted initiation lives are generally small within the notch of one specimen. The exception is specimen 5, which is the only specimen with stresses in the bottom of the notch lying below the knee point of the $S-N$ curve.

5 | DISCUSSION

The current work has demonstrated by a fatigue test that mean stresses in R4-grade steel can relax by almost one half of the initial value at a stress amplitude well below the monotonic yield stress and just below the cyclic yield stress. This contradicts the suggestion that macroscopic plastic straining is needed for MSR to occur, as indicated by some authors for other materials.[3,5,9] However, in the current work, the stress at 0.2% plastic strain, $R_{\mathrm{p0.2}}$, is regarded as the yield stress. Further investigations are needed to determine the relationship between the onset of MSR and fatigue loading with very low plastic strains.

One could hypothesize that dislocations created during the initial uploading above the monotonic yield stress facilitates some cyclic plastic straining at lower stress amplitudes than the cyclic yield stress suggests. In Figure 1, an indication of macroscopic plasticity is the rapid deviation from elastic behavior at the first load reversal C-D. Even the initial, small cycle A-B-A exhibits a hysteresis loop, although the $\sigma_a = 450$ MPa is much lower than the cyclic yield stress of 630 MPa. The effect high mean strains on the cyclic material model should be investigated.

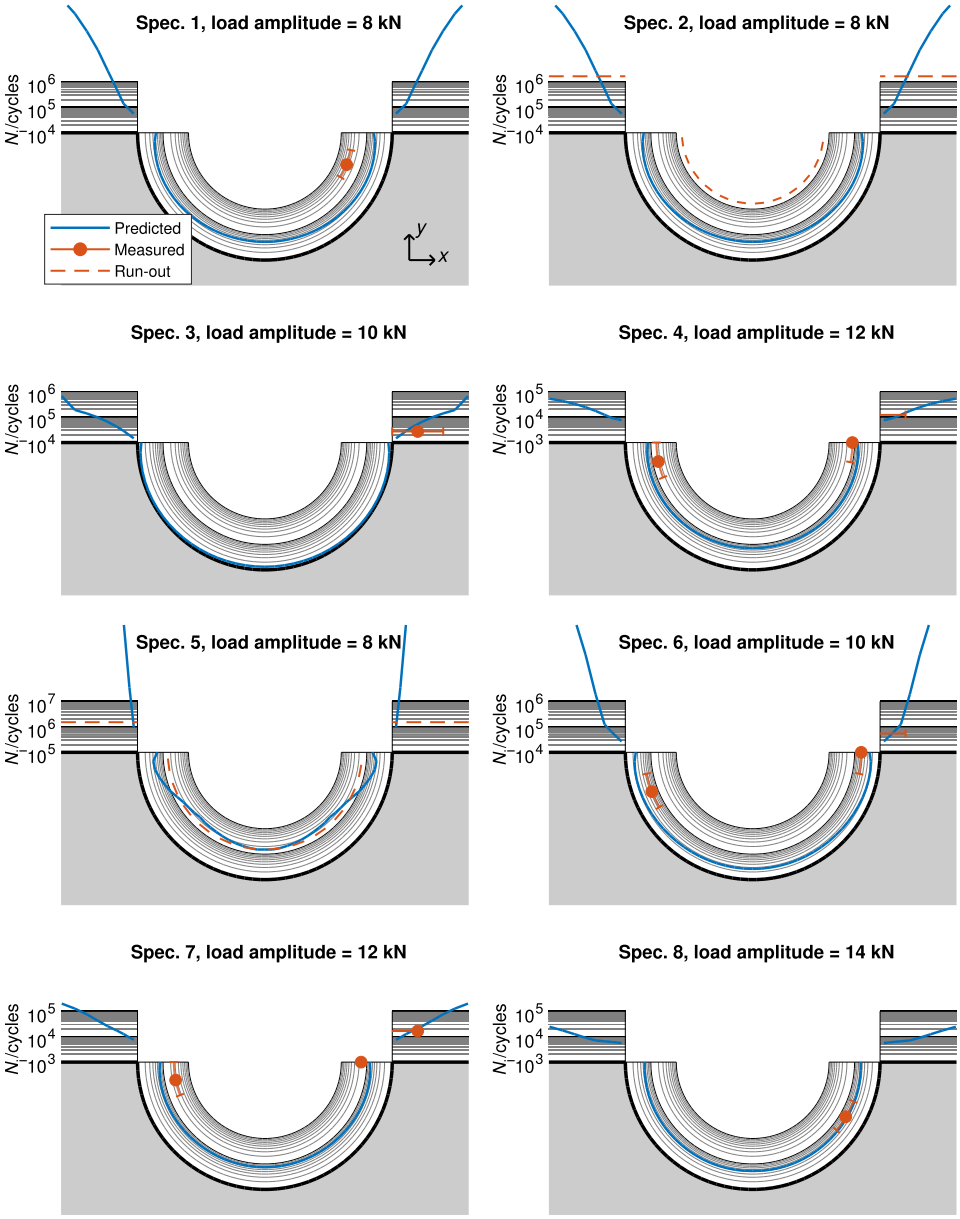

FIGURE 13 Predicted and measured fatigue initiation locations and lives at the notch profiles of all specimen. Specimens 1–4 and 5–8 are AM and PL specimens, respectively. Initiation lives have been predicted while accounting for cyclic softening and MSR [Colour figure can be viewed at wileyonlinelibrary.com]

The linear relation that was used to estimate the amount of MSR in the current work was based on measurements for only two strain ranges. It would probably have been possible to develop a more accurate model if test data from more strain ranges were available. Nevertheless, the amount of MSR that was observed should encourage taking this effect into account when predicting fatigue lives, and the current relation offers one way of doing so.

Preferably, a physically based plasticity model that can take into account both the non-Masing behavior at the first load reversal and the successive transient

behavior should be developed. Such an approach would be more robust than the current empirical fits and also able to account for stress states with a higher degree of triaxiality. Some recent studies show promising results, but need more experimental verification.[20] The RO model for the first load reversal seemed to predict residual stresses with high accuracy in the PL specimens after the overload. However, for more complex load histories, the use of the model becomes less trivial and its applicability more questionable. A first step towards a model that is universally applicable and simpler to use could be to try to capture the kinematic hardening behavior during the first load cycle that is not accurately represented by the current FEA model.

In Figure 1, there are apparent deviations between the FEA using the monotonic material model and the measured stress-strain behavior, not only for the unloading. Inability of the FEA to follow the loading path from zero to point A, indicates that material parameters can vary, also within one single production batch. This may result in deviations in fatigue predictions. For more accurate predictions, monotonic material model parameters could be based on the average behavior from a broader database of tensile tests on chain link material from the same production batch.

For all the notched specimens, taking in account cyclic softening and MSR in fatigue predictions led to more accurate results. Prediction accuracy is high for $N_{i,measured} < 10^5$. For longer initiation lives, deviations increase. Some possible explanations are discussed below.

Machining has the potential to create shallow residual stresses, with magnitudes highly dependent on process parameters, and that can be either tensile or compressive in the depth range of the estimated critical distance.[47–50] In the notched specimens, one can assume that the tangential feed motion of the ball end drill bit with respect to the notch mouth, or the very low feed rate used for drilling in the PL specimens, led to nonoptimal cutting conditions and aggravation of the residual stress state in the hot spots for fatigue initiation. It can be shown by geometric calculations that the current drilling parameters yields a cutting depth of of only 17 nm per revolution at the bottom of the notch, and 3 nm at 10 degrees from the mouth of the notch. For high load levels, the shallow residual machining stresses may have been redistributed and effectively removed by the first loading. For the low load levels, cyclic stresses might not have been high enough to induce plastic straining in regions of high, compressive residual machining stresses (since the maximum surface stress amplitudes are below the cyclic yield stress, cf. Tables 1 and 3). Thus, the machining stresses might have altered the effective mean stresses and been a major contributor to the observed deviations at long fatigue lives.

The scatter (in N) in the data in Figure 9 increases greatly when approaching the knee point of the S-N curve from the high σ_a side. Moreover, Lassen et al[51] document $S-N$ data points for $R = 0.1$ loading of R4 steel that are even deviating from those of Arredondo. In addition to the scatter, comes the uncertainty of using an empirical relation to correct non-symmetric stress cycles to equivalent symmetric ones. Stress amplitudes in the hemispherical notches at the lowest load levels lie quite close to the knee point, and the high scatter makes accurate prediction of initiation lives of single specimens challenging. Fatigue testing a larger number of hemispherically notched specimens at one load level would have yielded a measure of the scatter among these and allowed for a clearer comparison of predicted and measured initiation lives. Moreover, the gradual transition in the scatter around the knee point is not well represented by the current $S-N$ curve model. Moreover, the shallow slope that is predicted for the lower part of the $S-N$ curve might indicate that the stress amplitudes are close to the fatigue limit.

The increasing scatter in lower part of the $S-N$ curve in Figure 9 gives rise to a considerable size effect. That is, the probability of initiation in a specimen increases if the highly stressed region is enlarged. The area of a notch that had stress amplitudes above 90% of the highest one was around two orders of magnitude smaller than the homogeneously stressed area on specimens that the $S-N$ curve was constructed from. Taking the size of the stressed area into account would thus result in longer predicted initiation lives for the notched specimens.

A reason for the deviations in predictions could also have been that the critical distance for the material was not accurately determined, since it was adopted from a different alloy. Moreover, for higher load levels, the critical distance is known to increase compared to at the fatigue limit.[52] A sensitivity analysis presented in Appendix C showed that doubling the value of d improved the fatigue predictions somewhat but had generally small impact except for on specimen 5.

6 | CONCLUSIONS

In the current work, a non-symmetric fatigue test on R4-grade steel performed at a stress amplitude just below the cyclic yield stress showed that the initial mean stresses relaxed by 49% during the half-life of the specimen. This proves that MSR is significant also at relatively low loads and should be considered in fatigue predictions.

The non-Masing behavior of R4-grade steel controlled the mean stress in the first load cycle.

Eight specimens with hemispherical notches were fatigue tested in a three-point bending setup. Fatigue initiation lives were predicted, using an R4-grade-steel *S-N* curve compiled from the literature and taking into account the cyclic softening and MSR. This showed an improved accuracy over fatigue predictions based on the monotonic material model. Fatigue initiation locations were well predicted close to the mouths of the notches as measured by DIC. Good agreement between predicted and measured initiation lives was found for $N < 10^5$ cycles. For longer initiation lives, deviations were overly conservative. The deviations were likely caused by scatter in the $S-N$ data and residual machining stresses in the notches. A single value was used for the critical distance, independent on the load level. More accurate predictions are expected if a load dependent critical distance value is used.

Although the experimental data is limited, the current results show that MSR has a significant influence on fatigue initiation life in R4 steel. The approach outlined here is able to improve predictions in the finite life regime.

ACKNOWLEDGEMENTS

The authors would like to thank C. Frugone (NTNU) for his efforts to set up the fatigue rig and communications with the DIC system. P. J. Haagensen, T. Auestad, E. Fagerholt, L. Sandviken, M. Aursand, and L. Viespoli (NTNU and SINTEF) are also acknowledged for helpful discussions. The authors are grateful for financial support for the work received through the project KPN Lifemoor (RCN contract No. 280705).

NOMENCLATURE

a	crack depth
b	negative slope of the Basquin curve
c	crack half-length
d	critical distance
E	elastic modulus
K	strain hardening coefficient
m	negative slope of the Coffin-Manson curve
N	number of cycles
N_f	fatigue life
N_i	fatigue crack initiation life
$N_{i,measured}$	measured fatigue crack initiation life
$N_{i,predicted}$	predicted fatigue crack initiation life
n	strain hardening exponent
R	stress ratio
R^2	coefficient of determination
R_L	load ratio
$R_{p0.2}$	yield stress
R_ε	strain ratio
r	ratio of $N_{i,measured}$ to $N_{i,predicted}$
t	thickness
x, y, z	axes of Cartesian coordinate system
ε	strain
ε_a	strain amplitude
ε'_f	$N = 0.5$ intercept of the Coffin-Manson curve
$\varepsilon_{plastic}$	plastic strain
σ	stress
σ_a	stress amplitude
σ'_f	$N = 0.5$ intercept of the Basquin curve
σ_m	mean stress
$\sigma_{m,1}$	mean stress at first load cycle
$\sigma_{m,half\text{-}life}$	mean stress at half-life
σ_{max}	maximum stress

AUTHOR CONTRIBUTIONS

Paul Qvale contributed to the conceptualization, methodology, software, formalAnalysis, investigation, dataCuration, writingOriginalDraft, and visualization. Ershad P. Zarandi contributed to the conceptualization, methodology, investigation, and writingReviewEditing. Alberto Arredondo contributed to the investigation and writingReviewEditing. Sigmund K. Ås contributed to methodology, investigation, writingReviewEditing, supervision, and FundingAcquisition. Bjørn H. Skallerud contributed to conceptualization, methodology, writingReviewEditing, supervision, and fundingAcquisition.

DATA AVAILABILITY STATEMENT

The data that support the findings of this study are available from the corresponding author upon reasonable request.

ORCID

Paul Qvale https://orcid.org/0000-0002-7007-2865
Sigmund K. Ås https://orcid.org/0000-0003-2690-0851

REFERENCES

1. Zarandi EP, Skallerud BH. Cyclic behavior and strain energy-based fatigue damage analysis of mooring chains high strength steel. *Mar Struct*. 2020;70:102703.
2. Dowling NE. *Mechanical Behavior of Materials: Engineering Methods for Deformation, Fracture, and Fatigue*. 3rd ed. Upper Saddle River, NJ, USA: Pearson Prentice Hall; 2007.
3. Schijve J. *Fatigue of Structures and Materials*. 2nd ed.: Springer Netherlands; 2009.
4. Cofie NG, Krawinkler H. Uniaxial cyclic stress-strain behavior of structural steel. *J Eng Mech*. 1985;111(9):1105-1120.
5. Ellyin F. Effect of tensile-mean-strain on plastic strain energy and cyclic response. *J Eng Mater Technol*. 1985;107(2):119-125.
6. Jhansale HR, Topper TH. Engineering analysis of the inelastic stress response of a structural metal under variable cyclic

strains. In: Coffin LF, Krempl E, eds. *Cyclic Stress-Strain Behavior—Analysis, Experimentation, and Failure Prediction*. West Conshohocken, PA: ASTM International; 1971: 246-270.
7. James MR. Relaxation of residual stresses—an overview. In: Niku-Lari A, ed. *Residual Stresses*: Pergamon; 1987:349-365.
8. Hu W, Wang CH, Barter S. Analysis of Cyclic Mean Stress Relaxation and Strain Ratchetting Behaviour of Aluminium 7050. DSTO-RR-0153, DSTO Aeronautical and Maritime Research Laboratory; 1999. https://apps.dtic.mil/sti/citations/ADA367233
9. Koh SK, Stephens RI. Mean stress effects on low cycle fatigue for a high strength steel. *Fatigue Fract Eng Mater Struct*. 1991; 14(4):413-428.
10. Chaboche J-L, Kanouté P, Azzouz F. Cyclic inelastic constitutive equations and their impact on the fatigue life predictions. *Int J Plast*. 2012;35:44-66.
11. Frederick CO, Armstrong PJ. A mathematical representation of the multiaxial Bauschinger effect. *Mater at High Temp*. 2007; 24:1-26.
12. Zhuang WZ, Halford GR. Investigation of residual stress relaxation under cyclic load. *Int J Fatigue*. 2001;23:31-37.
13. Lee C-H, Do VNV, Chang K-H. Analysis of uniaxial ratcheting behavior and cyclic mean stress relaxation of a duplex stainless steel. *Int J Plast*. 2014;62:17-33.
14. Abaqus/cae user's guide; 2017.
15. Landgraf RW, Chernenkoff RA. Residual stress effects on fatigue of surface processed steels. In: Champoux RL, Underwood LH, Kapp JA, eds. *Analytical and Experimental Methods for Residual Stress Effects in Fatigue*. ASTM International; 1988:1-12.
16. Skallerud B, Larsen PK. A uniaxial cyclic plasticity model including transient material behaviour. *Fatigue Fract Eng Mater Struct*. 1989;12(6):611-625.
17. Gabrielsen O, Liengen T, Molid S. Microbiologically influenced corrosion on seabed chain in the north sea. In: Proceedings of the ASME 2018 37th international conference on ocean, offshore and arctic engineering. ASME; 2018: V003T02A045.
18. Ma K, Gabrielsen O, Li Z, et al. Fatigue tests on corroded mooring chains retrieved from various fields in offshore West Africa and the North Sea. In: Proceedings of the ASME 2019 38th International Conference on Ocean, Offshore and Arctic Engineering, Vol. 3. ASME; 2019:V003T02A060.
19. Qvale P, Zarandi EP, Ås SK, Skallerud BH. Digital image correlation for continuous mapping of fatigue crack initiation sites on corroded surface from offshore mooring chain. *Int J Fatigue*. 2021;151:106350.
20. Benedetti M, Berto F, Le Bone L, Santus C. A novel strain-energy-density based fatigue criterion accounting for mean stress and plasticity effects on the medium-to-high-cycle uniaxial fatigue strength of plain and notched components. *Int J Fatigue*. 2020;133:105397.
21. Wang CH, Rose LRF. Transient and steady-state deformation at notch root under cyclic loading. *Mech Mater*. 1998;30(3): 229-241.
22. Martinez Perez I, Constantinescu A, Bastid P, Zhang Y-H, Venugopal V. Computational fatigue assessment of mooring chains under tension loading. *Eng Fail Anal*. 2019;106:104043.
23. Zarandi EP, Skallerud BH. Experimental and numerical study of mooring chain residual stresses and implications for fatigue life. *Int J Fatigue*. 2020;135:105530.
24. Masing G. Eigenspannungen und Verfestigung beim Messing. In: Proceedings of the Second International Congress for Applied Mechanics; 1926:332-335.
25. Offshore standards, DNV-OS-E302, offshore mooring chain. DNV-OS-E302, DNV AS; 2021.
26. Zarandi EP. Multiaxial fatigue analysis of offshore mooring chains, considering the effects of residual stresses and corrosion pits. *Ph.D. thesis*: Trondheim, Norway: NTNU; 2020. https://hdl.handle.net/11250/2686419
27. Neuber H. Theory of stress concentration for shear-strained prismatical bodies with arbitrary nonlinear stress-strain law. *J Appl Mech*. 1961;28(4):544-550.
28. Basquin OH. The exponential law of endurance tests. *Am Soc Testing Mater Proc*. 1910;10:625-630.
29. Coffin LF. A study of the effects of cyclic thermal stresses on a ductile metal. *Trans ASME*. 1954;76:931-950.
30. Manson SS. Behavior of Materials Under Conditions of Thermal Stress. NACA-TN-2933, National Advisory Committee of Aeronautics; 1953.
31. Smith KN, Topper T, Watson P. A stress–strain function for the fatigue of metals. *J Mater*. 1970;5:767-778.
32. Härkegård G, Halleraker G. Assessment of methods for prediction of notch and size effects at the fatigue limit based on test data by Böhm and Magin. *Int J Fatigue*. 2010;32(10):1701-1709.
33. Skallerud B, Ås SK, Ottosen NS. A gradient-based multiaxial criterion for fatigue crack initiation prediction in components with surface roughness. *Int J Fatigue*. 2018;117:384-395.
34. Taylor D, Bologna P, Bel Knani K. Prediction of fatigue failure location on a component using a critical distance method. *Int J Fatigue*. 2000;22(9):735-742.
35. Taylor D. Geometrical effects in fatigue: a unifying theoretical model. *Int J Fatigue*. 1999;21(5):413-420.
36. Ahangarani S, Sabour AR, Mahboubi F. Surface modification of 30CrNiMo8 low-alloy steel by active screen setup and conventional plasma nitriding methods. *Appl Surf Sci*. 2007;254(5): 1427-1435.
37. Prohaska M, Panzenboeck M, Anderl H, Kordasch W. Influence of chemical composition and microstructural parameters on speed of sound of various materials used for high-pressure applications. In: 18th World Conference on Nondestructive Testing; 2012:16-20. https://www.ndt.net/search/docs.php3?id=12709
38. Bruun ØA, Härkegård G. A comparative study of design code criteria for prediction of the fatigue limit under in-phase and out-of-phase tension–torsion cycles. *Int J Fatigue*. 2015;73:1-16.
39. Arredondo A, Fernández J, Silveira E, Arana JL. Corrosion fatigue behavior of mooring chain steel in seawater. In: International Conference on Offshore Mechanics and Arctic Engineering, Volume 1: Offshore Technology; Offshore Geotechnics; 2016:V001T01A006.
40. Pollak RD, Palazotto AN. A comparison of maximum likelihood models for fatigue strength characterization in materials exhibiting a fatigue limit. *Probabilistic Eng Mech*. 2009;24(2): 236-241.
41. Wormsen A, Härkegård G. Weibull fatigue analysis of notched components under constant and variable amplitude loading.

In: Proceedings of the 9th International Fatigue Congress 2006. Elsevier; 2006.
42. Jones EMC, Iadicola MAE. A good practices guide for digital image correlation; 2018.
43. Evans C, Leiva-Garcia R, Akid R. Strain evolution around corrosion pits under fatigue loading. *Theor Appl Fract Mech*. 2018; 95:253-260.
44. Raju IS, Newman JC, Atluri SN. Crack-mouth displacements for semielliptical surface cracks subjected to remote tension and bending loads. In: Atluri SN, Raju IS, Newman JC, Epstein JS, eds. In: *Fracture Mechanics: Twenty-Second Symposium (Volume II)*. Philadelphia: ASTM International; 1992:19-28.
45. Cerit M, Genel K, Eksi S. Numerical investigation on stress concentration of corrosion pit. *Eng Fail Anal*. 2009;16(7):2467-2472.
46. Jie Z, Susmel L. High-strength steel wires containing corrosion pits: Stress analysis and critical distance based fatigue life estimation. *Fatigue Fract Eng Mater Struct*. 2020;43(8):1611-1629.
47. Ding W, Zhang L, Li Z, Zhu Y, Su H, Xu J. Review on grinding-induced residual stresses in metallic materials. *Int J Adv Manuf Technol*. 2017;88:2939-2968.
48. El-Khabeery MM, Fattouh M. Residual stress distribution caused by milling. *Int J Mach Tools Manuf*. 1989;29(3):391-401.
49. Ma Y, Feng P, Zhang J, Wu Z, Yu D. Prediction of surface residual stress after end milling based on cutting force and temperature. *J Mater Process Technol*. 2016;235:41-48.
50. Nespor D, Denkena B, Grove T, Böß V. Differences and similarities between the induced residual stresses after ball end milling and orthogonal cutting of Ti-6Al-4V. *J Mater Process Technol*. 2015;226:15-24.
51. Lassen T, Storvoll E, Bech A. Fatigue life prediction of mooring chains subjected to tension and out of plane bending. In: International Conference on Offshore Mechanics and Arctic Engineering, Vol. Volume 1: Offshore Technology; 2009:229-239.
52. Benedetti M, Santus C. Statistical evaluation of the critical distance in the finite life fatigue regime. *Procedia Struct Integr*. 2020;28:702-709. 1st Virtual European Conference on Fracture - VECF1.

How to cite this article: Qvale P, Zarandi EP, Arredondo A, Ås SK, Skallerud BH. Effect of cyclic softening and mean stress relaxation on fatigue crack initiation in a hemispherical notch. *Fatigue Fract Eng Mater Struct*. 2022;1-17. doi:10.1111/ffe.13834

APPENDIX A: FRACTURE SURFACES

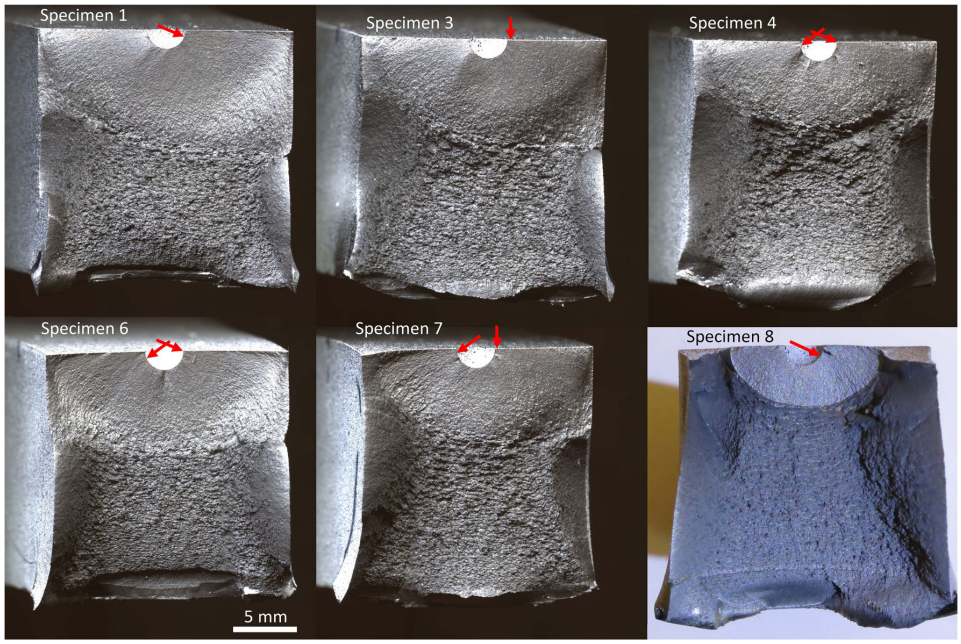

FIGURE A1 Micrographs of fracture surfaces of all notched specimens where cracks initiated. Red arrows mark initiation sites detected by DIC. Fatigue testing of specimen 8 was terminated before final fracture, in order to perform a separate study [Colour figure can be viewed at wileyonlinelibrary.com]

APPENDIX B: TABLE OF FATIGUE INITIATION LIVES

TABLE B1 Comparison between predicted and measured fatigue initiation lives

Specimen ID	**1**	**2**	**3**	**4**	**5**	**6**	**7**	**8**
Preloaded	Yes	Yes	Yes	Yes	No	No	No	No
Load amplitude (kN)	8	8	10	12	8	10	12	14
Mean load (kN)	12	12	15	18	12	15	18	21
$N_{i,measured}$	359,600	(1,653,300)	27,200	12,200	(1,527,610)	54,900	16,700	5800
N_f	421,328	-	64,920	33,452	-	93,605	39,687	(18,554)
Runout	No	Yes	No	No	Yes	No	No	After initiation
Values of $r = N_{i,predicted}/N_{i,measured}$.								
Cyclic + MSR	0.11	0.02	0.41	0.51	0.26	0.38	0.39	0.88
Cyclic	0.11	0.03	0.41	0.37	0.26	0.38	0.36	0.46
Monotonic	0.04	0.01	0.22	0.26	0.11	0.17	0.20	0.35

Note: Cycle numbers in parentheses mark the counts when fatigue testing was ended in run-out tests.

APPENDIX C: SENSITIVITY ANALYSIS ON CRITICAL DISTANCE

To investigate the sensitivity of the fatigue predictions to the critical distance, a sensitivity analysis was performed, where d was doubled from 34 to 68 μm. The results in Figure C1 show generally low impact on predictions, although accuracy improves slightly for all specimens. The increase in d has, however, a large effect on the maximum stresses in the notch of specimen 5, which is characterized by largely elastic stress cycling up from a highly compressive residual stress. Thus, fatigue predictions are greatly affected.

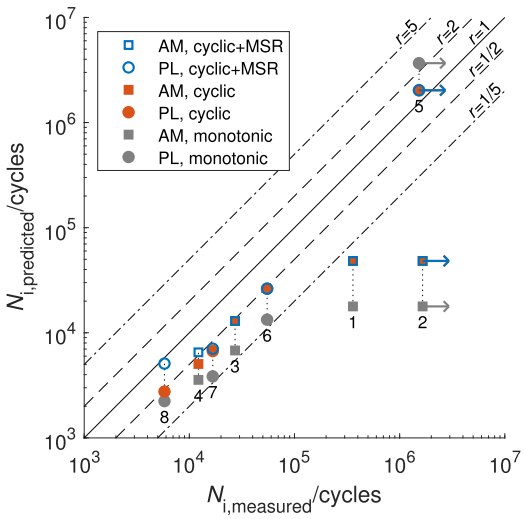

FIGURE C1 Predicted versus measured initiation lives for the notched specimens, if doubling the critical distance to $d = 68$ μm [Colour figure can be viewed at wileyonlinelibrary.com]

Marine Structures 85 (2022) 103236

Contents lists available at ScienceDirect

Marine Structures

journal homepage: www.elsevier.com/locate/marstruc

Effect of long periods of corrosion on the fatigue lifetime of offshore mooring chain steel

Paul Qvale [a,*], Håkon O. Nordhagen [b], Sigmund K. Ås [c], Bjørn H. Skallerud [a]

[a] Department of Structural Engineering, Norwegian University of Science and Technology (NTNU), NO-7491 Trondheim, Norway
[b] SINTEF Ocean, P.O. Box 4762 Torgard, NO-7465 Trondheim, Norway
[c] Department of Marine Technology, NTNU, NO-7491 Trondheim, Norway

ARTICLE INFO

Keywords:
Corrosion fatigue
Offshore mooring chain
Seasonal load variations
Fatigue crack growth
Crack tip blunting
Accelerated tests

ABSTRACT

R4-grade mooring chain steel specimens were subjected to alternating phases of saltwater corrosion and air fatigue to replicate seasonal load variations on chains in service. No significant difference in fatigue lifetimes was registered between precorroded specimens subjected to continuous fatigue and those periodically interrupted by phases of accelerated corrosion. Moreover, eight months of natural corrosion of specimens with fatigue cracks did not have a large effect on their remaining fatigue lifetimes. Retardation of fatigue crack growth by crack tip blunting from corrosion is deemed unlikely based on observations from the current work and the literature. Corrosion accelerated by anodic polarization is demonstrated to be unsuitable for replicating natural corrosion of fatigue cracks.

1. Introduction

Position mooring systems are integral parts of floating offshore structures used for oil and gas extraction, wind energy production and aquaculture. Uncoated steel mooring chains experience combined degradation from corrosion and fatigue. Design standards have been established based on laboratory fatigue tests on chain segments, some of which were carried out in seawater [1]. In order to keep test durations at acceptable levels, tests have been conducted at considerably higher loads and frequencies than those experienced by chains in service. While these tests are quite relevant for severe weather conditions, they provide no data for modeling the degradation during calm periods. Since corrosion is a time-dependent process, accelerating the tests means that the effect of corrosion is diminished.

Sea states in the North and Norwegian Sea are characterized by severe winter storms and much calmer summer conditions [2,3]. The calm sea states give rise to stress ranges that are below the cutoff in an accelerated test program. This implies that the intermediate periods between storms are essentially ignored, both in testing and in modeling, although cracks that initiated during a storm may very well be affected by corrosion processes during the calm summer months. This topic is explored in the current paper.

In mooring chains, general and microbiologically influenced corrosion reduce cross sectional areas and introduce macroscopic pits [4,5], increasing stresses globally and locally. Submersion in an electrolyte can accelerate fatigue damage development compared to that in dry air environment: The time of crack initiation is advanced by introduction of surface damage [6] and crack growth rates are believed to be enhanced by hydrogen embrittlement and film-rupture facilitated dissolution at the crack tip [7,8].

Under certain conditions, however, crack growth rates can also be *reduced*, by corrosion product-induced crack closure [7,9]. Moreover, dissolution at the crack tip implies that blunting may occur [7], which could reduce the local stresses at the crack tip.

* Corresponding author.
E-mail address: paul.qvale@ntnu.no (P. Qvale).

https://doi.org/10.1016/j.marstruc.2022.103236
Received 12 November 2021; Received in revised form 25 April 2022; Accepted 30 April 2022
Available online 21 May 2022
0951-8339/© 2022 The Author(s). Published by Elsevier Ltd. This is an open access article under the CC BY license (http://creativecommons.org/licenses/by/4.0/).

Observations of corrosion-induced blunting have been reported from several corrosion fatigue test programs: On the surface of high-strength steel in synthetic seawater at low loads, notch-like pits developed instead of narrow fatigue cracks [10]. For other high-strength steels in distilled water, an attempt to isolate the dissolution mechanism by anodic polarization indicated that blunting was responsible for the observed crack growth retardation [11]. Crack arrest, supposedly from crack tip blunting, has been reported for mild steel with prefabricated fatigue cracks at low load levels and frequency in 3.5% NaCl solution [12]. Also for 2024 aluminum alloy in 3.5% NaCl solution, a retarding effect on crack growth for low load frequency has been shown [13].

It has also been postulated that corrosion-driven dissolution of the free surface that a crack is growing from can retard fatigue damage development by reducing the effective crack depth, or even eliminating the crack altogether [14]. However, it has been demonstrated that crack initiation from a corrosion pit is controlled by the threshold stress intensity factor (SIF) range of an equally sized/deep crack [10,15,16]. Thus, if a short crack in a pit gets eliminated, it would quickly reinitiate from the encompassing, larger and more critical pit.

In the current work, the seasonal load variations on mooring chains have been simplified by assuming that no fatigue-driving load is exerted on the chains during the long "summer" season, and that fatigue is the dominating degradation mechanism during the short "winter" season. During summer, this leaves the corrosion mechanisms to act on fatigue damage over a much larger time scale than during continuous corrosion fatigue. This could lead to more pronounced crack tip blunting, as well as dissolution of a fatigue-damaged chain surface layer, if fatigue is still in the early stages of development. Since build-up of thick oxide layers in a crack in a corrosive environment is facilitated by repeated layer breaking and reforming from contact of the crack surfaces [9], it is assumed here that oxide-induced closure effects during the load-free summer season are limited.

Few records of test programs on alternating fatigue and corrosion exist — none on steel in sea water or other naturally, actively corroding substrate–electrolyte systems. Results from accelerated corrosion phases are difficult to correlate directly to realistic service environments and time scales [17,18], but they can still provide some indications on qualitative effects of corrosion. Alternating tests have been carried out on some aircraft aluminum alloys. Both slightly positive [19] and slightly negative [20] effect of corrosion on fatigue life have been registered. Periodic electropolishing of copper specimens between fatigue phases resulted in up to tenfold improvement in fatigue lifetime compared to continuous-fatigue lifetimes [21]. However, it is unlikely that such extreme trends can be observed for naturally corroding systems that induce corrosion pits.

In this article, two alternating corrosion and fatigue test programs on mooring chain steel are presented. Section 2.1 describes test program 1 (TP1), where the effect of periodic, accelerated corrosion on fatigue lifetimes was explored. The purpose of TP1 originally was to investigate if fatigue lifetimes could be prolonged by erasure of fatigue surface damage by corrosion at regular intervals. However, during a fatigue phase, cracks quickly initiated and grew past the surface layer affected by the next phase of corrosion. Thus, TP1 turned into an evaluation predominantly on the effect of accelerated corrosion on developed fatigue cracks. Section 2.2 describes test program 2 (TP2), where the effect of a single, eight-month period of natural corrosion in seawater on remaining lifetimes of fatigue-cracked specimens was investigated. The purpose of TP2 was to see if anodic dissolution would blunt the crack tip sufficiently to cause crack growth retardation. The design of the test programs allowed results for fatigue cracks at various stages of development to be obtained in a manageable time frame. It also provided some basis for comparison of natural and accelerated corrosion of fatigue cracks.

2. Methodology

2.1. TP1: Effect of periods of accelerated corrosion on fatigue lifetimes

In TP1, one group of precorroded specimens were fatigued to failure in air at room temperature. Fatigue tests on the other group of precorroded specimens were periodically interrupted, and the specimens underwent a phase of accelerated corrosion before fatiguing was resumed. This alternation was continued until failure, and the mean lifetimes of the two groups were compared. Specimens in the first and second group are hereafter referred to as *continuous fatigue* (CONT) and *alternating corrosion and fatigue* (ALT) specimens, respectively, even though they all underwent the same precorrosion phase.

Fatigue testing was done at high frequency in air. This was considered appropriate, since the dissolutive effect of corrosion on mooring chains is largest during the summer season. Corrosion was accelerated in order to complete several corrosion phases in a reasonably short time.

2.1.1. Specimen preparation

Notched specimens were cut from near the surface on the non-weld straight part of two connected ∅114 mm chain links made from R4-grade high-strength steel. The links had been laying on the deck of a floating production storage and offloading (FPSO) unit in the Norwegian Sea for 10 years. The links had minimal corrosion surface damage and had never experienced service loads. Figs. 1 and 2 show the cutting specification and machined specimen geometry. Yield strengths, $R_{p0.2}$, from position 5 of link 1 and 2 were measured to be 823 and 846 MPa, respectively. In both of the current test programs, it was assumed that any residual stresses from production of mooring chains [22,23] were relaxed during cutting of the specimens, and that any residual stresses that were introduced during machining were erased by material removal during the precorrosion phase.

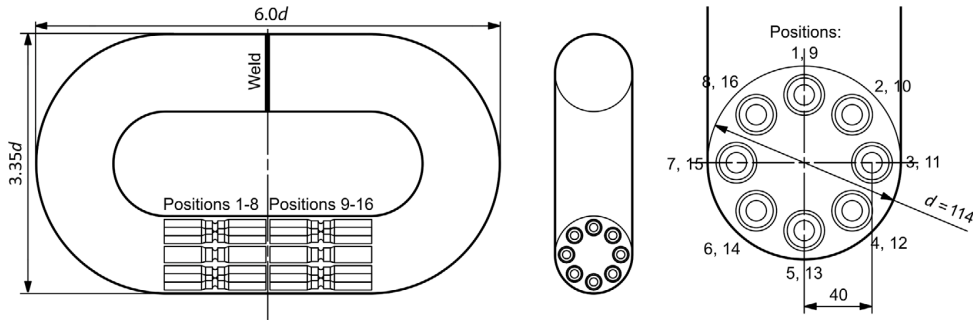

Fig. 1. Cutting specification for TP1 specimens from a chain link. All dimensions are given in millimeters.

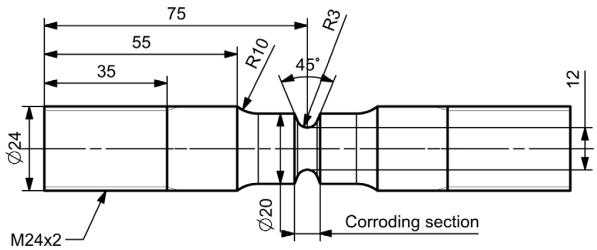

Fig. 2. As-machined specimen geometry for TP1. All dimensions are given in millimeters.

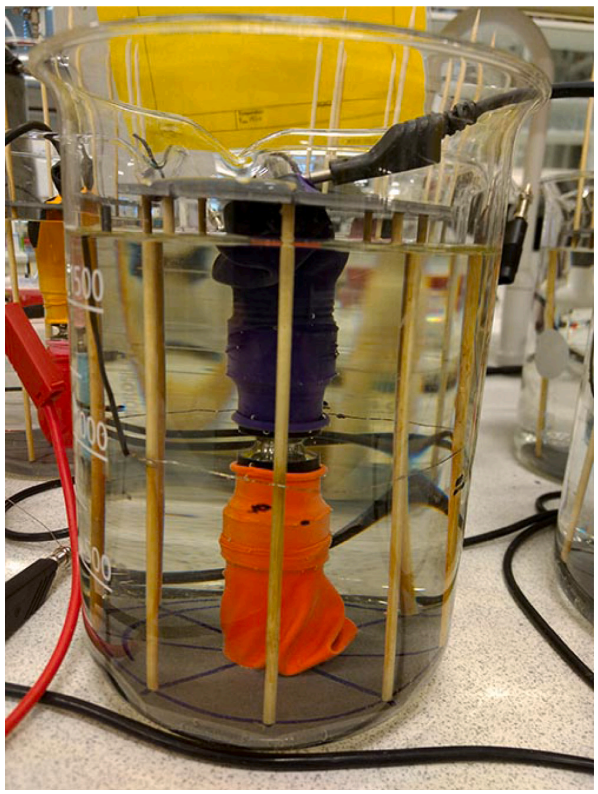

Fig. 3. Corrosion cell for anodic polarization of TP1 specimens during precorrosion and corrosion phases.

Fig. 4. Fatigue rig for tension loading in TP1. Housings of the spherical bearings that were installed to relieve any bending moment loads are visible.

2.1.2. Corrosion setup

The specimens were corroded in an unloaded state at room temperature in separate cells containing 3.5 wt% NaCl solution. All corrosion phases were accelerated by galvanostatic anodic polarization using a Gamry Interface 1000 galvanostat. The applied current density of 6.29×10^{-4} A/cm^2 was calculated [24] to give an average material removal rate of 20 μm/day across the corroding section of a specimen. The current density corresponds to a potential of about 100 mV above the open circuit potential [25]. The nominal surface area for application of current on the specimens was recalculated after the precorrosion phase. Platinum wire was used as cathode, arranged in a circular manner around each specimen, as shown in Fig. 3, to provide as uniform as possible current density in the notch surface on all sides. The non-corroding sections that are detailed in Fig. 2 were sealed off with tape. After each corrosion phase, any loose corrosion products were removed with a plastic brush, and the specimens were dried in warm air.

Precorrosion to remove 300 μm of material was carried out on all specimens to create a rough initial surface, and to limit the relative increase in roughness during subsequent corrosion phases. The corrosion phases on the ALT specimens were calculated to remove 100 μm of material per phase.

Corrosion rates of R4-grade and other carbon steels in seawater have been found to be 50–240 μm/year at temperatures below 18 °C [26,27]. The local corrosion rate on a chain link will depend on its location in a mooring line [28,29] and other factors. However, it can be concluded that 100 μm of average material removal by a corrosion phase is at least of the same order of magnitude as what can be expected on a chain from one summer season in service in the North or Norwegian Sea. The corresponding yearly corrosion rate on the specimens in the accelerated corrosion phases was 7.3 mm/year.

2.1.3. Fatigue setup

The specimens were fatigued in tension in an Instron 1603 electromagnetic resonance fatigue tester at a load frequency of about 170 Hz. Fig. 4 shows the fatigue rig. The load amplitude and ratio were 17 kN and 0.3, respectively. The load amplitude was calculated by finite element analysis (FEA) to correspond to a longitudinal stress amplitude in the notch after precorrosion of 281 MPa, when disregarding the stress raising effect from any corrosion pits. Details about all FEAs performed in the current work can be found in Appendix A. Fixings at both ends of the specimens had spherical bearings, to avoid any bending moment load on the specimens from misalignment. The temperature in the specimens during fatigue loading was not measured. Thus, no evaluation of the effect of temperature increase on fatigue lifetimes could be performed. For similar test programs in future research, this effect should be evaluated.

The tension fatigue setup and specimen geometry with a circular cross section and a relatively gentle notch was chosen to facilitate fatigue initiation in a limited segment of the specimen. This way, the development of fatigue damage or initiation in consistent locations on the circumference of the specimen could be followed during fatigue and corrosion phases. At the same time, the notch was not sharp enough to induce fatigue cracking immediately.

The CONT specimens (seven specimens) were fatigue tested until “failure”, i.e., full separation of the crack surfaces. Fatigue testing of the ALT specimens (eight specimens) was interrupted and corroded every 145,000 cycles (corresponding to about 46% of the recorded mean lifetime for the CONT specimens), in an attempt to conduct the corrosion phase before any large-scale crack growth had occurred. For clarity, the flowchart for TP1 is shown in Fig. 5.

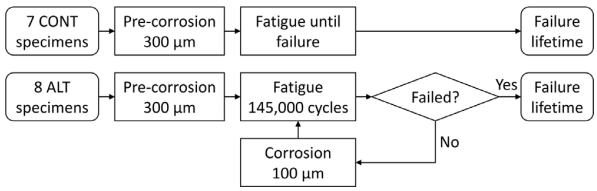

Fig. 5. Flowchart for TP1.

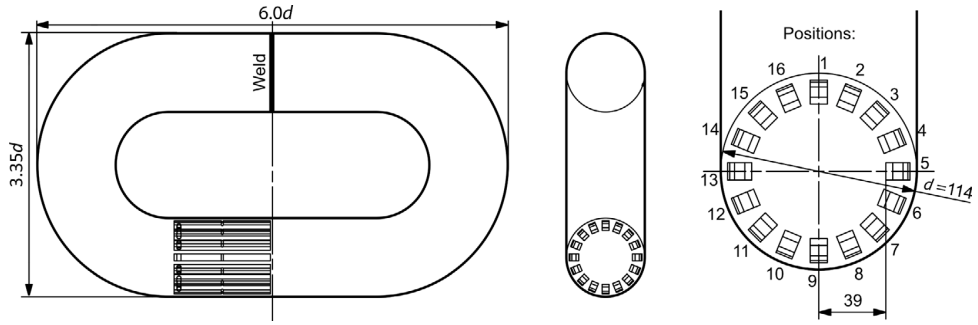

Fig. 6. Cutting specification from a chain link for the TP2 specimens. All dimensions are given in millimeters.

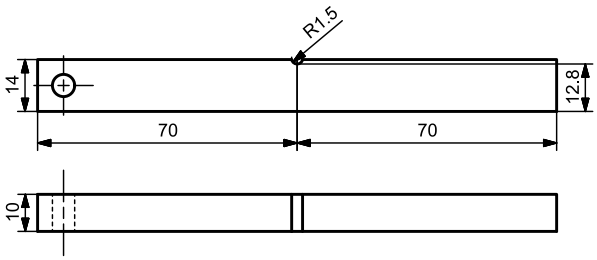

Fig. 7. As-machined specimen geometry for TP2. All dimensions are given in millimeters.

2.2. TP2: Effect of a period of natural corrosion on remaining lifetimes of fatigue-cracked specimens

For TP2, a group of *CONT* specimens were continuously fatigued to failure. A group of *ALT* specimens were fatigued until cracks of certain sizes had initiated. The ALT specimens were then left to corrode in seawater for eight months. Thereafter, fatiguing was resumed and continued until failure, and the remaining lifetimes were compared to that of the CONT specimens with similar crack sizes.

2.2.1. Specimen preparation

The TP2 specimens were designed for fatigue testing in a three-point bending setup. The reason for such a setup was that the bending stiffness of a specimen is sensitive to sizes of any cracks growing from the notch. This property was utilized to monitor crack growth, as described in detail in Section 2.2.3. Notched specimens were cut from the non-weld side of a link from the same chain as the specimens in TP1. Figs. 6 and 7 show the cutting specification and specimen geometry.

2.2.2. Corrosion setup

Precorrosion was carried out on all specimens, so that the ALT specimens, when cracked, could begin the subsequent corrosion phase with a homogeneously corroded surface free from residual machining stresses. The procedure and calculated average corrosion rate for the precorrosion phase was the same as in TP1, but only an average of 100 µm of material was removed. In the precorrosion cell, shown in Fig. 8, a platinum wire cathode was arranged at an even distance from the notch-side surface of the specimen to provide roughly uniform current density in the notch.

For the corrosion phase for the cracked ALT specimens, the specimens were left to corrode freely in seawater for 8 months, to allow the full effect of all time-dependent corrosion mechanisms in the fatigue cracks from a summer season. All specimens

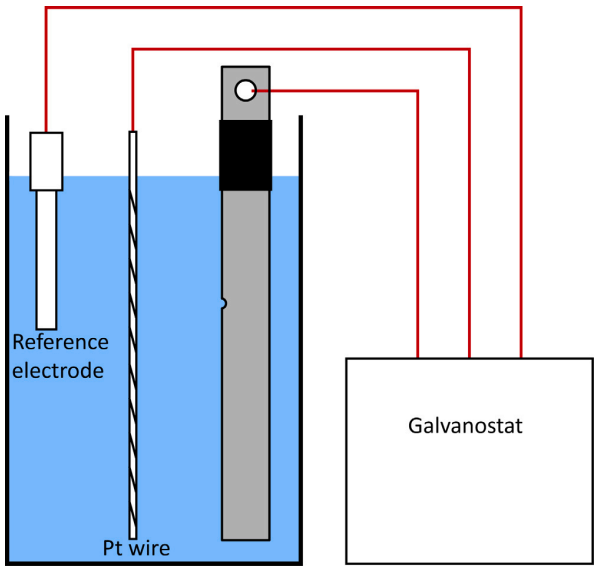

Fig. 8. Cell for precorrosion of a specimen in TP2. To accurately define the anode surface area on the specimen, the top of the specimen was sealed off with tape.

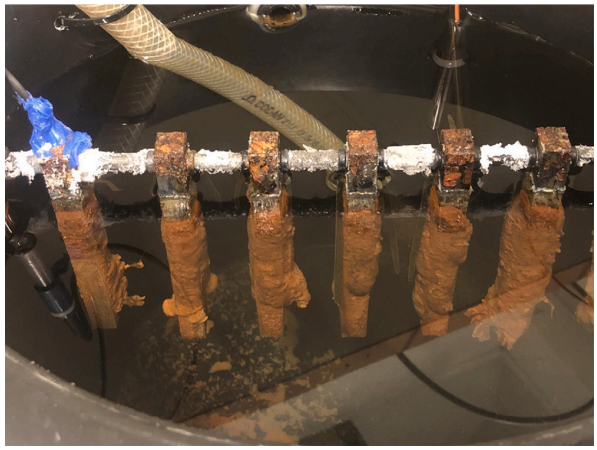

Fig. 9. Natural corrosion of the TP2 ALT specimens. Large amounts of oxide is visible.

were corroded together in a 15 l cell, shown in Fig. 9. Water was continuously pumped from 80 m depth in the Trondheim fjord (Trondheim, Norway) to an indoor laboratory. The flow rate through the corrosion cell was about 0.3 l/min. The water temperature varied between 10 and 16 °C. When the corrosion phase was finished, the specimens were cleaned with a plastic brush and dried.

2.2.3. *Fatigue setup*

The specimens were fatigued in three-point bending in an Amsler 100 HFP 5000 electromagnetic resonance fatigue tester at a load frequency of about 105 Hz. Fig. 10 shows a test specimen in the fatigue jig. Assuming that the degree of crack growth retardation from corrosion blunting might be sensitive to the load level, fatigue testing was done at two slightly different load levels, LL1 and LL2, as shown in Table 1. The loads were selected to give similar lifetimes as in TP1. Compared to in TP1, higher

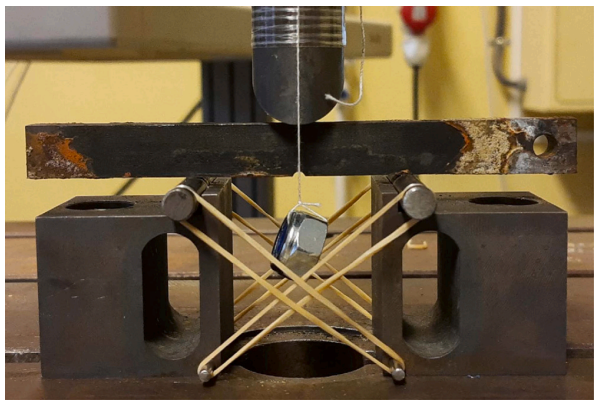

Fig. 10. TP2 three-point bending fatigue rig, with a distance between rollers of 56 mm. The nut and string are attached only for alignment purposes.

Table 1
Load level specifications. The longitudinal stress amplitude in the notch after precorrosion, calculated by FEA, is also stated.

Load level	Load amplitude/kN	Load ratio	Notch stress amplitude/MPa
LL1	3.30	0.3	397
LL2	3.47	0.3	418

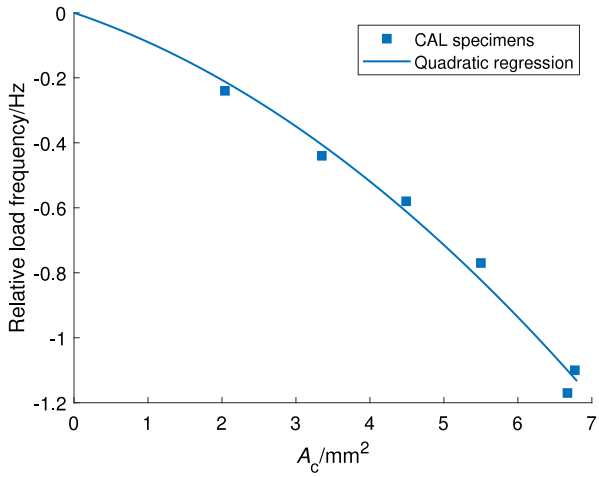

Fig. 11. Quadratic regression of relationship between total crack area and load frequency drop based on measurements on the CAL specimens.

surface stress amplitudes were needed. Reasons for this might be the less severe surface topographies on the specimens, due to a shorter precorrosion phase, or a steeper stress gradient due to the smaller notch and the applied bending load.

Before the CONT and ALT specimens were fatigued, a group of *calibration* (CAL) specimens were used to investigate the relationship between crack geometry and measured load frequency in the resonance fatigue tester. As a crack grows in a specimen, the bending stiffness of the specimen will be reduced. In a resonance fatigue tester, where the load frequency follows the natural frequency of the specimen and other vibrating components, this results in the load frequency dropping. In the current test program, the frequency drop was measured live and used to monitor crack growth. In order to translate the measured frequency drop into a useful crack geometry measurement, fatigue tests of six CAL specimens were stopped at different frequency drops of 0.2–1.2 Hz. The specimens were broken apart and the corresponding fatigue crack geometry was measured from the fracture surface. The 0.2 Hz value was chosen as the smallest frequency drop that could be detected over the noise of the load frequency signal. Such a detectable frequency drop indicated that a crack had initiated.

Fig. 11 shows the results of the calibration. A strong link between measured A_c, the total area of all cracks in a specimen, and frequency drops was registered. Quadratic regression resulted in a high coefficient of determination of $R^2 = 0.99$. Measured crack

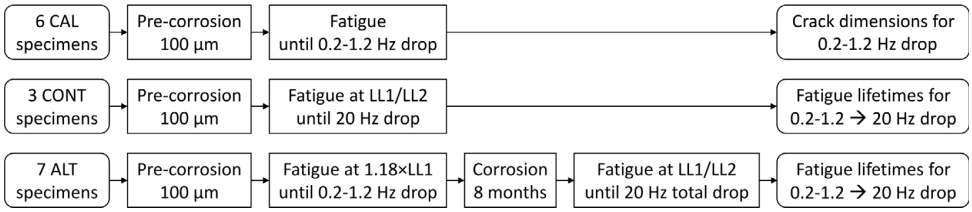

Fig. 12. Flowchart for TP2.

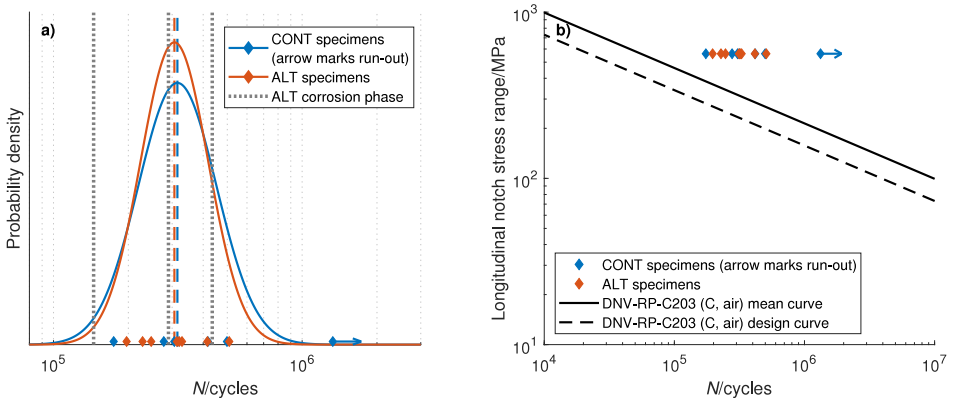

Fig. 13. (a) Probability density functions (solid lines) and mean $\log N$ (dashed lines) for both specimen groups. Diamond markers show observed lifetimes for individual specimens. (b) Comparison of the measured lifetimes with DNV-RP-C203 S–N mean and design (97.7% probability of survival) curves for detail category C in air.

depths showed a weaker correlation to the frequency drops than did the crack areas. Appendix C shows the fracture surfaces for the CAL specimens after they were broken off in liquid nitrogen. Details about crack geometries are provided in Appendix B.

From a theoretical point of view, it seems reasonable that a quadratic function would fit the data in Fig. 11 well. Derivations from the Euler–Lagrange equation for a freely vibrating, simply supported Euler–Bernoulli beam [30] with rectangular cross section yields a natural frequency, ω, that depends on the cross-section area to the power of 3/2 instead of 2, viz.

$$\omega \propto \sqrt{I} = \sqrt{\frac{wh^3}{12}} \propto A^{3/2}. \tag{1}$$

Here, I, w, h and A is the second moment of inertia, width, height and area of the beam cross section, respectively. However, this equation does not apply to notched and cracked specimens and does not include effects of vibrating parts of the fatigue tester.

After finishing the calibration, one CONT specimen was fatigued until failure at LL1, and two at LL2. The failure lifetime of a specimen was defined as the number of cycles for the load frequency to drop 20 Hz. This seemed to correspond to a crack covering nearly half of the original cross-section area of a specimen, see macrographs of the fracture surfaces in Appendix C. For the three specimens, the remaining lifetimes from measured frequency drops of 0.2–1.2 Hz until failure were noted and used as reference that the ALT specimens could be compared to.

Then, seven ALT specimens were fatigued until load frequency drops of 0.2–1.2 Hz. This was done at 18% higher load than LL1, to reduce the risk of any tests running out. The seven specimens were then corroded, before fatiguing was resumed and continued until the sum of frequency drops before and after corrosion was 20 Hz. Three specimens were fatigued at LL1, and four at LL2. The measured remaining lifetimes were compared to those of the CONT specimens at corresponding frequency drops and load levels. The flowchart for TP2 is shown in Fig. 12.

3. Results

3.1. TP1

Markers in Fig. 13a show the measured failure lifetimes, N, for all specimens. The results are also given in table form in Appendix B. Only one ALT specimen survived long enough to experience three corrosion phases (which are shown as gray, dotted lines every 145,000 cycles). Log-normal distributions have been fitted to both specimen groups by maximum likelihood

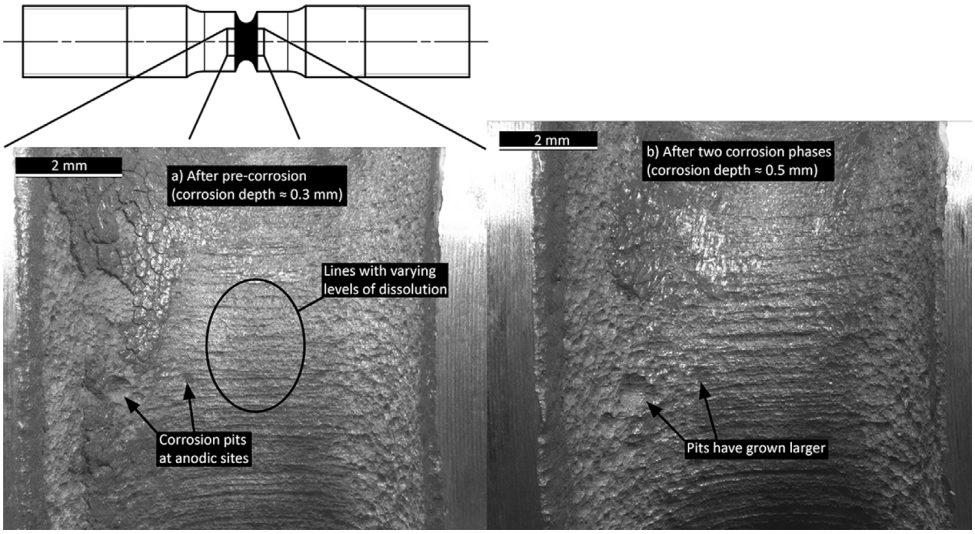

Fig. 14. Notch surface of an ALT specimen after a) precorrosion and b) two corrosion phases. Lines parallel to the rolling direction at the notch base likely results from microstructural features of former, elongated austenite grains.

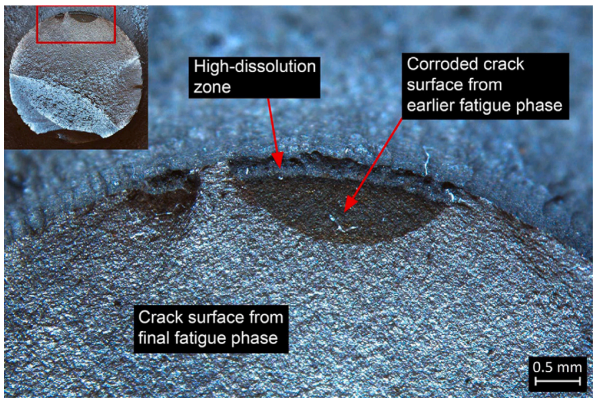

Fig. 15. Appearance of corroded cracks on the fracture surface of an ALT specimen after a corrosion phase and subsequent fatiguing.

regression [31]. Solid lines show the probability density functions (PDFs). For reference to offshore standards, the measured lifetimes have been plotted together with S–N curves from DNV-RP-C203 [32] in Fig. 13b.

The one CONT specimen that endured several times more load cycles than any other CONT specimens has been considered an outlier and disregarded during fitting of the PDF. Moreover, this specimen failed due to fatigue in threads, and the test is therefore marked as a run-out. During the test, the load frequency started dropping already at around 1.08×10^6 cycles, indicating a growing crack in the threads and, thus, possibly an altered stress distribution in the notch.

Even though the measured $\log N$ for the ALT specimens (mean = 5.49, standard deviation = 0.14) were on average slightly lower than for the continuous fatigue specimens (mean = 5.50, standard deviation = 0.16), an independent-samples t-test revealed that the difference was not significant, $t(12) = 0.15$, $p = 0.44$.

Fig. 14 shows macrographs of the notch surface of an ALT specimen after a) precorrosion and b) two corrosion phases. Since corrosion was accelerated by anodic polarization, one can imagine that shorter distances between protruding surface features and the cathode may have resulted in decreased electrolyte resistance and higher current densities at these, thus causing some degree of surface leveling. Nevertheless, the resulting surfaces in Fig. 14 are relatively rough, with obvious anodic and cathodic sites. By the end of the second corrosion phase, it is apparent that the surface has evolved into a slightly rougher one, and pits at persistent anodic sites have increased in size. The larger pits might have led to higher stresses at and near the surface, promoting earlier fatigue crack initiation than if the surface had remained in the precorroded state.

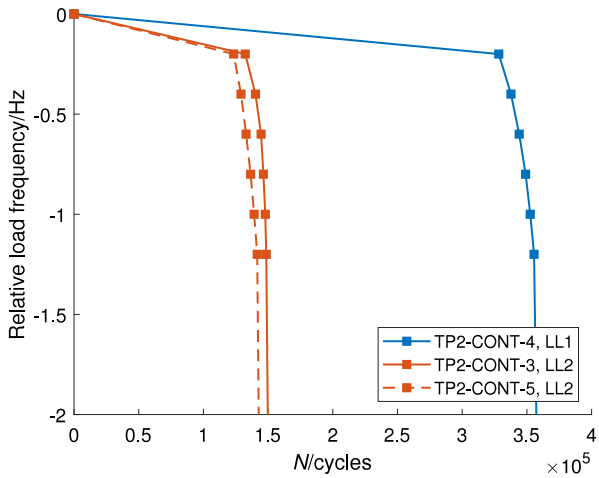

Fig. 16. Cycle count measurements at different load frequency drops for the CONT specimens. Each line represents one specimen, with IDs corresponding to the notation from Appendix B.

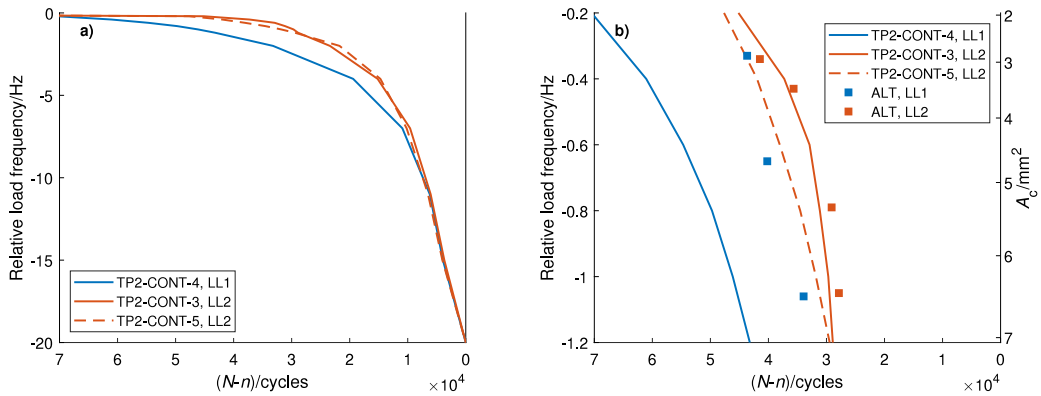

Fig. 17. (a) Remaining lifetime of the cracked CONT specimens at different load frequency drops. (b) Comparison with the cracked ALT specimens after eight months of corrosion and fatigue testing until failure.

From Fig. 15, which shows cracks in an ALT specimen after a corrosion phase, it can be seen that the dissolution rate has been high along the crack mouth down to a depth of about 0.2 mm during the anodic polarization. This indicates an anodic site for large cracks that is not at the crack tip, at which the dissolutive effect of corrosion might thus be limited.

From fractographs in Appendix C, it seems that all ALT specimens failed by fracture from cracks that had corroded in the previous corrosion phase. Of three specimens with corroded cracks that were shallow enough to be enclosed by the aforementioned zone of high dissolution, only one specimen experienced more than one corrosion phase. For the other two, it is thus clear that the extensive blunting of the crack tip did not retard crack growth sufficiently for the specimen to survive until the next corrosion phase. Four ALT specimens with larger corroded cracks showed even bands of high dissolution along the crack mouths, which indicated that the crack surfaces had been exposed only during the last corrosion phase.

3.2. TP2

Fig. 16 shows the load frequency drop measurements that were done on the CONT specimens at different cycle counts, n. In Fig. 17a, the curves from Fig. 16 have been translated horizontally so that the failure lifetimes (N) of the three specimens are aligned on the right vertical axis. By normalizing the curves by failure lifetime, the remaining lifetime, $N - n$, of a specimen at a

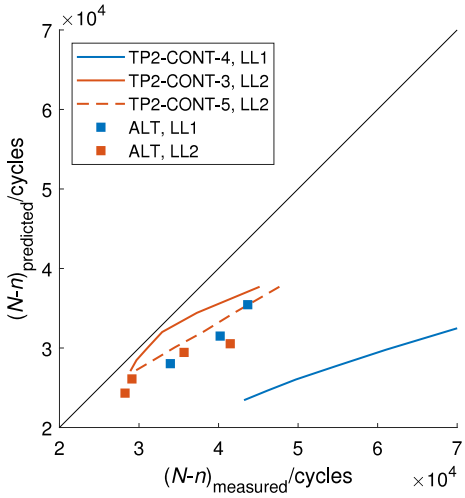

Fig. 18. Remaining lifetimes predicted according to BS 7910, compared to measured remaining lifetimes.

certain frequency drop can be read from the horizontal axis. In the current work, the remaining lifetime (consisting of crack growth) was adopted as measure for comparing lifetimes of the CONT and ALT specimens, to avoid the higher scatter often associated with crack initiation times.

In Fig. 17b, remaining lifetimes that were measured for the ALT specimens after the corrosion phase have been plotted by markers, for comparison with the CONT specimen curves. The right axis shows the crack areas that correspond to the load frequency drops on the left axis, as calculated from the quadratic-regression fit of Fig. 11. For LL2, there seem to be not much deviation between the CONT and the ALT specimens. For LL1, remaining lifetimes of the ALT specimens are slightly longer than for LL2, as expected. However, the remaining lifetime of the single CONT specimen is much longer than those of the corresponding ALT specimens.

To provide additional background for discussion, remaining lifetimes of the CONT and ALT specimens were predicted based on the crack growth rates of ferritic steel in air given in the BS 7910 standard [33]. The crack growth calculations were carried out by using a SIF solution for a single-edge-cracked bending specimen with rectangular cross section [34], while assuming an initial crack depth of $a = d + A_c/W$. Here, d and W is the notch depth and specimen width, respectively. While this approach might be crude, it allows for some degree of comparison between the CONT and ALT specimens. Fig. 18 shows the calculation results together with measured remaining lifetimes. It can be seen that, although the calculations slightly underestimate the measurements, the scatter is relatively low. The exception is the CONT specimen loaded at LL1, for which the measured remaining lifetimes are far higher than predicted. Reasons for this will be discussed later in the succeeding section.

4. Discussion

Contrary to what was expected, the corrosion phases did not have any significant effects on remaining fatigue lifetimes in air. Some likely explanations for this observation are given here, as well as what can be inferred from this finding regarding fatigue of mooring chains.

Firstly, the method for accelerating the corrosion phases in TP1 is reviewed. TP1 was designed to explore the effect of corrosion on fatigue surface damage. However, cracks initiated and developed too quickly to highlight this topic extensively. Thus, the relevant site for corrosion shifted to the crack tip, where the corrosion mechanisms are geometrically more restricted. Since the electrolyte resistance is inversely proportional to the area through which charge is being carried, the narrow opening of a fatigue crack results in a very high resistance, thus limiting the current. Therefore, after a fatigue crack had initiated in a specimen, the effect of accelerating corrosion with the current method was likely very limited at the crack tip.

Significant effects of the corrosion phases can thus only be expected for fatigue surface damage and for short cracks in the high-dissolution zone. By the looks from the notch surface outside a corroded crack in a dummy specimen in Fig. 19, it seems that the crack's width of around 0.2 mm in the high-dissolution zone is at least as extensive as could be expected from average corrosion rates in the North Sea. Yet, for the shallow, corroded cracks from TP1, it has been shown that corrosion did not seem to have a great lifetime-extending effect from crack tip blunting.

As no high-dissolution zone is visible on the corroded crack surfaces of TP2, the current way of accelerating corrosion exhibits dissolutive patterns in cracks that are clearly deviating from those in naturally corroding cracks. Thus, when studying corrosion effects on cracks, specimens should be subjected to natural corrosion to obtain the most accurate results.

For determining effects of corrosion phases on fatigue cracks in TP2, the remaining lifetimes of CONT and ALT specimens were compared. It was assumed that the crack growth is a relatively deterministic phenomenon, and that the crack growth rate depends

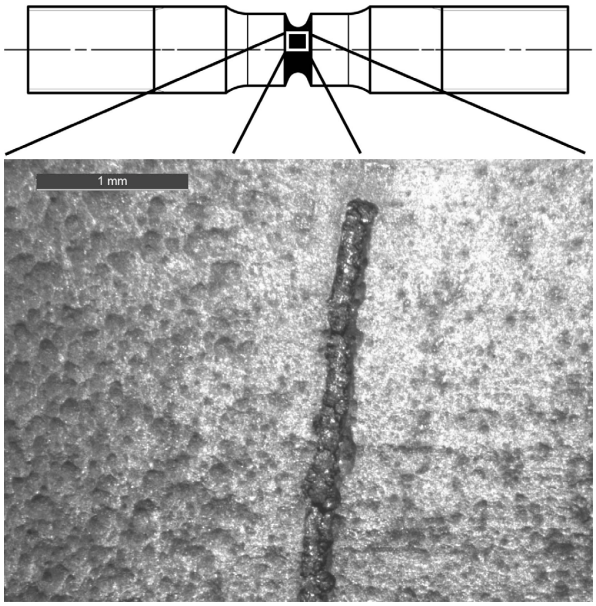

Fig. 19. Corroded crack in the notch of a dummy specimen in TP1.

closely on the crack driving force. Thus, two specimens with similar geometry and crack shape should have roughly the same remaining lifetime if loaded equally under the same conditions. However, even if two cracks yielded the same load frequency drop in fatigue tests, indicating similar crack areas, it does not mean that their shape is the same. Thus, the SIF ranges may differ between the cracks, and so will the crack growth rate. The CONT specimen that was subjected to LL1 is shown in Fig. 17 to have considerably longer remaining lifetime than the specimens subjected to LL2 have, at only 5% lower load. This seems peculiar and might have been a result of an atypical crack shape in the specimen and a less critical SIF range at the crack tip. Even though there was scatter in the rest of the TP2 results, it seemed to be low enough in the results from both CONT and ALT specimens to conclude that the eight-month corrosion phase at least did not have a large impact on the state of the cracks of the ALT specimens.

To explain this insensitivity to the corrosion phase, some discussion on the hypothesis that blunting of a crack by corrosion can retard crack growth is useful. As already mentioned, several authors have found that a corrosion pit has an equally severe SIF as a crack of the same depth [10,15,16]. It can be argued that a crack blunted by corrosion cannot have a geometry that is less stress-raising than a corrosion pit. Thus, it seems unlikely that blunting by corrosion would have a significantly retarding effect on crack growth. Any retarding effects that might be observed, are assumed to be results of other mechanisms. A mechanical explanation may be that even if a crack appears "blunted", the crack tip is not smooth. There may exist severe microscopic surface features that facilitates swift crack reinitiation. Even macroscopically, a blunted crack is still a very powerful local stress raiser, which too promotes crack reinitiation.

In the current test programs, the intensity and duration of the load in a fatigue phase might have deviated from what a mooring chain experiences during a winter storm. On small-scale fatigue tests of corroded surfaces of offshore mooring chains under high loads, fatigue initiation times have been demonstrated to be relatively short [35]. If, because of higher loads, initiation times in the current tests are shorter than for chains in service, then the potential for fatigue process retardation is reduced. Work is under way to quantify the magnitudes of the stresses in mooring chains in service, so that the relevance of the current tests can be evaluated.

Whereas mooring chains are subjected to stochastic loading and continuous corrosion, the test conditions in the current work were simplified by separating the corrosion and fatigue phases. In both phases, the simplification likely leads to reduced dissolution at the crack tip from corrosion compared to in-service conditions: In the summer season, static stresses from pretensioning and self-weight loads on an offshore mooring chain would increase crack opening and crack tip strains, promoting higher dissolution rates. In winter, the presence of seawater during load cycling would also lead to some additional dissolution. However, even though these effects would result in more pronounced crack tip blunting, the arguments about its effects on fatigue behavior still apply, and it is unlikely that blunting significantly retard further crack growth.

The absence of the corrosive environment during the fatigue phases is furthermore likely to push lifetime results in a non-conservative way compared to in-service conditions for mooring chains. Nevertheless, applying alternating corrosion and fatigue phases is seen as a practical way of investigating qualitative effects on crack development of the relevant seasonal extreme load variations during corrosion fatigue.

In order to stay within the load limitations of the fatigue rig used in TP1, specimen dimensions had to be kept relatively small. Consequently, as a result of reducing the specimen cross sections with each corrosion phase, the surface stresses in the notch grew.

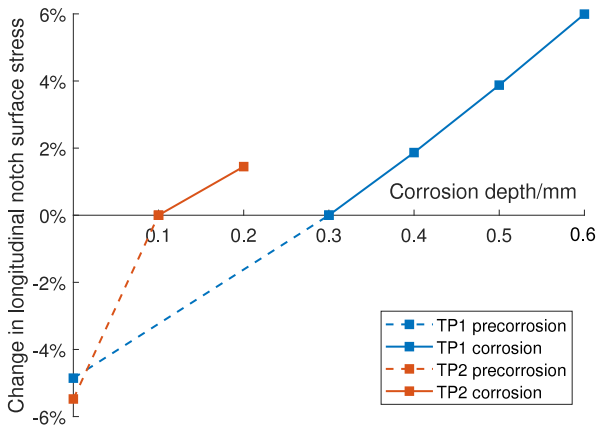

Fig. 20. Longitudinal notch surface stresses calculated by FEA after removal of material layers with uniform depths. The depths of the removal of material are corresponding to estimated removed material from corrosion phases. The stresses have been normalized w.r.t. the stresses after precorrosion.

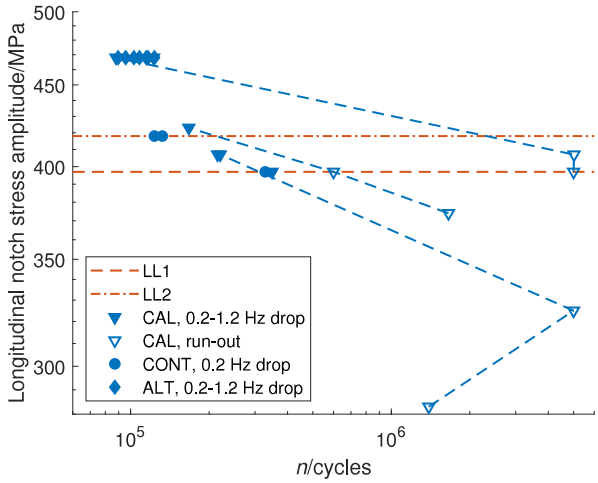

Fig. 21. Surface stress amplitude *S-N* plot of all specimens from the first fatigue phase of TP2. For the CONT specimens, the cycle count until 0.2 Hz load frequency drop is shown. Unfilled markers show run-outs, and dashed lines connect measurements that were made on the same specimen.

An increasing notch radius also meant that the stress-raising effect of the notch extended deeper into the material. These increased stresses, in addition to raised surface stresses from growing corrosion pits, promoted faster crack initiation. To yield conservative results, no adjustments were made to the load during the course of the testing. Thus, in order to limit the increase of stresses in the notch, corrosion phases had to happen relatively infrequently. Fig. 20 shows the nominal effect on the notch surface stresses from the corrosion phases, calculated by FEA, assuming uniform material removal rates. For the specimen that underwent three corrosion phases, a final change in stress of 6.0% was calculated. This might have had a substantial impact on the total fatigue lifetime.

For TP2, the effect was less pronounced, with notch stresses for the ALT specimens being only 1.4% higher after the corrosion phase, assuming that 0.1 mm of material was removed uniformly across the surface during this phase.

Because of the larger dimensions of mooring chains, the same material removal rates as used in these tests will, of course, have less effect on chain surface stresses than in the specimens.

To give the reader a sense of the stress levels used in TP2, measured cycle counts for the first fatigue phase of all TP2 specimens have been compiled in *S–N* format in Fig. 21. This means, for the CAL specimens, all cycles until they were cracked open in liquid

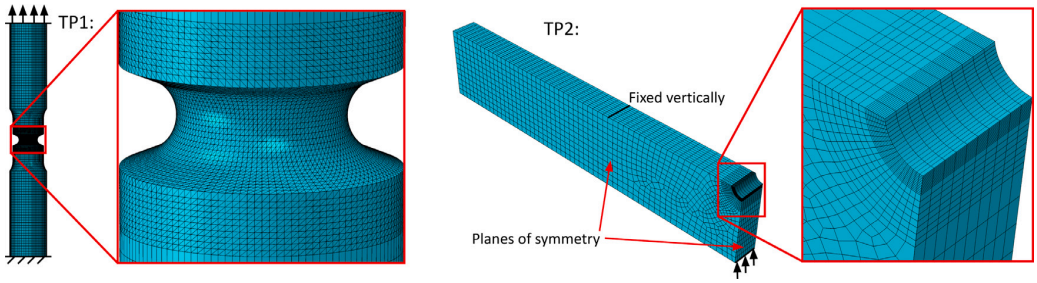

Fig. A.22. FEA models used in the current work.

Table B.2
TP1 specimen positions and measured lifetimes. Positions refer to Fig. 1.

Specimen ID	Link ID	Position on link	N/cycles	No. of corrosion phases (after precorrosion)
TP1-CONT-1-1	1	1	417,758	N/A
TP1-CONT-1-12	1	12	498,589	N/A
TP1-CONT-1-14	1	14	306,174	N/A
TP1-CONT-2-4	2	4	1,328,576[a]	N/A
TP1-CONT-2-6	2	6	316,096	N/A
TP1-CONT-2-8	2	8	174,610	N/A
TP1-CONT-2-14	2	14	277,691	N/A
TP1-ALT-1-5	1	5	509,112	3
TP1-ALT-1-6	1	6	313,607	2
TP1-ALT-1-9	1	9	196,800	1
TP1-ALT-1-10	1	10	320,370	2
TP1-ALT-1-15	1	15	247,110	1
TP1-ALT-2-5	2	5	415,814	2
TP1-ALT-2-12	2	12	228,170	1
TP1-ALT-2-15	2	15	328,721	2

[a]Run-out because of failure in the threads.

nitrogen. For the CONT specimens, the cycles until 0.2 Hz frequency drop are shown, and for the ALT specimens, the cycles endured at load 18% above LL1. Surface stress amplitudes have been calculated by FEA. The load levels in TP2 were chosen by means of gradually stepping up the load for a few run-out CAL specimens until load frequency drops could be observed. In the figure, results from the step-up of load have also been included. All markers connected by dashed lines represent the same specimen. From the large scatter at medium loads, it may seem that the final testing loads are just above the fatigue limit — or at least a lifetime regime governed by a gentler-slope S–N curve.

5. Conclusions

In the current study, two test programs of alternating corrosion and fatigue phases on R4-grade steel were conducted to replicate seasonal load variations on offshore mooring chains in service. One was on the effect of periodic phases of corrosion on fatigue lifetime of precorroded specimens. Here, corrosion was accelerated by anodic polarization. The other was on the effect of eight months of natural corrosion on the remaining lifetime of specimens with fatigue cracks.

For the specimens in the first test program, no significant difference in mean lifetime was registered compared to the reference group that was fatigued in air. Extensive blunting of shallow fatigue cracks in a few specimens did not seem to retard further crack growth to a large degree. However, in the majority of the specimens, cracks grew deep during fatigue phases, largely restricting any effect from accelerated corrosion processes at the crack tip during the following corrosion phase. Thus, accelerated corrosion is deemed unsuitable for studies of effects of natural corrosion on cracks. A weakness in the current test setup was that surface stresses were increased with each corrosion phase, promoting faster crack initiation in the specimens undergoing corrosion phases than in the reference group.

In the second test program, contrary to what was expected, no large extending effect on remaining lifetimes from crack tip blunting by natural corrosion was registered. However, the conclusion that a fatigue crack blunted by corrosion is as critical as a sharp one is supported by observations in the literature. This implies that any potentially retarding effects on crack growth likely result from other mechanisms.

Table B.3
TP2 specimen positions, load levels and measured crack sizes and lifetimes. Positions refer to Fig. 6.

Specimen ID	Position on link	Load level	A_c/mm^2	Depth of deepest crack/mm	Frequency drop before corrosion/Hz	N/cycles	$(N-n)$/cycles
TP2-CAL-6	6	1.18 × LL1	6.77	1.1	−1.1	122,515	N/A
TP2-CAL-8	8	1.07 × LL1[a]	3.35	1.19	−0.44	167,147	N/A
TP2-CAL-11	11	1.03 × LL1	5.5	1.58	−0.77	215,515	N/A
TP2-CAL-12	12	1.18 × LL1[a]	2.04	0.71	−0.24	87,903	N/A
TP2-CAL-15	15	1.03 × LL1[a]	6.67	1.47	−1.17	220,686	N/A
TP2-CAL-16	16	LL1	4.49	1.34	−0.58	348,815	N/A
TP2-CONT-3	3	LL2	N/A	N/A	−20	175,598	N/A
TP2-CONT-4	4	LL1	N/A	N/A	−20	396,688	N/A
TP2-CONT-5	5	LL2	N/A	N/A	−20	168,905	N/A
TP2-ALT-1	1	LL2	N/A	N/A	−0.34	95,700	41,470
TP2-ALT-2	2	LL2	N/A	N/A	−0.43	89,503	35,664
TP2-ALT-7	7	LL2	N/A	N/A	−0.79	114,790	29,110
TP2-ALT-9	9	LL2	N/A	N/A	−1.05	108,092	28,243
TP2-ALT-10	10	LL1	N/A	N/A	−1.06	116,604	33,940
TP2-ALT-13	13	LL1	N/A	N/A	−0.33	102,938	43,670
TP2-ALT-14	14	LL1	N/A	N/A	−0.65	123,372	40,203

[a]Last applied load level. Specimens also sustained significant numbers of cycles at lower load levels. See Fig. 21 for details.

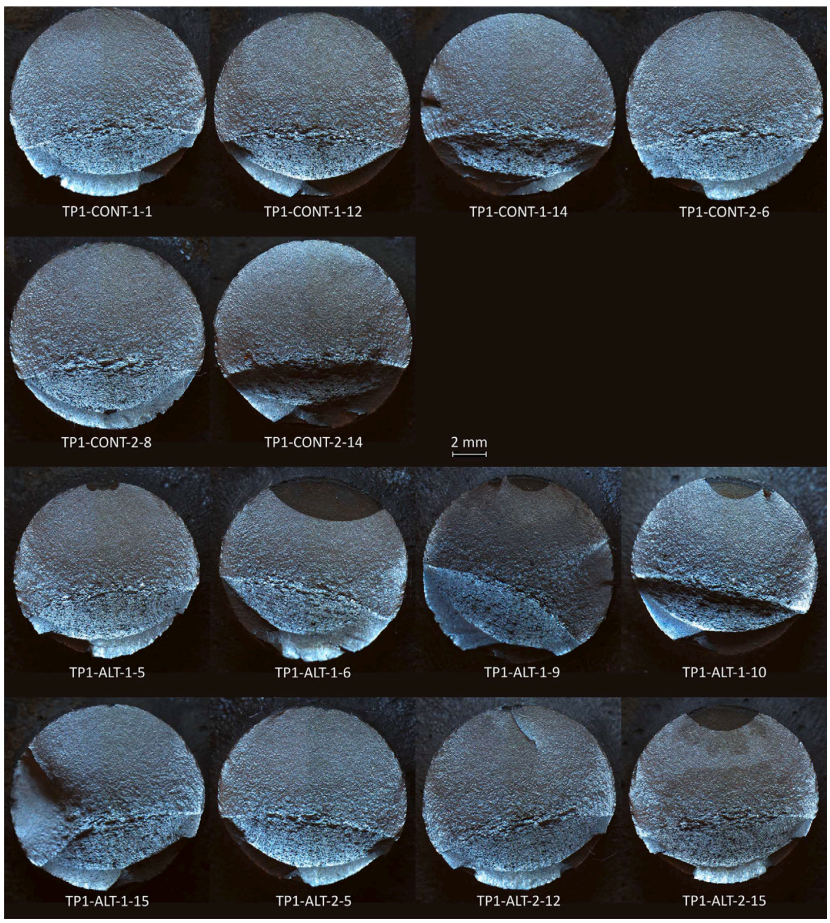

Fig. C.23. Macrographs of fracture surfaces of specimens from TP1. Codes on the figure refer to the specimen IDs stated in Table B.2.

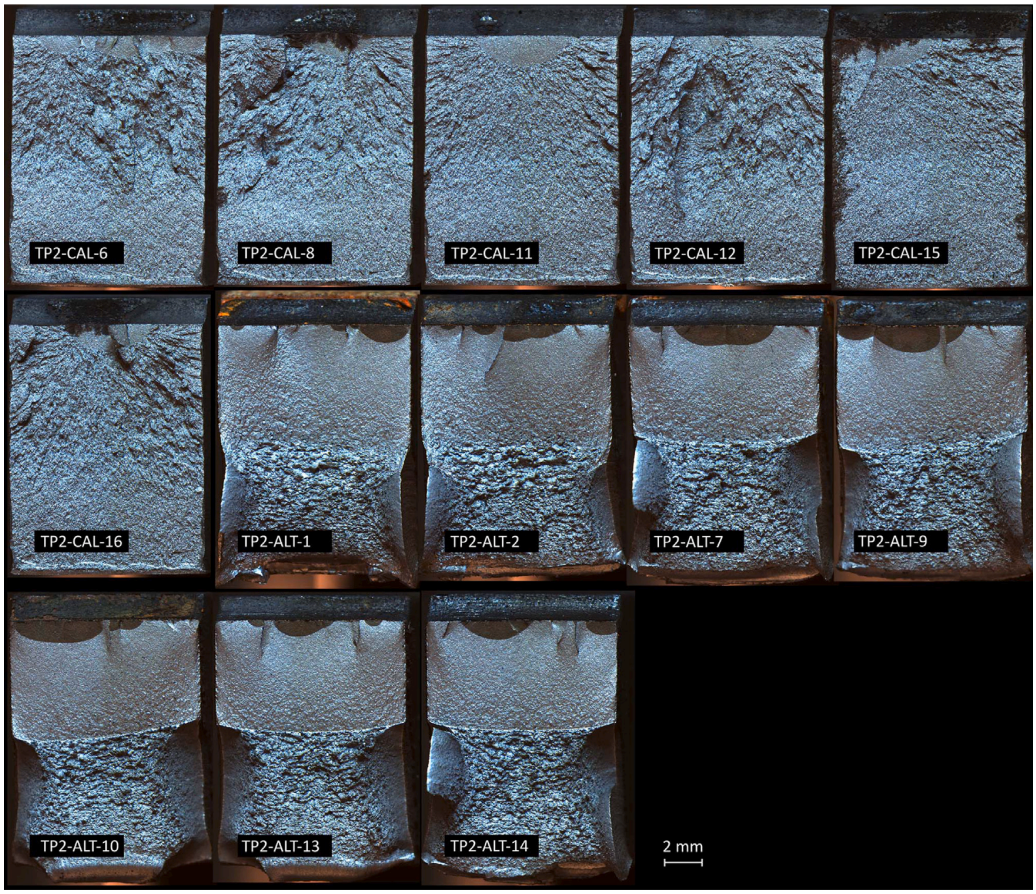

Fig. C.24. Macrographs of fracture surfaces of specimens from TP1. Codes on the figure refer to the specimen IDs stated in Table B.3. The CAL specimens were submerged in liquid nitrogen and cracked open after fatiguing to different crack depths. The ALT specimens were cracked open in ambient temperature after fatiguing until 20 Hz load frequency drop. Fracture surfaces of some CAL specimens were damaged by corrosion in air during storage. Specimens TP2-ALT-1 and TP2-ALT-2 were fatigued until unstable fracture at load frequency drops between 20 and 25 Hz, instead of terminating the fatiguing at 20 Hz drop. However, the cycle count at 20 Hz drop was used for lifetime evaluations.

Declaration of competing interest

The authors declare that they have no known competing financial interests or personal relationships that could have appeared to influence the work reported in this paper.

Acknowledgments

The authors would like to thank O. Ø. Knudsen, A. Erbe, T. A. Kristensen, A. Hellesvik, M. Aursand, C. Torres and other researchers and staff at SINTEF and NTNU for helpful discussions on the experimental setup and results processing. This work was supported through the project KPN LifeMoor by the Research Council of Norway (RCN contract no.: 280705).

Appendix A. FEA methodology

All FEAs in the current work was performed using the Abaqus 2017 software and 3D solid models. Material properties for R4-grade steel was implemented in the form of a monotonic material model from [36].

The meshed FEA models are shown in Fig. A.22. For TP1, the whole specimen was modeled. As boundary condition, one end surface of the specimen was fixed. The axial load was applied on the other end surface, while forcing this surface to remain plane. Quadratic-order tetrahedron elements (C3D10) was used in and around the notch. The element length was 0.39 mm in the tangential direction of the notch. Thus, each element covered a 7° sector of the notch profile. The total element count in the model was 332,730.

In TP2, the two planes of symmetry were utilized to model only one quarter of a specimen. In the location of the support rollers (see Fig. 10), vertical translations were fixed. The load was applied along a non-deformable line at the center of the specimen, representing the load punch. Linear-order hexahedron elements (C3D8) were used in the model. The element length in tangential direction of the notch was 0.11 mm, covering 4° of the notch profile. The total element count was 12,090.

For calculating stresses after corrosion phases, specimen dimensions were changed accordingly, and the models were remeshed.

Appendix B. Specimen details and lifetimes

See Tables B.2 and B.3.

Appendix C. Macrographs of fracture surfaces

See Figs. C.23 and C.24.

References

[1] Fernández J, Storesund W, Navas J. Fatigue performance of grade R4 and R5 mooring chains in seawater. In: Proceedings of the ASME 2014 33rd International Conference on Ocean, Offshore and Arctic Engineering. ASME; 2014, http://dx.doi.org/10.1115/OMAE2014-23491.

[2] Lone EN, Sauder T, Larsen K, Leira BJ. Probabilistic fatigue model for design and life extension of mooring chains, including mean load and corrosion effects. Ocean Eng 2022;245:110396. http://dx.doi.org/10.1016/j.oceaneng.2021.110396.

[3] Bauer E. Interannual changes of the ocean wave variability in the North Atlantic and in the North Sea. Clim Res 2001;18(1–2):63–9. http://dx.doi.org/10.3354/cr018063.

[4] Gabrielsen Ø, Liengen T, Molid S. Microbiologically influenced corrosion on seabed chain in the North Sea. In: Proceedings of the ASME 2018 37th International Conference on Ocean, Offshore and Arctic Engineering, Vol. 3. ASME; 2018, http://dx.doi.org/10.1115/OMAE2018-77460.

[5] Ma K, Gabrielsen Ø, Li Z, Baker D, Yao A, Vargas P, et al. Fatigue tests on corroded mooring chains retrieved from various fields in offshore West Africa and the North Sea. In: Proceedings of the ASME 2019 38th International Conference on Ocean, Offshore and Arctic Engineering, Vol. 3. ASME; 2019, http://dx.doi.org/10.1115/OMAE2019-95618.

[6] Schijve J. Fatigue of Structures and Materials. 2nd ed.. Springer Netherlands; 2009, http://dx.doi.org/10.1007/978-1-4020-6808-9.

[7] Gangloff RP. Corrosion fatigue crack propagation in metals. In: 1st International Conference on Environment Induced Cracking of Metals. NASA; 1990, URL https://ntrs.nasa.gov/citations/19900015089.

[8] Shipilov SA. Mechanisms for corrosion fatigue crack propagation. Fatigue Fract Eng Mater Struct 2002;25(3):243–59. http://dx.doi.org/10.1046/j.1460-2695.2002.00447.x.

[9] Suresh S, Ritchie R. Near-threshold fatigue crack propagation: A perspective on the role of crack closure. Tech. rep, Lawrence Berkeley National Laboratory; 1983, LBL-16263 URL https://escholarship.org/uc/item/8mr83283.

[10] Komai K, Minoshima K, Kinoshita S, Kim G. Corrosion fatigue crack initiation of high-tensile-strength steels in synthetic seawater. JSME Int J Ser 1, Solid Mech Strength Mater 1988;31(3):606–12. http://dx.doi.org/10.1299/jsmea1988.31.3_606.

[11] Austen I. Quantitative assessment of corrosion fatigue crack growth under variable amplitude loading. Tech. rep, London, UK: British Steel Corporation; 1988.

[12] Radon JC, Branco CM, Culver LE. Crack blunting and arrest in corrosion fatigue of mild steel. Int J Fract 1976;12(3):467–9. http://dx.doi.org/10.1007/BF00032842.

[13] Menan F, Henaff G. Influence of frequency and exposure to a saline solution on the corrosion fatigue crack growth behavior of the aluminum alloy 2024. Int J Fatigue 2009;31(11):1684–95. http://dx.doi.org/10.1016/j.ijfatigue.2009.02.033, Fatigue Damage of Structural Materials VII.

[14] Yamamoto N, Sugimoto T, Ishibashi K. Fatigue strength assessment of a structure considering corrosion wastage and corrosion fatigue. In: Proceedings of the ASME 2018 37th International Conference on Ocean, Offshore and Arctic Engineering, Vol. 3. ASME; 2018, http://dx.doi.org/10.1115/OMAE2018-78188.

[15] Kondo Y. Prediction of fatigue crack initiation life based on pit growth. Corrosion 1989;45(1):7–11. http://dx.doi.org/10.5006/1.3577891.

[16] Ishihara S, Saka S, Nan Z, Goshima T, Sunada S. Prediction of corrosion fatigue lives of aluminium alloy on the basis of corrosion pit growth law. Fatigue Fract Eng Mater Struct 2006;29(6):472–80. http://dx.doi.org/10.1111/j.1460-2695.2006.01018.x.

[17] Montgomery EL, Calle LM, Curran JC, Kolody MR. Timescale correlation between marine atmospheric exposure and accelerated corrosion testing – part 2. In: Corrosion 2012. NACE; 2012, NACE-2012-1730 URL https://onepetro.org/NACECORR/proceedings/CORR12/All-CORR12/NACE-2012-1730/120250.

[18] Baldwin K, Smith C. Accelerated corrosion tests for aerospace materials: Current limitations and future trend. Aircr Eng Aerosp Technol 1999;71(3):239–44. http://dx.doi.org/10.1108/00022669910270718.

[19] Du M, Chiang F, Kagwade S, Clayton C. Damage of Al 2024 alloy due to sequential exposure to fatigue, corrosion and fatigue. Int J Fatigue 1998;20(10):743–8. http://dx.doi.org/10.1016/S0142-1123(98)00043-7.

[20] Dong Z, Rong C. An investigation of alternate behavior of corrosion and fatigue of LY12CZ aluminum alloy. In: Proceedings of the 9th international conference on aluminium alloys. Institute of Materials Engineering Australasia Ltd; 2004, URL http://www.icaa-conference.net/ICAA9/data/papers/GP%2020.pdf.

[21] Nakano Y, Sandor B. Fatigue behavior of copper with intermediate surface layer removal. J Test Eval 1974;2:16–22. http://dx.doi.org/10.1520/JTE10067J.

[22] Zarandi EP, Skallerud BH. Experimental and numerical study of mooring chain residual stresses and implications for fatigue life. Int J Fatigue 2020;135:105530. http://dx.doi.org/10.1016/j.ijfatigue.2020.105530.

[23] Martinez Perez I, Constantinescu A, Bastid P, Zhang Y-H, Venugopal V. Computational fatigue assessment of mooring chains under tension loading. Eng Fail Anal 2019;106:104043. http://dx.doi.org/10.1016/j.engfailanal.2019.06.073.

[24] Faraday M. VI. Experimental researches in electricity. - Seventh series. Philos Trans R Soc 1834;124:77–122. http://dx.doi.org/10.1098/rstl.1834.0008.

[25] Zhang X, Noel N, Ferrari G, Hoogland M. Corrosion behaviour of mooring chain steel in seawater. In: The 67th annual meeting of the international society of electrochemistry. 2016, URL http://resolver.tudelft.nl/uuid:7eb6d065-cb82-4fbd-955c-822821337c21.

[26] Nevshupa R, Martinez I, Ramos S, Arredondo A. The effect of environmental variables on early corrosion of high–strength low–alloy mooring steel immersed in seawater. Mar Struct 2018;60:226–40. http://dx.doi.org/10.1016/j.marstruc.2018.04.003.

[27] Refait P, Grolleau A-M, Jeannin M, François E, Sabot R. Localized corrosion of carbon steel in marine media: Galvanic coupling and heterogeneity of the corrosion product layer. Corros Sci 2016;111:583–95. http://dx.doi.org/10.1016/j.corsci.2016.05.043.

[28] Fredheim S, Reinholdtsen S-A, Håskoll L, Lie HB. Corrosion fatigue testing of used, studless, offshore mooring chain. In: Proceedings of the ASME 2013 32nd international conference on ocean, offshore and arctic engineering. ASME; 2013, OMAE2013-10609.

[29] Gabrielsen Ø, Larsen K, Reinholdtsen S-A. Fatigue testing of used mooring chain. In: Proceedings of the ASME 2017 36th international conference on ocean, offshore and arctic engineering. ASME; 2017, http://dx.doi.org/10.1115/OMAE2017-61382.
[30] Han SM, Benaroya H, Wei T. Dynamics of transversely vibrating beams using four engineering theories. J Sound Vib 1999;225(5):935–88. http://dx.doi.org/10.1006/jsvi.1999.2257.
[31] Pollak RD, Palazotto AN. A comparison of maximum likelihood models for fatigue strength characterization in materials exhibiting a fatigue limit. Probab Eng Mech 2009;24(2):236–41. http://dx.doi.org/10.1016/j.probengmech.2008.06.006.
[32] Recommended practice DNV-RP-C203: Fatigue design of offshore steel structures. Standard, DNV; 2010.
[33] BS 7910:2019, Guide to methods for assessing the acceptability of flaws in metallic structures. Standard, BSI; 2019.
[34] Tada H, Paris PC, Irwin GR. the Stress Analysis of Cracks Handbook. Third Ed.. ASME Press; 2000, http://dx.doi.org/10.1115/1.801535.
[35] Qvale P, Zarandi EP, Ås SK, Skallerud BH. Digital image correlation for continuous mapping of fatigue crack initiation sites on corroded surface from offshore mooring chain. Int J Fatigue 2021;151:106350. http://dx.doi.org/10.1016/j.ijfatigue.2021.106350.
[36] Zarandi EP, Skallerud BH. Cyclic behavior and strain energy-based fatigue damage analysis of mooring chains high strength steel. Mar Struct 2020;70:102703. http://dx.doi.org/10.1016/j.marstruc.2019.102703.